

HADRONIC ENERGY FLOW
AND INCLUSIVE CHARGED
PARTICLE PRODUCTION
AT HERA

Stuart Mark Robertson

*Thesis submitted for the degree of
Doctor of Philosophy*

School of Physics and Space Research
Faculty of Science
University of Birmingham

September 1995

Synopsis

The energy flow in hard photoproduction interactions has been studied using data collected by the H1 detector at HERA during the 1993 data taking period. The production of jets and the energy flow about the resulting jet axis have been studied using a cone jet algorithm. The increased energy flow about the jet axis for jets reconstructed in the proton direction, compared with predictions of Monte Carlo event generators incorporating leading order pQCD calculations together with initial and final state radiation, is illustrated. The description of the energy flow has been found to be improved when multiple interactions models have been included.

The presence of multiple interactions has been further explored by studying charged particle production in the region $2.0 < \eta < 2.5$. To facilitate this the performance of the H1 Forward Tracker has been studied in detail, and the corrected track multiplicity measured in this region. This has further illustrated the inadequate description of photoproduction provided by leading order Monte Carlo generators and the improved description provided by the inclusion of multiple interaction models.

Cross sections are presented for the inclusive photoproduction of charged particles in the kinematical region $2.0 < \eta < 2.5$ and $p_T > 1.5\text{GeV}/c$. The transverse momentum distribution is found to be well described by a QCD inspired power law fit, and is found to be harder than observed in $p\bar{p}$ interactions at comparable centre of mass energies, $\sqrt{s_{\gamma p}} \approx \sqrt{s_{p\bar{p}}} \approx 200\text{ GeV}$.

This work was supported financially by the Particle Physics and Astronomy Research Council

Acknowledgements

I would like to thank Professor John Dowell for giving me the opportunity to work for the High Energy Physics Department, and for his help and guidance as my supervisor.

I am also grateful to the members of the H1 photoproduction working group for providing an interesting and relaxed environment for analysis during my stay at DESY. In particular, I am indebted to Gerhard Knies for his guidance and enthusiasm, and Mark Burton for his help with the Forward Tracker (good luck with the writing up).

I would also like to thank all the members of staff at Birmingham. In particular, I would like to thank Ian Kenyon and John Garvey for their help with getting to grips with HERA physics and H1. I would also like to thank Laurie Lowe for answering all my computer questions.

During my studentship, I have been fortunate to meet many interesting and lively people, who have made my time at Birmingham and DESY very enjoyable. I am grateful to Lee West, Paul Newman, Paul Sutton, Tim Nicholls, Kirstee Hewitt, Vicky Hudgson, Tanwir Ahmed and Hywel Phillips for their help as fellow H1'ers. Thanks Lee and Rachel for your culinary experiments which have prevented me from fading away during the dark days of writing up. I hope you both have an excellent time out at Hamburg. I am also grateful to you all for the many late night beer sessions in Hamburg.

I would also like to thank all the OPAL and OMEGA students at Birmingham. In particular I would like to thank Andy, Jim and Steve for their help as fellow newbies all those years ago, and for providing me with countless opportunities to

test my liver. Thanks also to Chris and Rich, I look forward to joining you and Jim down in Harrow to ruin the reputation of particle physics in the real world forever. I must also mention Paul Davies, Keith Norman, Dave Rigby, Mark Venables, Dave Rees, Dave Evans, James Bloomer and Andy Bell for providing such an entertaining working environment.

Thanks also to everyone I met in Hamburg, in particular Dave Kant, John Lomas, Pete Bispham, Mark Burton, Paul Sutton and Dave Milstead. I must also mention Rob Akers, for forcing me to get drunk even when I didn't want to.

Finally I would like to thank my parents and family for their support (not least of all financially!) during my studies.

Contents

1	Introduction	1
1.1	The Standard Model	1
1.1.1	Quantum Electrodynamics	3
1.1.2	The Electro-Weak Interaction	4
1.1.3	Quantum Chromo-Dynamics (QCD)	5
2	Physics at HERA	7
2.1	Introduction	7
2.2	Electron-Proton Scattering at HERA	7
2.3	Deep-Inelastic Scattering	8
2.3.1	The NC Deep Inelastic Cross Section	10
2.3.2	The Quark-Parton Model	10
2.3.3	Scaling Violations	11
2.4	Photoproduction	12
2.4.1	The Photon Structure Function	15
2.4.2	The Total Photoproduction Cross Section	18
2.4.3	Jet Production	23
3	The H1 Detector	27
3.1	The HERA accelerator	27
3.2	The H1 Detector	28
3.3	The H1 Tracking Detectors	31
3.3.1	The Central Tracking Detectors	33

3.3.2	The Forward Tracking Detectors	34
3.3.3	The Backward MWPC	36
3.4	The H1 Calorimeters	37
3.5	Muon Detection	40
3.6	Luminosity Monitoring	40
3.7	Scintillation Counters	42
3.8	Triggering and Off-line Analysis	42
4	Event Selection	45
4.1	Introduction	45
4.2	The Tagged Event Selection	45
4.3	Good Track Selection	52
4.4	MC Samples	53
4.4.1	PYTHIA	53
4.4.2	HERWIG	54
4.4.3	PHOJET	54
5	The Performance of the H1 Forward Tracker	55
5.1	Introduction	55
5.2	Track Reconstruction in the Forward Tracker	55
5.2.1	Planar Segment Pattern Recognition	56
5.2.2	Radial Segment Pattern Recognition	57
5.2.3	Line Segment Linking and Track Fitting	58
5.3	Determination of the Track Reconstruction Efficiency	59
5.4	Comparison of the Track Reconstruction Efficiency between Data and MC	67
5.5	Track Selection	69
5.6	Summary	80
6	The Photoproduction of Jets at HERA	82
6.1	Introduction	82

6.2	Jet Reconstruction	83
6.2.1	The QJCALO algorithm	83
6.3	Jet Pedestals	87
6.4	Summary and Conclusions	93
7	The Track Multiplicity in the Forward Region	95
7.1	Introduction	95
7.2	Event Sample	96
7.3	Determination of the Corrected Track Multiplicity	96
7.4	Results	99
7.5	Summary and Conclusions	102
8	The Inclusive Charged Particle Cross-section	103
8.1	Introduction	103
8.2	Cross Section Determination and Results	103
8.3	Summary	111
9	Summary	115

List of Figures

2.1	A schematic representation of deep inelastic scattering in lowest order QCD and QED.	9
2.2	A schematic representation of the typical contributions to the hard non-diffractive photoproduction cross section.	16
2.3	An example of multiple parton scattering in γp interactions.	22
2.4	The kinematics of a typical LO resolved photoproduction event.	24
2.5	The gluon density of the photon divided by the fine structure constant $\alpha=1/137$ at the scale $\langle p_T \rangle^2 = 75 \text{ GeV}^2$	25
3.1	The layout of the HERA accelerator and pre-accelerators.	28
3.2	The H1 detector (3D view).	30
3.3	Side view of the H1 tracking detectors.	32
3.4	Cell structure of the Central Jet Chamber	34
3.5	Side view of the H1 Forward Tracker.	35
3.6	The Planar Drift Chambers.	36
3.7	The Radial Drift Chambers.	37
3.8	Containment of the LAr stacks: iso- λ and iso- X_0 lines	39
3.9	The Backward Electromagnetic Calorimeter (BEMC): x, y view.	40
3.10	The H1 Luminosity System.	41
4.1	The y_{TAG} distribution for (a) sample I, (b) the background sample and (c) sample I compared with the background sample normalised to the number of events with $y_{TAG} < 0.2$	48

4.2	The measured ZVTX distribution for a sample of 897 proton pilot bunch events.	49
4.3	The measured ZVTX distribution for data and Monte Carlo respectively.	50
4.4	The measured y_{TAG} spectrum for data and Monte Carlo respectively.	51
5.1	The average track reconstruction efficiency as a function of (a) pseudorapidity, η , and (b) transverse momentum, p_T	61
5.2	The average track reconstruction efficiency as a function of the total number of reconstructed tracks in the forward tracker.	62
5.3	The average planar segment reconstruction efficiency as a function of the total number of reconstructed tracks in the forward tracker for each respective supermodule.	63
5.4	The planar segment linking efficiency as a function of the total number of reconstructed tracks in the forward tracker.	64
5.5	The distributions of the ratio R1 and the distance ΔR for (a),(b) particles matched to three successfully linked planar segments, and (c),(d) particles in which the matched planar segment in the first supermodule has failed to be linked to the remainder of the track in the second and third supermodules.	65
5.6	A comparison of the ‘missing segment efficiency’ between data and MC for each supermodule.	68
5.7	The percentage of (a) primary reconstructed tracks accepted and (b) secondary reconstructed tracks rejected as a function of the cut applied to the χ^2 of the vertex fit.	71
5.8	The reconstructed track resolution in $1/p$ before and after the vertex constraint.	73
5.9	The distributions of (a) $ DCA $ and (b) $ Z_0 - Z_{vtx} $ before and after the vertex constraint.	74
5.10	The distributions of the track parameters a) $ DCA $, b) $ Z_0 - Z_{VTX} $ for primary reconstructed tracks and secondary reconstructed tracks.	75

5.11	The percentage of primary tracks accepted, (a),(c), and the percentage of secondary tracks rejected, (b),(d), as a function of the track parameters $ DCA $, $ Z_0-Z_{vtx} $	76
5.12	A comparison of the of the track parameters (a) DCA, and (b) Z_0 -ZVTX between data and Monte Carlo.	77
5.13	The reconstructed track resolution in (a) $1/p$ and (b) pseudorapidity, η , after the full track selection.	78
5.14	The average track selection efficiency as a function of (a) the number of reconstructed tracks in the forward tracker and (b) the transverse momentum of the track.	79
5.15	The track purity as a function of the transverse momentum of the track.	80
6.1	The distance Δr in the η/ϕ plane between the reconstructed jet axis and the nearest outgoing parton.	85
6.2	The correlation of the pseudorapidity, η , and azimuthal angle, ϕ , between the reconstructed jet axis and the nearest outgoing parton from the hard scattering.	86
6.3	The correlation between the transverse energy, E_T^{jet} , of the reconstructed jet axis and the transverse momentum, p_T , of the nearest outgoing parton from the hard subprocess.	87
6.4	The observed transverse energy flow about the jet axis versus the pseudorapidity distance from the jet direction and the azimuthal angle with respect to the jet direction. Full circles are H1 data. The curves refer to the predictions from the PYTHIA event generator with (full) and without (dashed) the inclusion of multiple interactions. . .	89

6.5	The observed transverse energy flow about the jet axis versus the pseudorapidity distance from the jet direction and the azimuthal angle with respect to the jet direction. Full circles are H1 data. The curves refer to the predictions from the HERWIG generator including the soft underlying event option for 35% of events (full) and the PHOJET generator (dashed) respectively.	91
6.6	The distribution of the transverse energy measured outside the jets in the slice $ \eta^{cell} - \eta^{jet} \leq 1.0$, $E_T^{Pederal}$, normalised to the area of the jet cone. Full circles are H1 data. The curves refer to the predictions from the PYTHIA event generator with (full) and without (dashed) the inclusion of multiple interactions.	92
6.7	The distribution of the transverse energy measured outside the jets in the slice $ \eta^{cell} - \eta^{jet} \leq 1.0$, $E_T^{Pederal}$, normalised to the area of the jet cone. Full circles are H1 data. The curves refer to the predictions from the HERWIG event generator with the soft underlying event option for 35% of events (full) and the PHOJET generator (dashed) respectively.	93
7.1	The corrected distribution $1/N dN_{trk}/dp_T$ for events with $p_T^{max'} > 1.5$ GeV compared with predictions from the PYTHIA generator both with (solid histogram) and without (dashed histogram) the inclusion of multiple interactions.	100
7.2	The corrected distribution $1/N dN_{trk}/dp_T$ for events with $p_T^{max'} > 1.5$ GeV compared with predictions from the PHOJET generator (solid histogram) and the HERWIG generator (dashed - without soft underlying event / dash dotted - 35% events including soft underlying event).	101
8.1	The measured inclusive charged particle cross-section $\frac{d^2\sigma^e p}{dp_T^2 d\eta}$ in photoproduction (full circles) in the kinematical region $2.0 < \eta < 2.5$, $Q^2 < 10^{-2} \text{GeV}^2$ and $0.3 < y < 0.7$ at an average $E_{CMS}(\gamma p) \approx 200$ GeV.	106

8.2	The measured inclusive charged particle cross-section as depicted in figure 8.3 (full circles) compared with the previously measured cross section for the rapidity range $ \eta < 1.5$ (open circles).	108
8.3	The measured inclusive charged particle cross-section $\frac{d^2\sigma^{ep}}{dp_T^2 d\eta}$ in photoproduction (full circles) compared with the predictions from a LO QCD calculation using the PYTHIA generator.	110
8.4	The measured inclusive charged particle cross-section $d\sigma/d\eta$ in photoproduction in the kinematical region $p_T > 1.5$ GeV/c and $2.0 < \eta < 2.5$ (open circles) compared with the previously measured cross-sections in the η region $ \eta < 1.5$ and predictions from a LO QCD calculation using the PYTHIA generator.	112
8.5	The measured inclusive charged particle cross-section $d\sigma/d\eta$ in photoproduction in the kinematical region $p_T > 1.5$ GeV/c and $2.0 < \eta < 2.5$ (open circles) compared with the prediction of the PYTHIA generator with and without the inclusion of multiple interactions. . .	113

List of Tables

1.1	The three generations of fermions within the Standard Model.	2
7.1	The difference in the planar segment efficiency, determined from the weighted mean of the difference in the missing segment efficiency, between data and MC for each supermodule respectively	97
8.1	The measured differential cross section $\frac{d^2\sigma^{eP}}{dp_T^2 d\eta}$ for the production of charged particles in the η range 2.0 to 2.5.	105
8.2	The results of a QCD inspired power law fit to the inclusive charged particle spectra measured by H1 and UA1 respectively in the region $p_T > 1.5$ GeV/c.	107

Chapter 1

Introduction

Elementary particle physics is concerned with the search for a description of the fundamental structure of matter and the forces of nature. During the last couple of decades, dramatic progress has been made in this field with the advent of huge particle accelerators enabling physicists to study matter at the most fundamental level. From the confusing profusion of experimental data on particles and phenomena, a theory known as the **Standard Model** has been developed which has been able to predict successfully many of the recent precise experimental results in terms of a small number of fundamental particles and interactions.

1.1 The Standard Model

In the Standard Model, matter is believed to be constructed from a small number of fundamental, point-like fermions. The forces between these particles, with the exception of gravity, have been successfully described by the exchange of fundamental gauge bosons within the framework of **Gauge Field Theories**.

Two classes of fundamental fermions exist, known as quarks and leptons. These are arranged in three quark and lepton families. Each lepton family consists of a negatively charged particle and a corresponding neutral, massless (or very light) neutrino. A total of six types or flavours of quarks are believed to exist. The existence of the five lightest quarks has been well established by experimental measurements.

	CHARGE	GENERATIONS		
		I	II	III
QUARKS	+2/3	up	charm	top
	-1/3	down	strange	bottom
LEPTONS	-1	e	μ	τ
	0	ν_e	ν_μ	ν_τ

Table 1.1: The three generations of fermions within the Standard Model.

Recently, experimental evidence of the existence of the sixth quark, known as the ‘top’ quark, has been observed by the CDF [1] and D0 [2] collaborations in proton-antiproton collisions at the Fermilab Tevatron accelerator.

The quarks are grouped into three families consisting of a quark with electric charge $+\frac{2}{3}e$ (the *up* (u), *charm* (c), and *top* (t) quarks) and a quark with electric charge $-\frac{1}{3}e$ (the *down* (d), *strange* (s), and *bottom* (b) quarks). A ‘generation’ then consists of a family of quarks and the corresponding family of leptons, as illustrated in table 1.1. It is believed that only three generations of quarks and leptons exist. Excluding antiparticles, the Standard Model includes 12 fundamental fermions.

It is believed that all the observed, strongly interacting particles of nature (referred to as hadrons) consist of either 3 quarks (or anti-quarks), referred to as baryons, or a quark and an antiquark pair, referred to as mesons. This model of baryons and mesons (known as the static quark model) was very successful in describing observed hadronic spectroscopy.

The fundamental forces of nature are described in the Standard Model using the language of quantum field theory. At the energy scales of interest to particle physics gravity is in fact very weak and can be neglected. The remaining three forces that have been observed are electromagnetism, the weak nuclear force and finally the strong nuclear force. All the observed fundamental fermions experience the electromagnetic force (with the exception of the electrically neutral neutrinos) and the weak nuclear force. However only the quarks experience the strong nuclear

force.

Electricity and magnetism were unified into a single electromagnetic force by Maxwell in 1860. The weak nuclear force was postulated in order to explain phenomena such as β -decay. Finally the strong nuclear force was postulated as being the force that holds the atomic nucleus together.

1.1.1 Quantum Electrodynamics

Electromagnetism was the first force to be described by an accurate quantum field theory known as **Quantum Electrodynamics** or QED. In QED the electromagnetic force is mediated by the exchange of a massless gauge boson known as the photon. This is one of the most successful theories ever developed and is an example of a gauge field theory since it is based around the idea of gauge symmetry.

Quantum electrodynamics is formulated within the Lagrangian framework, in which the energy-momentum dynamics of a system is described by a Lagrangian density (often referred to as the Lagrangian). Quantum electrodynamics is based on the postulate that the Lagrangian should be invariant under an arbitrary change in the phase of the fermionic field at any point in space and time. This is known as a ‘local gauge’ transformation, as opposed to a ‘global gauge’ transformation in which a constant phase transformation is applied at all points in space and time. Whilst the initial Lagrangian of a fermionic field is invariant under a global gauge transformation, the Lagrangian is not invariant under local transformations. In order to enforce local gauge invariance, additional terms must be introduced to the Lagrangian. One of the most important discoveries of particle physics is that the resulting terms introduced to the Lagrangian correspond to a term equivalent to the Lagrangian describing the Maxwell equations of electromagnetism (the photon field), together with a term describing the interaction between the fermion and photon fields. Furthermore local gauge invariance also requires that the photon be massless.

The interaction term introduced to the Lagrangian by imposing local gauge invariance enables predictions to be made which may then be compared with ex-

perimental measurements. Calculations are performed using perturbation theory, in which each subsequent order of expansion in terms of the electromagnetic coupling constant, α , corresponds to one or more unique Feynman diagrams. Unfortunately, simple application of perturbation theory introduces divergent integrals into the calculation. However, an important property of QED is that it is ‘renormalizable’. In this procedure the divergent integrals obtained are absorbed into a redefinition of the ‘bare’ lepton charges and masses, which are in any case arbitrary, so that the new definitions are equal to the observed physical values.

Another important consequence of QED is that the electromagnetic coupling constant is in fact not a constant and instead is dependent on the energy scale of the interaction. This can be understood in terms of the cloud of virtual electron-positron pairs that surround a bare electron. The cloud of electrons and positrons will tend to be polarised, screening the bare electron charge. The more penetrating the probe into the electron structure the larger the charge of the electron will appear to be. The coupling constant is therefore referred to as a ‘running coupling constant’.

1.1.2 The Electro-Weak Interaction

After the success of the unification of electricity and magnetism, and the description of the subsequent electromagnetic force using QED, the Glashow-Weinberg-Salam model was proposed in order to describe the electromagnetic and weak interactions in a unified manner. In this model, the electromagnetic and weak interactions are considered to be aspects of the same force, and at very high energy scales have the same strength. However, as the weak interaction is mediated by the exchange of the massive W^\pm and Z gauge bosons, the force appears weak at low energies because of its short range.

Experimentally, the charged current weak interaction was found to couple to left handed fermions only, whilst the neutral current interaction is known to couple to both left and right handed fermions. The parity violating nature of the charged current interactions is accounted for by treating the left and right-handed fermions differently. The left handed fermions are grouped into weak isospin doublets, and

the right handed fermions are treated as weak isospin singlets. The electroweak interaction is then described by requiring invariance under the gauge transformation $SU(2)_L \times U(1)_Y$. The term $SU(2)_L$ refers to the gauge group of rotations in weak isospin space. The term $U(1)_Y$ corresponds to the gauge group of weak hypercharge (Y), where weak hypercharge, Y , is defined by

$$Q = T^3 + \frac{Y}{2}$$

where Q is the electric charge and T^3 is the third component of weak isospin, i.e. zero for isospin singlets and $\pm\frac{1}{2}$ for doublets. Imposing invariance of the Lagrangian under the above gauge transformation results in the introduction of four gauge fields.

A consequence of the above gauge invariance is that the observed bosons must be massless. However, the short range of the weak interactions indicates that in fact the W^\pm and Z bosons are massive with a mass $\mathcal{O}(100 \text{ GeV})$. Furthermore, if a mass term is introduced to the Lagrangian, the resulting theory is no longer renormalizable. This problem has been solved by the ‘Higgs mechanism’, in which four Higgs fields are introduced to the Lagrangian which enables the possibility of having a ‘spontaneously broken symmetry’. This means that the Lagrangian is still invariant under local $SU(2)_L \times U(1)_Y$ transformations, but in the ground state the invariance is broken enabling the gauge bosons to acquire mass. Combining three of the four Higgs fields with the weak bosons results in the massive W^\pm and Z bosons, requiring the introduction of just one additional physical boson, known as the Higgs boson. A detailed discussion of electroweak physics and the Higgs mechanism is beyond the scope of this thesis.

1.1.3 Quantum Chromo-Dynamics (QCD)

Finally, the last observed fundamental force, the strong nuclear force, is described in the language of quantum field theory by **Quantum Chromo-Dynamics** or QCD. The strong interaction acts on colour charge, analogous to the electric charge of electromagnetism. The quarks are believed to exist in three ‘colour’ states, referred to as red, green and blue. Colour was first introduced to describe the wavefunc-

tion of particles such as the Δ^{++} particle for which the combined space, spin and flavour wavefunction is symmetric under the exchange of identical fermions. However the overall wavefunction is expected to be antisymmetric. This was resolved by introducing the colour degree of freedom, with the colour wavefunction being antisymmetric, restoring the required overall antisymmetric nature of the full wave function describing the Δ^{++} baryon.

QCD is based on the gauge transformation $SU(3)_C$ of colour. The requirement of gauge invariance under such transformations leads to the introduction of an octet of bi-coloured (i.e. carrying colour-anticolour quantum numbers) gauge bosons known as gluons. The fact that the resulting gluons themselves carry colour implies that the gluons also experience the strong interaction. This is referred to as the non-Abelian nature of QCD.

The non-Abelian nature of QCD has important consequences for calculations performed using perturbation theory. In analogy to QED, the strength of the strong interaction is described by the strong coupling constant, α_s , which again is a running coupling constant. However, due to the non-Abelian nature of QCD, the cloud of gluons surrounding a quark has the opposite effect to the cloud of electrons and positrons surrounding a bare electron. Instead of screening the colour charge of the quark, the effective colour charge of the quark increases with increasing distance (or equivalently decreasing four momentum transfer Q^2). This is believed to be the reason why free quarks have not been observed and instead quarks are always confined within colourless hadrons. However, as $Q^2 \rightarrow \infty$ the strong coupling constant decreases and the quarks appear to be weakly interacting. This is known as ‘asymptotic freedom’. Consequently, QCD can only be solved using perturbation theory for high momentum transfers ($Q^2 > \mathcal{O}(\text{a few GeV}^2)$). As a result, though the basic interactions involved in many high energy scattering experiments can be calculated using perturbative QCD, the production of the final state hadrons seen in the detector cannot be calculated, and instead phenomenological models are required to describe the resulting hadronisation process.

Chapter 2

Physics at HERA

2.1 Introduction

Throughout the history of physics, scattering experiments have been crucial to the development of our understanding of the fundamental structure of matter and the forces of nature. Early scattering experiments by Rutherford using α particles led directly to the discovery of the nucleus. Later experiments by Hofstadter using electrons led to the measurement of the sizes of various nuclei and the observation of proton constituents within the helium nucleus[3]. Observations of point-like partons within the proton itself have resulted from the scattering of leptons (e, μ, ν) at various fixed target experiments [4]. The experiments H1 and ZEUS, using the HERA accelerator at DESY, are the latest in this chain of experiments and have the potential to extend our understanding of the structure of matter and the fundamental forces of nature still further.

2.2 Electron-Proton Scattering at HERA

At HERA energies, electron-proton (ep) scattering is dominated by the inelastic scattering process :

$$e^-(k) + p(P) \longrightarrow e^-(k') + X$$

where X is the hadronic final state. The four momentum transfer squared, Q^2 , is defined as

$$Q^2 \equiv -q^2 = -(k - k')^2 \quad (2.1)$$

where q is the four momentum of the virtual exchange particle. By convention, the above definition is used so that Q^2 is a positive quantity. Such interactions, in which the exchanged boson is either a virtual photon or Z^0 , are referred to as ‘Neutral Current’ (NC) interactions.

Interactions in which a W^- boson is exchanged of the general form

$$e^- + p \longrightarrow \nu_e + X$$

are also possible and are referred to as ‘Charged Current’ (CC) interactions. Interactions involving the exchange of a Z^0 or W^- are only significant at high Q^2 as the cross section is suppressed by the factor

$$\frac{\sigma(Z^0, W^-)}{\sigma(\gamma)} \propto \left| \frac{Q^2}{Q^2 + M_{Z^0, W^-}^2} \right| \quad (2.2)$$

with respect to photon exchange.

High Q^2 ($Q^2 > \mathcal{O}(4 \text{ GeV}^2)$) interactions are referred to as ‘Deep Inelastic Scattering’ (DIS). Interactions in which the momentum transfer is small ($Q^2 < \mathcal{O}(1 \text{ GeV}^2)$), mediated by the exchange of a quasi-real photon, are referred to as ‘photoproduction’.

2.3 Deep-Inelastic Scattering

The kinematics of deep inelastic scattering can be described at any given centre of mass energy by two independent variables. An example could be the energy and scattering angle of the scattered lepton. However, it is convenient to work in terms of the Lorentz invariant quantities Q^2 and x , the Bjorken scaling variable, defined as

$$x \equiv Q^2 / (2P \cdot q). \quad (2.3)$$

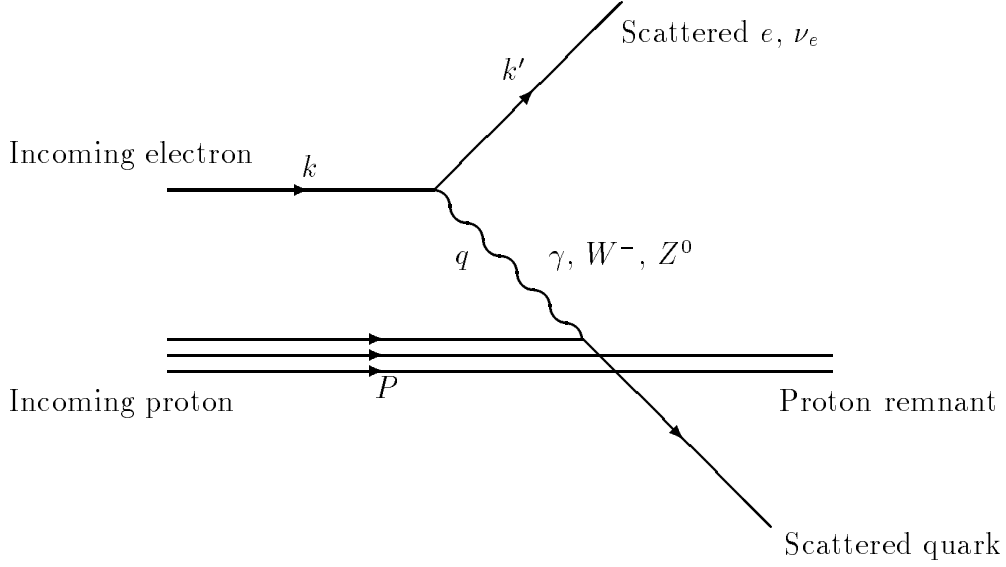


Figure 2.1: A schematic representation of deep inelastic scattering in lowest order QCD and QED.

Additional useful variables are

$$y \equiv (P \cdot q) / (P \cdot k) \quad (2.4)$$

and

$$W^2 \equiv (q + P)^2 \quad (2.5)$$

the invariant mass of the hadronic final state. A schematic representation of a deep inelastic ep interaction in lowest order QCD and QED is shown in figure 2.1.

The Bjorken scaling variable, x , can be interpreted as the fraction of the proton's momentum carried by the struck quark in the infinite momentum frame of the proton [5]. The variable y can be interpreted as the fraction of the incident lepton's energy transferred to the proton, measured in the rest frame of the incident proton. The variables Q^2 , x and y are related by the equation

$$Q^2 = sxy \quad (2.6)$$

where s is the squared centre of mass energy given by

$$s \equiv (k + P)^2 \simeq 4E_e E_p \quad (2.7)$$

and E_e and E_p are the electron and proton beam energies respectively.

At the energies available at the HERA accelerator it is possible to make measurements at much higher values of Q^2 (up to $\mathcal{O}(10^4)$ GeV²) and, equally importantly, at much lower values of x than otherwise possible at fixed target experiments.

2.3.1 The NC Deep Inelastic Cross Section

The total differential neutral current deep inelastic cross section can be expressed as :

$$\frac{d^2\sigma_{tot}}{dx dQ^2} = \frac{d^2\sigma_B}{dx dQ^2} + \frac{\alpha}{2\pi} \frac{d^2\sigma_1}{dx dQ^2} + \mathcal{O}(\alpha^2) \quad (2.8)$$

where the first term represents the Born cross section and the second and third terms represent the electro-weak radiative corrections to the Born cross section. In order to determine the Born cross section, the effect of radiative corrections must be accounted for. The largest contribution to the difference between the measured cross section and the Born cross section is due to initial state radiation, in which the incoming electron emits a real photon before interacting with the proton. For such events, the kinematics determined at the electron vertex are not the true kinematics of the ep interaction.

The Born cross section can be expressed in terms of two independent functions, $F_1^P(x, Q^2)$ and $F_2^P(x, Q^2)$, known as structure functions, by the equation

$$\frac{d^2\sigma_B}{dx dQ^2} = \frac{4\pi\alpha^2}{xQ^4} \left[y^2 x F_1^P(x, Q^2) + (1-y) F_2^P(x, Q^2) \right] \quad (2.9)$$

2.3.2 The Quark-Parton Model

In the quark-parton model, deep inelastic scattering is viewed as a two stage process. In the first stage, the virtual exchanged photon interacts with a quark within the proton, which over the short time scale of the interaction is assumed to be free. In the second stage of the process the outgoing partons hadronise to produce a ‘current jet’ of hadrons due to the struck quark, and a proton remnant.

The Born cross section can then be expressed in terms of the cross section for

electron-quark scattering by the equation

$$\frac{d^2\sigma_B}{dx dQ^2} = \frac{4\pi\alpha^2}{xQ^4} \sum_q \int_0^1 d\xi f_q(\xi) e_q^2 \frac{x}{2} [1 + (1-y)^2] \delta(x-\xi). \quad (2.10)$$

Equating equations 2.9 and 2.10 the following relationships are obtained :

$$F_2^P = 2xF_1^P \quad (2.11)$$

$$F_2^P = \sum_q e_q^2 x f_q(x) \quad (2.12)$$

It can be seen that, in the quark parton model, the structure function F_2^P is only dependent on the Bjorken scaling variable, x , and not on Q^2 . This is known as Bjorken Scaling[6]. Equation 2.11 is known as the Callan-Gross relationship.

Within the framework of the quark parton model, if the total momentum of the proton was carried by the proton's quark constituents, then the momentum sum rule

$$\sum_i \int_0^1 dx x f_i(x) = 1 \quad (2.13)$$

would be expected to be true, where the sum is over all quark flavours. However, early measurements at SLAC [7] found that this relationship was not true with only approximately 50% of the total momentum of the proton being carried by the quark constituents. This was the first direct evidence for the existence of gluons within the proton.

2.3.3 Scaling Violations

In DIS measurements at previous fixed target experiments, Bjorken Scaling has been observed to be approximately true for $x \approx 0.15$. However, significant scaling violations have been observed at both lower and higher values of x . Such scaling violations can be predicted using the QCD improved quark-parton model. In QCD it is possible for a quark to radiate a gluon and for the gluon subsequently to split into a $q\bar{q}$ pair. At low Q^2 this structure is not resolved, however as the Q^2 of the probe is increased the structure is observed. Consequently, at high Q^2 there is an increased probability to observe a parton with a low value of x and conversely a

reduced probability to observe a parton with a high value of x . Therefore, at fixed x the proton structure function F_2 will increase (decrease) with increasing Q^2 for low (high) x respectively. This leads to the ‘ Q^2 contraction’ of the measured structure function.

The scaling violations can be predicted within the framework of perturbative QCD (pQCD) using the Altarelli-Parisi evolution equations [8] in which the evolution of the quark distribution functions, $q_i(x, Q^2)$, are given by

$$\frac{dq_i(x, Q^2)}{d \log Q^2} = \frac{\alpha_s}{2\pi} \int_x^1 \frac{dz}{z} \left(q_i(z, Q^2) P_{qq} \left(\frac{x}{z} \right) + g(z, Q^2) P_{qg} \left(\frac{x}{z} \right) \right) \quad (2.14)$$

where $g(x, Q^2)$ is the gluon distribution function which evolves with Q^2 according to the equation

$$\frac{dg(x, Q^2)}{d \log Q^2} = \frac{\alpha_s}{2\pi} \int_x^1 \frac{dz}{z} \left(\sum_i q_i(z, Q^2) P_{gq} \left(\frac{x}{z} \right) + g(z, Q^2) P_{gg} \left(\frac{x}{z} \right) \right). \quad (2.15)$$

The splitting function $P_{qq}(\frac{x}{z})$ gives the probability that a quark with momentum fraction z ($z > x$) will radiate a gluon giving a quark with momentum fraction x and can be calculated from pQCD. Equation 2.14 also includes a term due to the possibility of a gluon splitting into a $q\bar{q}$ pair (P_{qg}). Similarly, the evolution equation for the gluon distribution function includes two terms corresponding to the probability for a quark to radiate a gluon (P_{gq}) and the probability for a gluon to radiate a gluon (P_{gg}) due to the triple gluon vertex.

The Altarelli-Parisi equations therefore give a set of coupled differential equations, which given the quark distribution functions at a given $Q^2 = Q_0^2$ can be solved to determine the evolution of the quark distribution function for all $Q^2 > Q_0^2$. Generally, an analytical form of the parton distribution function at the input scale is used, the free parameters of which are then fitted by comparing with the measured structure functions.

2.4 Photoproduction

Though the primary interest at HERA may be with high Q^2 deep inelastic scattering, the ep cross section at HERA is in fact dominated by low Q^2 photoproduction events

in which the interaction is mediated by a quasi-real photon. Photoproduction is however very interesting in its own right and offers a rich potential for physics analysis. Photoproduction offers an ideal testing ground for QCD in both the perturbative and non-perturbative regimes. In particular, the study of high p_T photoproduction with the production of jets enables the determination of the partonic structure of the photon.

For photoproduction events, the electron vertex can be treated to a good approximation by the ‘equivalent photon approximation’ (EPA). In this approximation, the cross section is factorised into the flux factor to describe the probability for a photon to be emitted at the electron vertex multiplied by the γp cross-section for real photons. Using the Weizacker-Williams approximation [9] the incident electron beam can be considered as a source of real photons with a flux given by

$$\frac{d^2 f}{dy dQ^2} = \frac{\alpha}{2\pi Q^2} \left(\frac{1 + (1-y)^2}{y} - \frac{2m_e^2 y}{Q^2} \right). \quad (2.16)$$

A discussion of the limitations of the Weizacker-Williams approximation and photon flux calculations in general can be found in [10, 11] and [12]. Consequently the measured photoproduction cross section can be related to the total γp cross-section using the relationship

$$\frac{d^2 \sigma_{ep}}{dy dQ^2} = \frac{\alpha}{2\pi Q^2} \left(\frac{1 + (1-y)^2}{y} - \frac{2m_e^2 y}{Q^2} \right) \sigma_{\gamma p}^{tot}(ys). \quad (2.17)$$

Several different mechanisms contribute to photoproduction at HERA energies. To first approximation, a real photon is a fundamental pointlike particle. However, through its direct coupling to quarks, a real photon has the possibility to split into a $q\bar{q}$ pair. The $\gamma \rightarrow q\bar{q}$ fluctuation may have varying virtualities, which can be characterised by the common p_T^2 of the q and \bar{q} with respect to the photon direction. When the virtuality is small a vector meson wave function description may be a good approximation. This is the basis behind the vector dominance model (VDM) [13, 14] in which the photon couples to a hadronic vector particle with the same quantum numbers as the photon, which in turn interacts strongly with the proton.

In the VDM model it is postulated that the photon wavefunction is a superposition of a bare photon component, $|\gamma_B\rangle$, and a hadronic component,

$\sqrt{\alpha} | h \rangle,$

$$|\gamma\rangle = \sqrt{Z_3} |\gamma_B\rangle + c\sqrt{\alpha} |h\rangle \quad (2.18)$$

where $Z_3 = 1 - c^2\alpha$ assures proper normalisation. At fixed target energies, the general features of photoproduction interactions have been found to be remarkably similar to hadronic interactions, for example πN interactions. This implies that the bare photon interactions can only account for a small fraction of the total photoproduction cross section: the smallness of the $\sqrt{\alpha} | h \rangle$ component is more than compensated by the intrinsically much larger hN cross section. In the VDM model, interactions involving the bare photon component are neglected. Furthermore it is postulated that the three vector mesons ρ^0, ω and ϕ are the sole hadronic constituents of the photon, based on their copious photoproduction. The inclusion of heavier constituents is referred to as generalised vector dominance (GVD) [15].

The VDM model has been successfully applied in describing photoproduction at fixed target energies and has illustrated the similarity between photoproduction and hadron-hadron interactions. In hadronic physics, interactions can be separated into several different event classes such as elastic, diffractive and non-diffractive events. This classification can be extended naturally to the VDM model.

The elastic process $V + p \rightarrow V + p$ generalises to the ‘VDM elastic’ process¹

$$\gamma + p \rightarrow V + p \quad (2.19)$$

The VDM single and double diffractive processes are correspondingly

$$\gamma + p \rightarrow V + X \quad (2.20)$$

$$\gamma + p \rightarrow X + p \quad (2.21)$$

$$\gamma + p \rightarrow X_1 + X_2 \quad (2.22)$$

where for case 2.22 the event is characterised by a large rapidity gap between the photon and proton dissociative systems. The remaining events,

$$\gamma + p \rightarrow X \quad (2.23)$$

¹The truly elastic (Compton) process $\gamma + p \rightarrow \gamma + p$ is $\mathcal{O}(\alpha^2)$ and can safely be neglected.

where the hadronic system X does not contain any significant rapidity gaps, are referred to as non-diffractive events.

The non-diffractive photoproduction cross-section is dominated by ‘soft’ events leading to low p_T particle production. However, the observation of the production of high p_T particles and the production of jets in photoproduction has clearly shown that there is also a hard component to the non-diffractive cross section. Two components contribute to this hard component of the cross-section. Firstly the photon, as the gauge particle mediating the electromagnetic interaction, can interact directly with a parton from the proton. This class of events is known as ‘direct photoproduction’. The second contribution occurs when the photon is resolved into a hadronic system, and a hard scattering occurs between a parton from the photon and a parton from the proton. Such interactions are called ‘resolved photoproduction’.

The direct contribution to the non-diffractive cross-section can be calculated using perturbative QCD. Resolved photoproduction includes a component due to the VDM contribution. However, the pointlike coupling of the photon to quarks also leads to a contribution where the photon splits into a $q\bar{q}$ pair, at relatively high virtuality, without forming a bound state. This additional mechanism is referred to as the ‘anomalous’ contribution to the photoproduction cross-section [16, 17, 18]. Figure 2.2 shows the typical direct, VDM and anomalous contributions to the hard non-diffractive cross section.

2.4.1 The Photon Structure Function

The above interpretation of the structure of the photon and its interactions leads to the introduction of parton distribution functions within the photon. The hadronic structure of the photon has been studied at e^+e^- colliders in $\gamma^*\gamma$ interactions. The real γ is radiated by an electron scattered at a small angle, whilst the highly virtual photon γ^* is ‘radiated’ by an electron scattered at a large angle in the detector. In analogy to the measurement of the structure of the proton in deep inelastic ep scattering, the resulting differential cross section can be expressed in terms of the photon structure functions F_1^γ and F_2^γ [19]. The resulting differential cross section

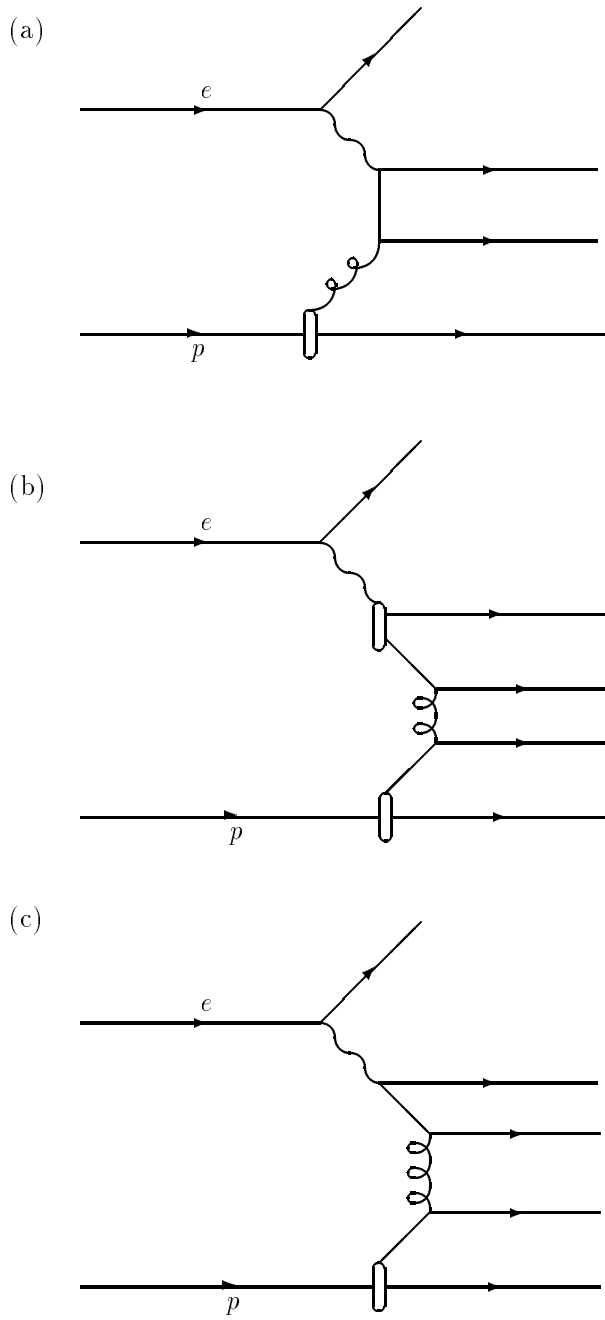


Figure 2.2: A schematic representation of the typical (a) direct, (b) VDM and (c) anomalous contributions to the hard non-diffractive photoproduction cross section.

for the interaction $e\gamma \rightarrow eX$ where X is any hadronic final state is then given by

$$\frac{d^2\sigma(e\gamma \rightarrow eX)}{dx dQ^2} = \frac{4\pi\alpha^2}{xQ^4} \left[y^2 x F_1^\gamma(x, Q^2) + (1-y) F_2^\gamma(x, Q^2) \right]. \quad (2.24)$$

The evolution of the photon structure functions from a given input scale, Q_0^2 , to higher Q^2 can then be calculated in a similar manner to F_2^P using the Altarelli-Parisi equation with the inclusion of a term to account for the anomalous contribution to the photon structure function [20].

The situation is consequently very similar to the case of nucleonic parton densities. However, the determination of the input distributions is much more difficult in the case of the photon. In particular, no momentum sum rules apply for the photon and it is consequently difficult to derive reliable information on the gluon content of the photon. Furthermore, the $e\gamma \rightarrow eX$ event rate in e^+e^- interactions is quite small; most recent measurements are based typically on around 1,000 events at $Q^2 \simeq 5 \text{ GeV}^2$ [21, 22, 23]. This can be compared with millions of events in, for example, deep-inelastic μN scattering.

Several parameterisations of the parton distribution functions of the photon exist. In particular, three leading order (LO) parton distribution sets have been produced by Levy, Abramowicz and Charchula (LACI-III) [24], and leading order and next to leading order (NLO) parton distribution sets have been produced by Gluck, Reya and Vogt (GRV-LO and GRV-NLO) [25].

The LAC parton distributions are based on the QCD evolution of input distributions at $Q_0^2 = 4 \text{ GeV}^2$ (LACI and LACII) and $Q_0^2 = 1 \text{ GeV}^2$ (LACIII) respectively. An analytical form of the input distribution at Q_0^2 was assumed with a total of 12 free parameters. The free parameters were then determined by a fit to all experimental data on F_2^γ above the initial value, Q_0^2 . The set LACII was produced with one less free parameter. The resulting parton distribution functions illustrate the poor constraint on the gluon content of the proton provided by data on F_2^γ . In particular the LACIII parameterisation predicts a very hard gluon content, with a maximum at $x \simeq 0.9$, whilst the LACI and LACII parameterisations predict very soft gluon distributions, rising very steeply at low x .

The GRV parton distribution functions (GRV-LO and GRV-NLO) are based on the QCD evolution of input distributions at a very low Q_0^2 (0.25 GeV² in LO, 0.3 GeV² in NLO). The approach is based on the same philosophy as used in the previous fits of protonic and pionic parton densities by the same authors. In the case of the proton, it was initially hoped that the complex structure of the proton could be generated dynamically from a valence quark distribution at the chosen input scale. However, whilst the gluon density was found to evolve sufficiently to carry approximately half of the proton's momentum at Q^2 of a few GeV², the gluon distribution was found to be too soft in shape. Consequently 'valence-like' gluon and sea quark densities had to be introduced even at the input scale. Similarly the pionic input distributions also included a 'valence-like' gluon density, though no sea quarks were introduced at the input scale.

The GRV parton distribution functions for the photon were subsequently obtained by using input distributions of the form

$$\vec{q}_{0,GRV}^\gamma(x) = \kappa \frac{4\pi\alpha_{em}}{f_\rho^2} \vec{q}_{0,GRV}^\pi(x) \quad (2.25)$$

where $\vec{q}_{0,GRV}^\pi(x)$ are the corresponding input distribution functions used for case of the pion. The use of the above input distributions is motivated by VDM considerations, where f_ρ^2 determines the $\gamma \rightarrow \rho$ transition probability. The constant κ is introduced to allow for the contribution of heavier vector mesons, and is a free parameter in the subsequent fit to the available data. Equation 2.25 is an assumption which must be tested experimentally; in particular it is not clear that the parton densities in a pion are similar to those of a vector meson, or that pQCD is applicable at such low scales.

A general review of the theoretical uncertainties in the current knowledge of the photon structure functions can be found in [18].

2.4.2 The Total Photoproduction Cross Section

The total photoproduction cross-section has been measured by both the H1 and ZEUS collaborations at centre of mass energies of $\sqrt{s} \simeq 200$ GeV. Using the data

collected in the 1992 data taking period, the total photoproduction cross section was measured by the H1 collaboration as

$$\sigma_{tot}^{\gamma p} = 159 \pm 6.6(stat) \pm 20(sys)\mu b \quad (2.26)$$

where the first error is statistical and the second error is systematic [26]. The measurement is consistent with the total cross section determined by the ZEUS collaboration [27]. However, in order to determine the cross section a model dependence is introduced as the acceptance corrections are sensitive to the expected contribution to the cross section of the various event classes discussed above.

Using a data sample collected during a short dedicated running period in 1994, the H1 collaboration has attempted to reduce the systematic error in the above measurement by measuring the elastic and diffractive contributions to the total cross section[28]. The total cross section was then determined as

$$\sigma_{tot}^{\gamma p} = 165 \pm 2(stat) \pm 11(sys)\mu b. \quad (2.27)$$

The resulting cross section is only then dependent on the assumed rate of the double diffractive contribution to the total cross section. The measurement shows the typical increase in the total cross section at high energies compared with previous measurements using fixed target experiments at $\sqrt{s} \leq 18$ GeV, as observed in hadronic interaction cross sections.

Predictions of the dependence of the total cross section in photoproduction are based on two main approaches: (i) Regge-type model predictions and (ii) QCD-based predictions in ‘mini-jet’ models.

In Regge theory [29] the high-energy behaviour of a two-body amplitude due to the exchange of a Regge pole is given by

$$A(s, t) \sim s^{\alpha(t)} \quad (2.28)$$

where $\alpha(t)$ is the relevant Regge trajectory. Using the optical theorem the total cross section is related to the imaginary part of the forward scattering amplitude, giving

$$\sigma_{tot} \sim s^{\alpha(0)-1} \quad (2.29)$$

where $\alpha(0)$ is the intercept of the Regge trajectory

The Regge pole carrying the quantum numbers of the vacuum is called the Pomeron, while all other poles are referred to as Reggeons. The total cross section for the hadronic interaction $A + B \rightarrow X$ can then be described by the general form

$$\sigma_{tot}^{AB} = X^{AB} s^{\alpha_P(0)-1} + Y^{AB} s^{\alpha_R(0)-1}. \quad (2.30)$$

The constants $\alpha_P(0)$ and $\alpha_R(0)$ are believed to be universal, with a recent fit to measured hadronic cross sections [30] finding $\alpha_P(0) = 1.0808$ and $\alpha_R(0) = 0.5475$. The coefficients X^{AB} and Y^{AB} are process dependent, and must be determined by a fit to previous cross section measurements for the process under consideration. A recent fit to photoproduction data below 20 GeV gives a predicted cross section at 200 GeV of $160 \mu b$ [17], which is consistent with the measured cross section determined by the H1 and ZEUS collaborations.

In the second class of predictions on the total photoproduction cross section, the increase in the total cross section in hadronic interactions at high centre of mass energies is interpreted as due to the increase in the cross section for the production of two (mini-)jets in the framework of pQCD [31, 32]. In LO pQCD, parton parton scattering leads to the production of two outgoing jets. The scale that is used to determine the point at which perturbative calculations are applicable is usually taken as the transverse momentum squared (p_T^2) of the outgoing partons. The di-jet cross section is given by pQCD as

$$\frac{d\sigma_{\gamma p}^{jet}}{dp_T^2} = \sum_{i,j,k} \int dx_\gamma \int dx_p \int d\hat{t} f_i^\gamma(x_\gamma, \mu^2) f_j^p(x_p, \mu^2) \frac{d\hat{\sigma}_{ij}^k}{d\hat{t}} \delta\left(p_T^2 - \frac{\hat{t}\hat{u}}{\hat{s}}\right) \quad (2.31)$$

where $f_i^{\gamma,p}$ are the parton distribution functions and $\hat{\sigma}$ is the partonic scattering cross section. Consequently the total di-jet cross section above a given $p_T = p_{T,min}$ is then given by

$$\sigma_{\gamma p}^{jet}(p_{T,min}) = \int_{p_{T,min}^2}^{s/4} \frac{d\sigma^{jet}}{dp_T^2} dp_T^2. \quad (2.32)$$

It is reasonable that an effective $p_{T,min}$ cut should be applied since the incoming hadrons are colour neutral objects and when the p_T of the exchanged gluon (say) is small and the transverse wavelength correspondingly large, the gluon can no longer

resolve the individual colour charges, and the effective coupling is decreased. This mechanism cannot be predicted by pQCD calculations, which are always performed assuming the scattering of free partons, but is also not in contradiction with pQCD.

If $\sqrt{s} \gg p_{T,min}$ equation 2.32 receives its dominant contribution from $x_{\gamma,p} \ll 1$. The parton density functions can then be approximated by a simple power law, $f_i^\gamma, f_j^p \propto x^{-J}$ where the power J is expected to lie roughly in the range $1.2 \leq J \leq 1.5$. The total di-jet therefore cross section scales at high (asymptotic) energies like [33]

$$\sigma_{\gamma p}^{jet}(p_{T,min}) \propto \frac{1}{p_{T,min}^2} \left(\frac{s}{4p_{T,min}^2} \right)^{J-1} \log \frac{s}{4p_{T,min}^2}. \quad (2.33)$$

The cross section will therefore grow much faster than the total γp cross section, which only grows $\propto \log^2 s$ (Froissart bound [34]). Eventually the jet cross section will therefore exceed the total γp cross section.

This apparent problem is solved by the observation that pQCD is performed assuming free partons, whilst the incoming hadrons can be viewed as beams of partons. Consequently a multiplicity factor can be introduced. Since each partonic scattering leads to a pair of (mini-)jets the following relationship is obtained :

$$\sigma_{ab}^{jet} = \langle n_{jetpairs} \rangle \sigma_{ab}^{inel}. \quad (2.34)$$

This is known as multiple scattering and can be included within the eikonal formalism. In this approach the eikonal $\chi(b, s)$ is introduced, where χ is identified as the mean density of hard scatters for collisions at impact parameter b . χ is assumed to be of the form

$$\chi(b, s) = \frac{A(b)\sigma^{jet}(s)}{P_{had}} \quad (2.35)$$

where $A(b)$ describes the overlap of partons within the colliding particles in impact parameter space and P_{had} is the probability that both initial particles are in a hadronic state when they interact. The overlap function $A(b)$ is usually taken as a convolution of the electromagnetic form factors of the incident particles and P_{had} is expected to be $\sim 4\pi\alpha_{em}/f_\rho^2 (\simeq 1/300)$. If the multiple partonic interactions are assumed to be independent at a fixed impact parameter, then the probability that no hard scattering should occur is given by Poisson statistics as $e^{-\chi(b,s)}$. The total

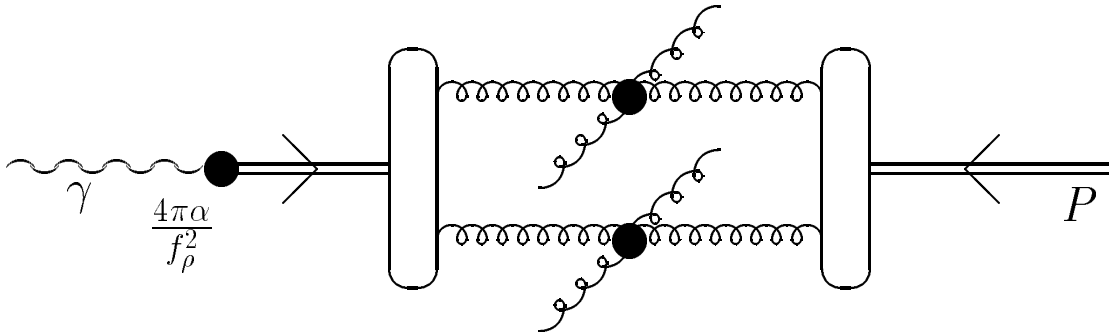


Figure 2.3: An example of multiple parton scattering in γp interactions.

cross section is then given by

$$\sigma_{tot}^{pQCD} = P_{had} \int_0^\infty \pi db^2 [1 - \exp(-\chi(b, s))] \quad (2.36)$$

which has manifestly taken into account the possibility of more than one hard scatter per interaction, illustrated in figure 2.3

In realistic analyses of the total photoproduction cross section a non-perturbative contribution to the eikonal is introduced:

$$\chi(b, s) = \frac{A(b) [\sigma^{soft} + \sigma^{jet}(s)]}{P_{had}} \quad (2.37)$$

with the soft cross section often parameterised as

$$\sigma^{soft}(s) = \sigma_0 + \frac{\sigma_1}{\sqrt{s}} \quad (2.38)$$

where σ_0 and σ_1 are constants. Therefore including $p_{T,min}$ three free parameters (beyond those describing high p_T jet production) are available to fit the total photoproduction cross section.

Extreme predictions from mini-jet models are excluded by the recent measurements of the total photoproduction cross section. However, minijet jet predictions

could be consistent with the measured cross section provided a $p_{T,min}$ value of about 2 GeV/c is chosen.

Jets with a transverse momentum of $\mathcal{O}(1-3 \text{ GeV}/c)$ are referred to as mini-jets. Recently the TOPAZ and AMY collaborations unambiguously observed [35] mini-jets in $\gamma\gamma$ collisions at TRISTAN. These data, as well as other data on multi-hadron production in $\gamma\gamma$ scattering [36] imply that partonic collisions with transverse momenta in the GeV range occur at the rate predicted by pQCD. A detailed review of the uncertainties in recent predictions of the total photoproduction cross section based on mini-jet models can be found in [37, 38].

It should be emphasised that it is not possible to determine the presence of multiple parton-parton interactions by an analysis of the total cross section alone. In particular, the measured cross section can equally well be described by Regge parameterisations as discussed above.

2.4.3 Jet Production

The production of high p_T jets offers the largest cross-section of all hard γp scattering reactions. Consequently, the production of jets in photoproduction has been the focus of much of the early analysis by the H1 [39, 40, 41, 42] and ZEUS [43, 44, 45, 46] collaborations at HERA. In LO pQCD, hard photoproduction leads to the production of two outgoing partons leading to the production of two jets at the experimental level.

The kinematics of a typical resolved photoproduction event is shown in figure 2.4. The variables x_γ and x_P are the momentum fraction of the parton from the photon and proton respectively. For events with two well reconstructed jets it is possible to reconstruct x_γ and x_P from the measured transverse energy, E_T , and pseudorapidity, η , of the reconstructed jets using the equations

$$x_\gamma = \frac{E_T^1 \exp(-\eta_1) + E_T^2 \exp(-\eta_1)}{2E_\gamma} \quad (2.39)$$

$$x_P = \frac{E_T^1 \exp(\eta_1) + E_T^2 \exp(\eta_1)}{2E_P}. \quad (2.40)$$

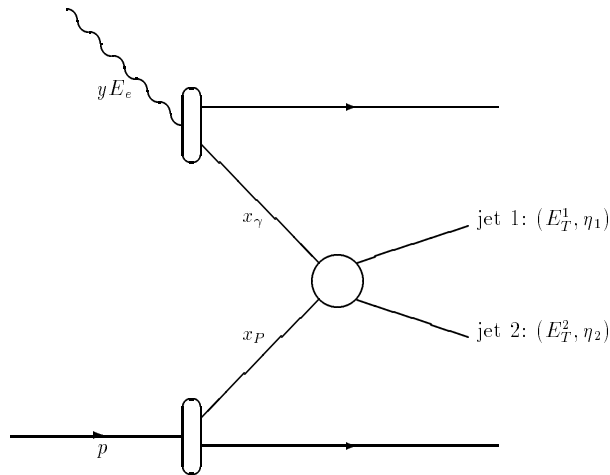


Figure 2.4: The kinematics of a typical LO resolved photoproduction event. The production of two outgoing partons leads to the observation of two hadronic jets in the event, characterised by their transverse energy, E_T , and pseudorapidity, η .

As described in the previous section it is possible for multiple interactions to occur in resolved photoproduction. The presence of multiple interactions should lead to observable features in hard photoproduction events. In particular the presence of additional mini-jets or soft activity in the event leads to an increased ‘jet pedestal’, where the term jet pedestal refers to the energy flow away from the jet axis. The increased jet pedestal should also contribute additional energy to the jet, leading to an increased inclusive jet rate. The situation is however complicated as other effects such as initial and final state radiation and fragmentation also contribute to the energy flow in such events. A detailed discussion of jet production and the evidence for multiple interactions is presented in chapter 6.

The description of the energy flow in hard photoproduction is also important in order to enable the observed distribution of x_γ to be unfolded back to the true distribution in order to study the photon structure function. The gluon density in the photon has been studied by the H1 collaboration [41] by subtracting the contribution due to direct photoproduction (concentrated at high x_γ) and resolved

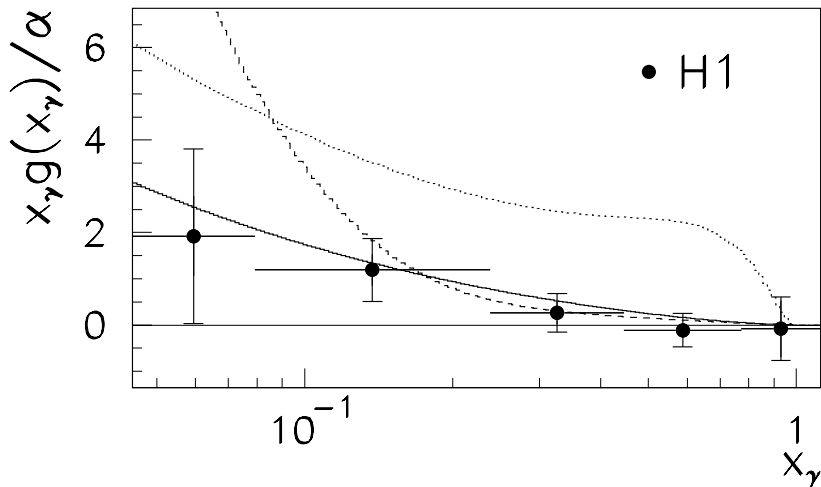


Figure 2.5: The gluon density of the photon divided by the fine structure constant $\alpha=1/137$ (data: circles) at the scale $\langle p_T \rangle^2=75 \text{ GeV}^2$. For comparison the GRV-LO (full) and the LACI (dashed) and the LACIII (dotted) parameterisations are shown. From [41]

photoproduction events initiated by a quark from the photon from the unfolded x_γ distribution. The gluon density of the photon has then been measured at a scale of $\langle p_T \rangle^2=75 \text{ GeV}^2$ and is shown in figure 2.5 compared with predictions from the GRV-LO, LACI and LACIII parameterisations. It can be seen that the LACIII prediction of a very hard gluon density in the photon is ruled out by the measurement. The LACI distribution, giving a very steeply rising gluon density at low x_γ , is also not favoured, whilst the GRV-LO predictions give reasonable agreement with the data. For this reason, in the analysis presented in this thesis the GRV-LO parton distribution functions for the photon have been used in order to describe photoproduction interactions using Monte Carlo generators.

The above determination of the gluon density within the photon has been obtained by applying a jet pedestal subtraction method, as a full description of the energy flow in such events has not yet been achieved. A quite large model dependence is therefore introduced into the result. In order to improve the determination

of the parton distribution functions in the photon from HERA data, a thorough description of the energy flow in such events is required. Consequently, the study of the presence of multiple interactions in photoproduction at HERA energies is essential for practical purposes, in addition to the theoretical interest in multiple interactions. This has been the motivation for much of the analysis presented in this thesis.

Chapter 3

The H1 Detector

3.1 The HERA accelerator

The HERA accelerator at DESY in Hamburg is the first electron-proton storage ring to be constructed. It is designed to accelerate 210 bunches of electrons (or positrons) and 210 bunches of protons to 30 GeV and 820 GeV respectively in two independent storage rings housed in a tunnel of circumference 6.3 km. The electron and proton bunches are arranged to intersect at four interaction points, two of which house the general purpose detectors H1 and ZEUS.

The layout of the HERA accelerator and pre-accelerators is shown in figure 3.1. The design of the electron and proton storage rings differ due to the respective limiting factors. For electrons the beam energy is limited by synchrotron radiation. However, for protons the effect of synchrotron radiation is negligible, and consequently the proton beam energy is limited by the magnetic field attainable in the bending magnets. Therefore, the electron ring uses conventional magnets operating at room temperature whilst the proton ring uses superconducting magnets. The proton beam is accelerated by a series of warm 52 and 208 MHz RF cavities in order to achieve the design beam energy and the electron beam is accelerated by a series of 82 warm cavities and 16 superconducting cavities.

Luminosity was first achieved at HERA during 1992. For the first year of running HERA operated with 10 electron and proton bunches, with the bunch crossing

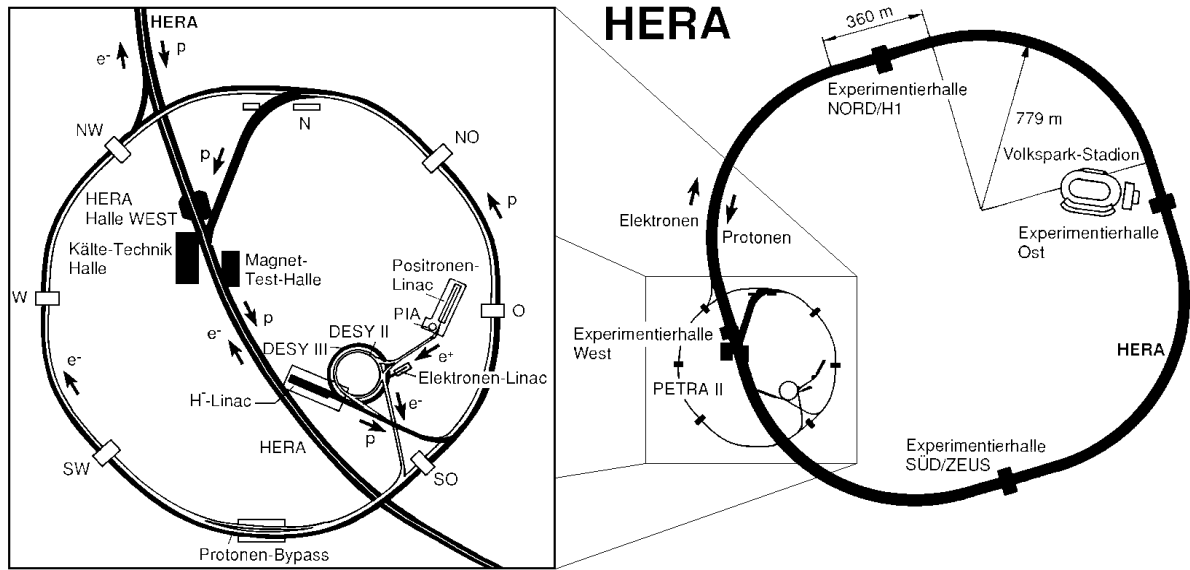


Figure 3.1: The layout of the HERA accelerator and pre-accelerators.

interval set at the design value of 96 ns. However only 9 of the electron and proton bunches were collided. The 10th bunch in both the electron and proton beams were separated, such they did not have a colliding partner. The non-colliding bunches, referred to as pilot bunches, enable beam induced backgrounds to be studied. The 1992 data taking period yielded an integrated luminosity of approximately 30 nb^{-1} . For the 1993 data taking period several improvements enabled HERA to operate with 84 colliding electron and proton bunches, and 6 proton and 10 electron pilot bunches. A total integrated luminosity of 880 nb^{-1} was delivered.

3.2 The H1 Detector

In order to realise the potential of the HERA accelerator, the H1 detector has to satisfy certain basic criteria. The identification and measurement of electrons plays a crucial role in the physics at HERA, and consequently the H1 detector must be able to facilitate this. The detector must have good electromagnetic and hadronic energy resolution in order to study inclusive energy flow measurements both in DIS

and photoproduction. It is important that the detector is as hermetic as possible to facilitate the measurement of missing transverse energy, in order to select and study charged current DIS events. Muon identification and energy resolution must be excellent in order to allow the study of interactions that produce heavy flavours, as well as to allow the search for new particles.

An accurate determination of the luminosity is required, and this must also include the facility to study photoproduction via the tagging of low angle electrons produced in low Q^2 interactions. Finally a beam crossing occurs at the H1 detector every 96 ns, and consequently sophisticated triggers are required in order to select physics events from the large numbers of beam-gas and beam-wall background interactions, and to distinguish between different physics classes.

The layout of the H1 detector is shown in figure 3.2. A right-handed Cartesian coordinate system (x, y, z) is used, where z is the direction of the proton beam, y is vertical and the origin is at the nominal interaction point. A spherical polar coordinate system (r, θ, ϕ) is defined in the conventional way with reference to the Cartesian coordinate system, such the $\theta = 0^\circ$ is the proton direction. The regions $\theta < 90^\circ$ and $\theta > 90^\circ$ are referred to as the ‘forward’ and ‘backward’ region respectively.

The main components of the H1 detector, as operational for the 1993 data taking period, are :

- A tracking detector consisting of separate central ($15^\circ < \theta < 165^\circ$) and forward ($7^\circ < \theta < 25^\circ$) components together with a backward MWPC in the electron direction.
- A calorimeter system consisting of the main electromagnetic and hadronic LAr calorimeters, supplemented by a backward electromagnetic calorimeter (BEMC) in the electron direction, a plug calorimeter to detect small angle hadronic energy in the very forward direction, and limited streamer tubes (LST) in the iron return yoke to measure hadronic energy that has leaked out of the main calorimeter system.

HERA Experiment H1

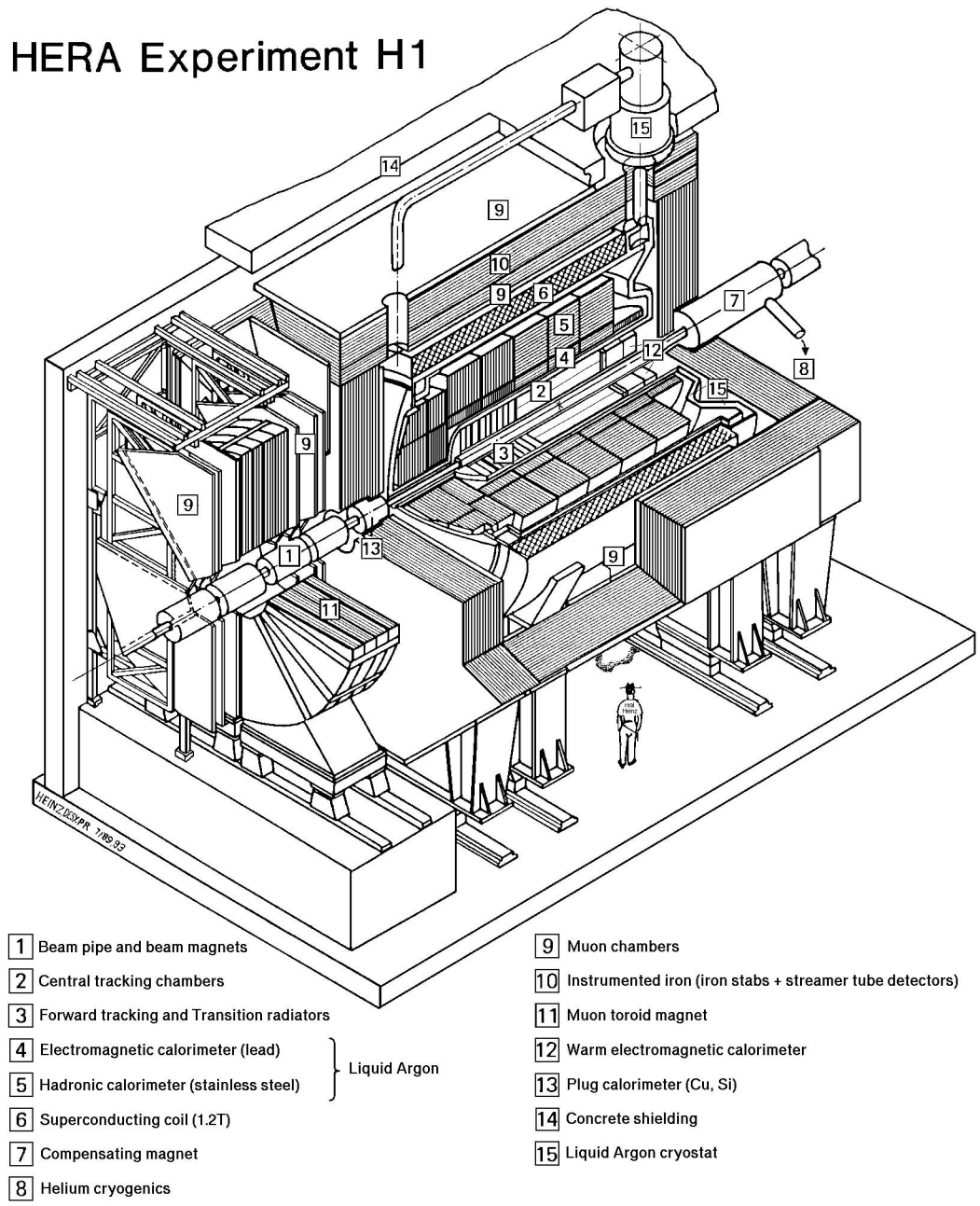


Figure 3.2: The H1 detector (3D view).

- A superconducting coil and cryostat outside the hadronic calorimeter in order to provide a magnetic field of approximately 1.15 Tesla over the central region.
- A set of iron plates surrounding the superconducting coil to act as a return yoke for the magnetic field. The return yoke is instrumented both to act as a tail-catcher for hadronic energy and also to provide muon identification and tracking.
- A forward muon spectrometer to supplement the muon identification in the forward region.
- A luminosity monitoring system consisting of small angle electron and photon detectors in the electron direction. The small angle electron tagger is also used as a trigger for low- Q^2 physics.

The above components will be discussed in more detail in the following sections, with particular emphasis on those components of relevance to the analysis presented in this thesis. A more detailed description of the H1 detector can be found in [47].

3.3 The H1 Tracking Detectors

Due to the typical event topology at HERA, the tracking system is divided into two main components, the Central Tracking Detector (CTD), covering the angular range $15^\circ < \theta < 165^\circ$, and the Forward Tracking Detector (FTD), covering the angular range $7^\circ < \theta < 25^\circ$. The H1 tracking system is then completed by a backward multiwire proportional chamber (BPC) in front of the backward electromagnetic calorimeter. The BPC covers the angular range $155.5^\circ < \theta < 174.5^\circ$. A side view of the H1 tracking system is shown in figure 3.3. A superconducting coil provides a uniform magnetic field inside the tracking region of approximately 1.15 Tesla parallel to the beam direction.

Both the central and forward tracking detectors consist of a series of drift chambers and multiwire proportional chambers (MWPC). The drift chambers are designed to give accurate measurement of the trajectory of charged particles, enabling

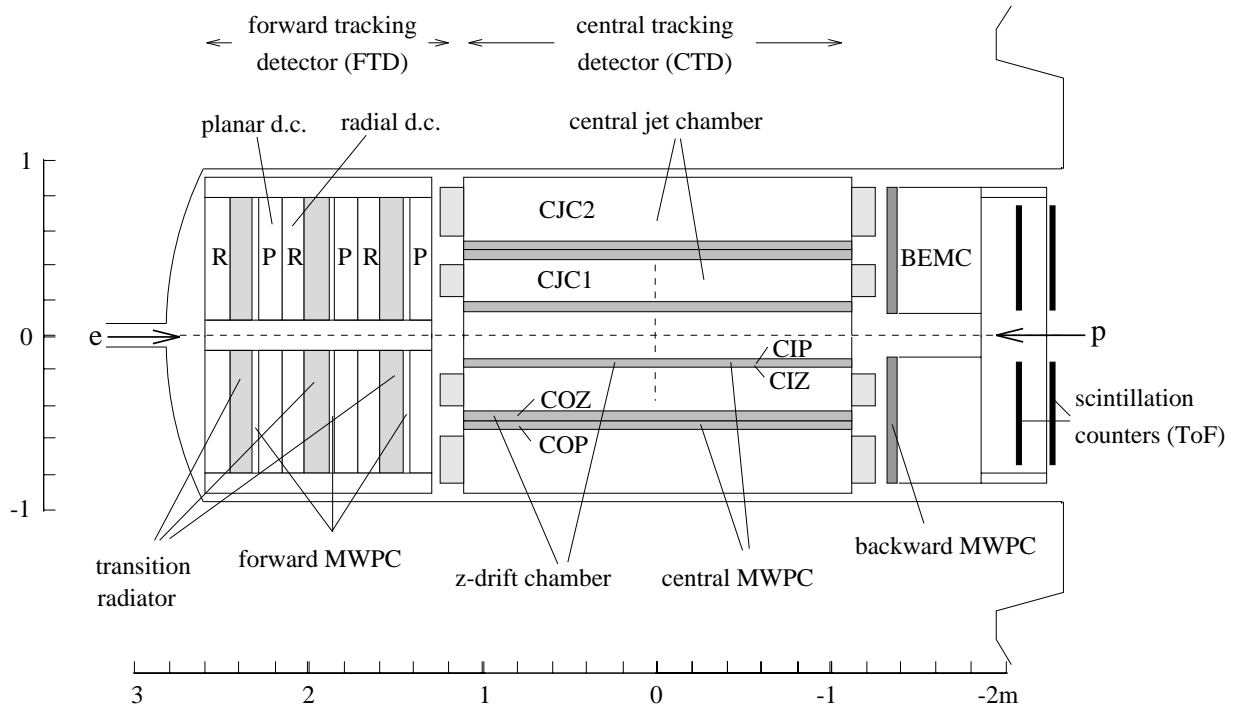


Figure 3.3: Side view of the H1 tracking detectors.

a determination of the particle momentum. This is achieved by a system of anode (sense) and cathode wires, which are used to set up a uniform drift field within the chamber, with the exception of the region very close (<1 mm) to the sense wires where the field increases very rapidly. A charged particle transversing the chamber causes ionization along its path. The resulting electrons drift towards the sense wires and in the region of increasing electric field an avalanche of electrons is produced. This causes a detectable signal on the sense wires. Readout and timing at the ends of the wires enables the trajectory of the charged particle to be accurately reconstructed.

The multiwire proportional chambers are used in event triggering. The proportional chambers are made up of finely spaced wires, such that a charged particle experiences a very high initial electric field, independent of the particle's trajectory. The resulting pulses are detected very quickly and enable a fast determination of the

approximate trajectory of the charged particle. This enables a fast trigger decision to be made. The spatial resolution of the MWPCs are limited by the spacing of the sense wires.

3.3.1 The Central Tracking Detectors

The functions of accurate $r\phi$ - and z -measurement are separated in the central tracking detector. Accurate $r\phi$ -measurement is provided by the Central Jet Chamber (CJC) [48] of which there are two rings. The CJC also provides moderate z -measurement by charge division; however precise z -measurement is instead provided by z -drift chambers both inside and outside the CJC. Finally two sets of multiwire proportional chambers provide a central track trigger [49]. Starting from the interaction region a charged particle is detected in the Central Tracking Detector by the inner MWPCs (CIP), the inner z -chamber (CIZ), the inner jet chamber (CJC1), the outer z -chamber (COZ), the outer MWPCs (COP) and finally the outer jet chamber (CJC2).

The Central Jet Chambers are JADE type jet chambers, with cells tilted by approximately 30° with respect to the radial direction and wires running parallel to the beam axis (see figure 3.4). The chamber has an inner radius of 200 mm, an outer radius of 795 mm and a length of 2640 mm centred about the nominal interaction point. A spatial resolution of $\sigma_{r\phi} \simeq 350 \mu\text{m}$ and $\sigma_z \simeq 5\text{cm}$ has been achieved [47], which compares well with the design goals.

The inner and outer z -chambers are drift chambers with wires stretched in a polygon around a cylinder. They consist of 16 azimuthal sectors and 60 cells in the z -direction. Using this arrangement a z -resolution of $\sigma \simeq 300 \mu\text{m}$ has been achieved [47]. The inner and outer z chambers are combined in a package with the inner and outer MWPCs respectively. The inner z -chambers and inner MWPCs are designed to fit into a cylinder with an inner radius of 15 cm, an outer radius of 20 cm and a total length of 249 cm. The outer z -chambers and the outer MWPCs lie between the two CJC chambers, with an inner radius of 45.5 cm and an outer radius of 49 cm.

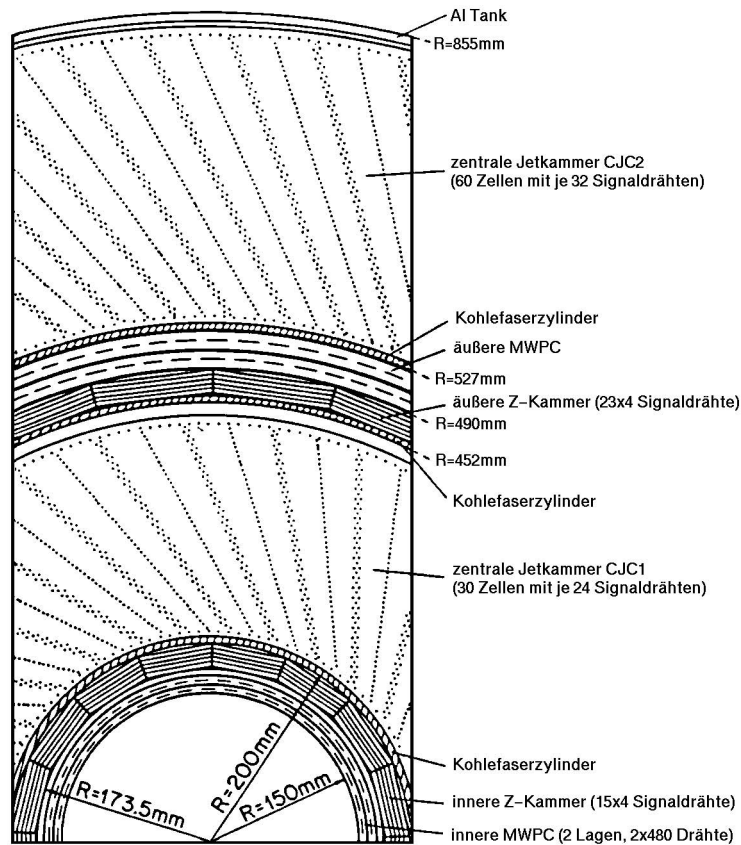


Figure 3.4: Cell structure of the Central Jet Chamber

3.3.2 The Forward Tracking Detectors

The H1 Forward Tracking Detector (FTD) [50] consists of three identical sub-units, known as supermodules, numbered from 0 to 2 in increasing z . Each supermodule, when seen from the direction of the incoming proton, consists of a planar chamber module, followed by a MWPC, then a layer of transition radiator material, and finally a radial drift chamber. The FTD covers the angular range between 7° and 25° with a sensitive region of $134 < z < 254$ cm and $15 < R < 79$ cm. The orientation of the chambers is designed to maximise the number of sense wires passed by a particle and so increase the number of hits per track. The layout of the H1 forward tracker is illustrated in figure 3.5

Each planar chamber module consists of three planar drift chambers orientated

Figure 3.5: Side view of the H1 Forward Tracker.

at 0° , $+60^\circ$ and -60° to the vertical respectively. Each chamber consists of four wire planes in the z direction. The sense wires in each drift chamber are only read out at one end of the wires, and hence no information is available concerning the coordinate of each hit along the wires. However the separate orientations enable the trajectory of a particle passing through the tracker to be reconstructed. The structure of the planar drift chambers is illustrated in figure 3.6. The methods used to reconstruct a track in the planar chambers will be discussed in more detail in chapter 5.

The radial drift chambers consist of planes of sense wires radiating out from the beam-pipe, such that the maximum drift length for each wire increases with increasing distance from the beam pipe. This enables an accurate measurement of the azimuthal angle, together with a moderate measurement of the radial coordinate using charge division. The radial chambers are also used to detect the X-rays from the transition radiators. Each radial chamber has 48 cells in ϕ equipped with 12 sense wires stacked in z . The layout of the radial drift chambers is illustrated in figure 3.7

Figure 3.6: The Planar Drift Chambers.

A more detailed description of the forward tracker and the reconstruction of tracks in this region is given in chapter 5.

3.3.3 The Backward MWPC

The H1 tracking system is completed by a multi-wire proportional chamber situated in front of the backward electromagnetic calorimeter. This consists of four planes of parallel wires, each rotated by 45° with respect to each other. The backward MWPC completes the trigger system for the tracking detector and also provides additional space points for small angle tracks pointing towards the backward electromagnetic calorimeter in order to improve the identification and measurement of electrons for low- Q^2 DIS events.

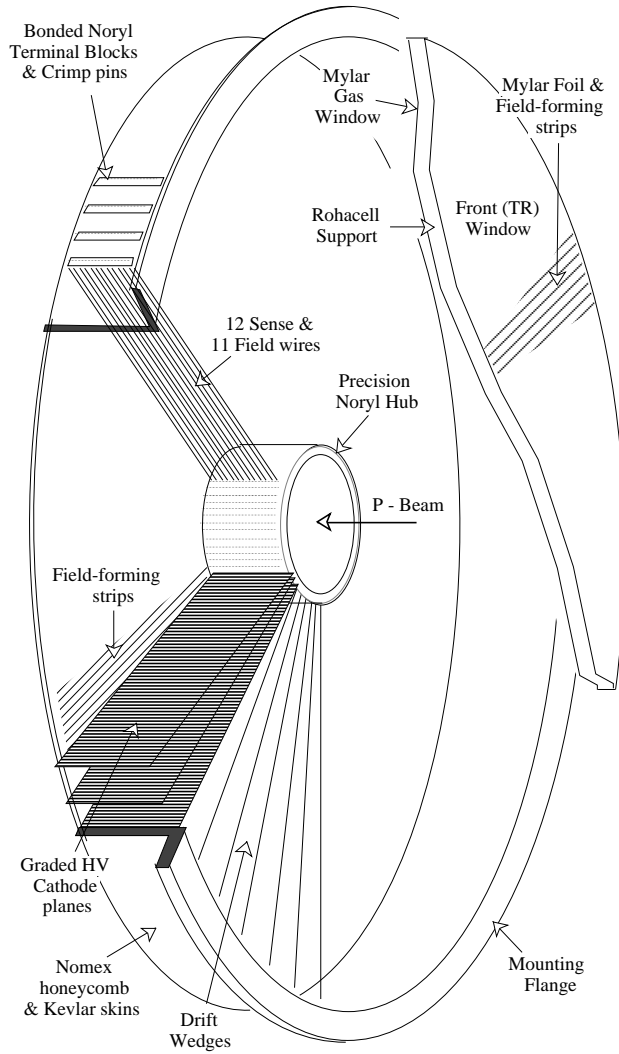


Figure 3.7: The Radial Drift Chambers.

3.4 The H1 Calorimeters

The H1 tracking system is complemented by the H1 calorimeter system which is designed to measure the total energy of both charged and neutral particles produced in the interaction. The calorimeter system consists of the main Liquid Argon Calorimeter (LAR) covering the angular range $4^\circ < \theta < 153^\circ$, the Backward Electromagnetic Calorimeter (BEMC) covering the angular range $151^\circ < \theta < 177^\circ$, the Plug Calorimeter in the very forward direction ($0.3^\circ < \theta < 3^\circ$) and the Tail Catcher (TC) covering the angular range $6^\circ < \theta < 172^\circ$.

The H1 calorimeters are all based on the same principle of layers of passive absorption material interleaved with layers of instrumented active regions. A particle passing through the absorption material produces a shower of particles. The shower particles produced lose energy by ionisation or excitation of the active medium. By measuring the ionisation produced in the active regions the development of the shower can be periodically sampled. Consequently, the total energy of the incident particle can be measured and the longitudinal and transverse profile of the shower can be determined.

In electromagnetic calorimeters, energetic photons and electrons produce a shower of lower energy photons and electrons due to Bremsstrahlung and pair production processes. The development of an electromagnetic shower in a given absorption material is characterised by the radiation length, X_0 , the mean longitudinal length over which an electron loses all but $1/e$ of its energy.

A strongly interacting particle passing through an absorption material loses energy through inelastic nuclear collisions producing lower energy hadrons which undergo further inelastic collisions. Hadronic showers take longer to develop than electromagnetic showers, and for any given absorption material the longitudinal development of the hadronic shower is given by the nuclear interaction or absorption length, λ .

The LAr calorimeter [51] consists of an electromagnetic section with lead absorbers, corresponding to a depth of between 20 and 30 radiation lengths, and a hadronic section with steel absorbers. The total depth of the LAr calorimeter varies between 4.5 and 8 hadronic interaction lengths. The containment of the LAr calorimeter is shown in figure 3.8 in terms of radiation lengths X_0 and absorption lengths λ for the electromagnetic and hadronic components respectively. The calorimeter is highly segmented in both sections, with a total of around 45000 cells. The root mean square electronic noise per channel typically corresponds to 10 to 30 MeV.

Test beam studies of LAr calorimeter modules have demonstrated energy resolutions of $\sigma(E)/E \simeq 0.12/\sqrt{E} \oplus 0.01$ with E in GeV for electrons [52] and $\sigma(E)/E \simeq$

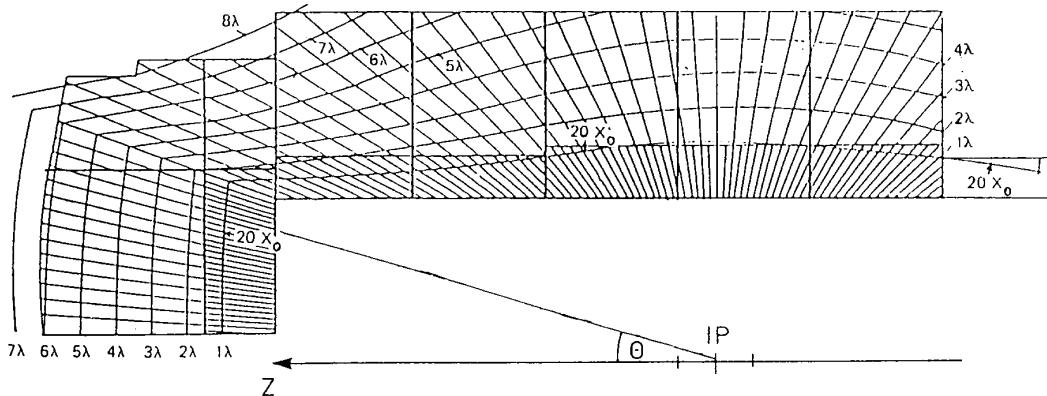


Figure 3.8: Containment of the LAr stacks: iso- λ and iso- X_0 lines

$0.5/\sqrt{E} \oplus 0.02$ for charged pions [47, 53]. The hadronic energy scale and resolution have been verified from the balance of transverse momentum between hadronic jets and the scattered electron in deep inelastic scattering events and are known to a precision of 5% and 10% respectively.

The containment of hadronic energy is completed by plastic streamer tubes interleaved with the iron plates in the return yoke, and by a small angle plug detector in the very forward direction. The plug calorimeter is a silicon-instrumented sandwich calorimeter and is designed to cut down on the missing component of the total transverse momentum due to the proton remnant.

Finally the H1 calorimeter system is completed by the backward electromagnetic calorimeter (BEMC) covering the angular range $151^\circ \leq \theta \leq 177^\circ$, with a thickness of 22.5 radiation lengths. This is designed to measure the energy of electrons scattered in the backward region, and to a lesser extent to measure hadronic energy flow in photoproduction events. The detector consists of 88 calorimeter stacks, each of which contains 50 lead-scintillator sandwich layers with readout by wavelength shifter bars (WLS) and photodiodes. Test beam studies have determined the energy resolution of the BEMC calorimeter for incident electrons to be $\sigma(E)/E \simeq 0.10/\sqrt{E} \oplus 0.01$ with E in GeV [47]. The segmentation of the BEMC calorimeter is shown in figure 3.9

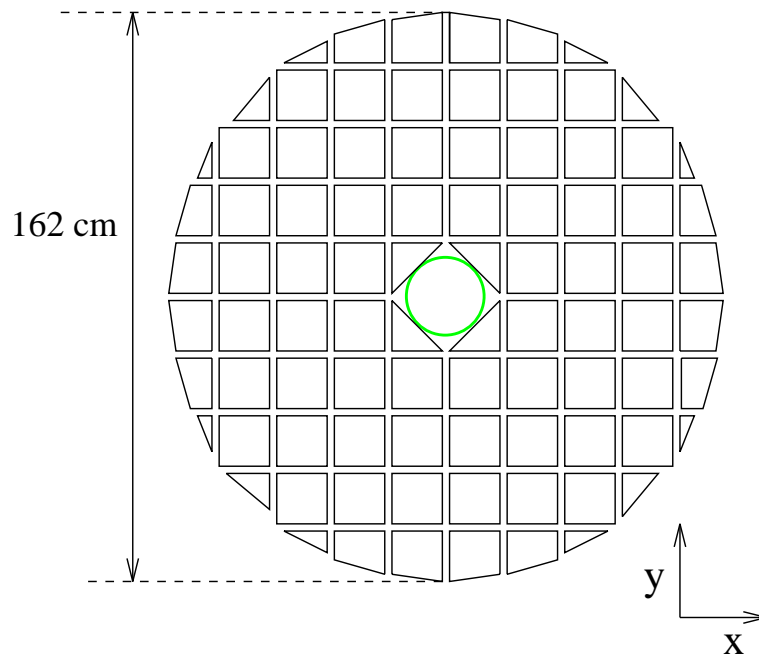


Figure 3.9: The Backward Electromagnetic Calorimeter (BEMC): x, y view.

3.5 Muon Detection

Muon identification is provided in the H1 detector by streamer tube chambers in the instrumented iron return yoke. However in the forward direction this is inadequate for the measurement of muon momenta and so this is supplemented by a separate forward muon spectrometer. This consists of four sets of drift chambers designed to measure the polar angle, θ , and two sets of drift chambers designed to measure the azimuthal angle ϕ . A magnetic field is provided by a toroidal magnet to facilitate the measurement of the track momentum.

3.6 Luminosity Monitoring

A fast luminosity measurement system is provided at the H1 detector by small angle electron and photon detectors in the electron direction. This makes use of the Bethe-Heitler process $ep \rightarrow e\gamma p$. This has a large and exactly calculable cross-

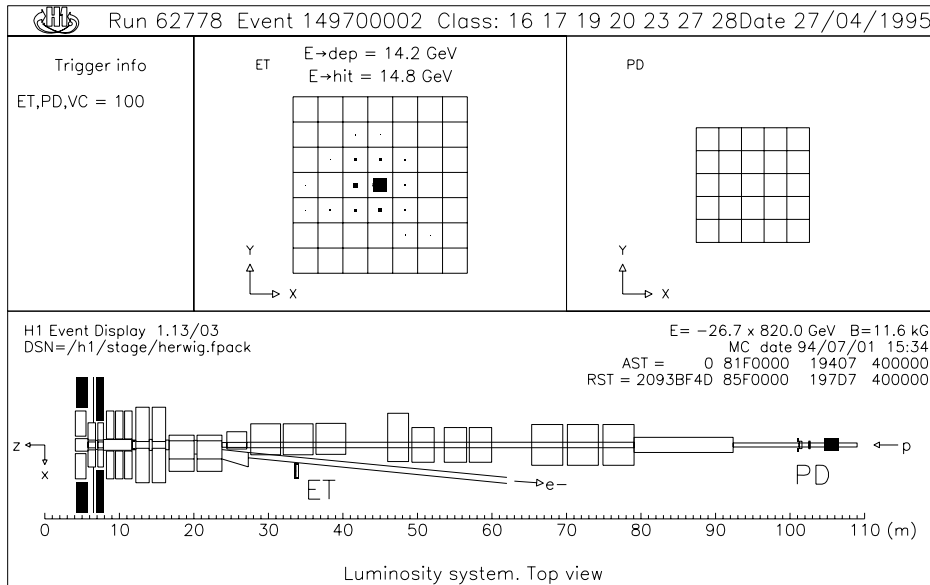


Figure 3.10: The H1 Luminosity System.

section, making it an ideal reaction to study in order to measure the luminosity. The electron and photon detectors are TlCl/TlBr crystal calorimeters, with a resolution of $\sigma(E)/E = 0.1/\sqrt{E}$ with E in GeV. The electron tagger is located at $z = -33$ m and the photon tagger at $z = -103$ m. The electron tagger accepts electrons with an energy fraction between 0.2 and 0.8 with respect to the beam energy and scattering angles below $\theta' \leq 5$ mrad ($\theta' = \pi - \theta$). The layout of the H1 luminosity system is shown in figure 3.10.

The electron tagger detector is also used as a trigger for photoproduction interactions, in which case it is combined with a veto against there being a photon in the small angle photon detector. However, due to the fact that the small angle photon detector is not 100% efficient and due to the high cross-section for Bremsstrahlung reactions, the above trigger must be combined with triggers from other detectors to study photoproduction reactions.

3.7 Scintillation Counters

Fast scintillation detectors at H1 enable genuine ep interactions to be distinguished from proton induced background interactions occurring upstream of the detector. The scintillation detectors work on the principle that particles produced from ep interactions will arrive at a different time from background interactions relative to the nominal time of the bunch crossing. Background events produced near the interaction cannot be distinguished from ep interactions in this way, however the scintillation counters give a significant reduction in the background rate.

Two scintillation detectors exist at H1. The Time of Flight system (ToF) consists of two planes of scintillator situated between the BEMC and the backward iron endcap. The inner and outer veto walls are situated further upstream at $z = -6.5\text{m}$ and $z = -8.1\text{m}$ respectively.

3.8 Triggering and Off-line Analysis

Interactions at the H1 detector are dominated by background events rather than the physics events of interest. Consequently, sophisticated triggers are required to reject background events, whilst at the same time keeping the physics events of interest. Background events that have to be considered include

- low energy photons or electrons from synchrotron radiation;
- interactions between beam protons or electrons with the residual gas in the chamber;
- interactions between off momentum beam particles and the wall of the vacuum chamber;

and

- cosmic rays.

The combined background rate at H1 is $\approx 10\text{kHz}$. This must be compared with the rate of the dominant physics process (photoproduction), at the design luminosity, of $\approx 100\text{Hz}$.

The triggering is complicated by the short beam crossing time at HERA of 96 ns. Consequently the readout and trigger system is ‘pipelined’, with the information from the last 24 bunch crossings being stored whilst an initial trigger decision (L1) is determined. During this period, only simple reconstruction tasks in each detector component can be made before the resulting trigger elements are sent to the central trigger logic. If there is any combination of trigger elements that would indicate a true interaction then a signal is sent to each subdetector and the event is read out. During the time it takes to read out the event, the detector cannot read out any further events. The trigger system is pipelined in order to minimise this ‘dead-time’

Once the information from an event has been read out, the event is sent to the level 4 (L4) trigger. The L4 trigger system, often referred to as the L4 Filter Farm, operates independently of the L1 trigger, enabling data taking to continue. The L4 Filter Farm performs a partial event reconstruction in order to make a more sophisticated decision as to whether the event is accepted or not. The accepted events are stored on cartridge and a full event reconstruction is then performed using the event reconstruction program HIREC [54]. Typically events are reconstructed a few hours after the event was recorded. At this stage, L5, a final selection is performed to select events of interest to the physics working groups with each event being assigned a set of ‘class numbers’ which can then be used to select relevant events for subsequent physics analysis.

The resulting events are analysed within the framework of the H1 analysis package, H1PHAN [55]. This stores the information in the event into ‘Q-vectors’ and enables this information to be accessed via simple FORTRAN statements. The analysis package also provides several standard analysis routines such as jet finding algorithms and routines to reconstruct the event kinematics.

Monte Carlo events are used both to study detector acceptances and also to compare with the data. The events are produced by several different event generators

tuned to the physics of interest. The output from the event generators is then passed through the detector simulation program H1SIM [56], and is then passed through the same analysis chain as the data.

Chapter 4

Event Selection

4.1 Introduction

In the remainder of this thesis, an analysis of hard photoproduction at H1 is presented. To allow a direct comparison between the selected data sample and predictions from leading order (LO) Monte Carlo generators, several methods have been used to select events with a hard scattering.

In this section, the basic tagged event selection is described. This is the basis for all subsequent event samples in the following analysis. The background contamination after the full event selection is estimated using the measured fractional energy spectrum of the photon determined from the scattered electron reconstructed in the small angle electron tagger. The track selection used throughout this thesis is outlined. Finally the Monte Carlo generators used to compare with the data and to study the acceptance of the detector are described in detail.

4.2 The Tagged Event Selection

Tagged events are triggered by requiring an electron candidate with an energy $E_{e'} > 4$ GeV in the electron tagger and less than 2 GeV deposited in the small angle photon detector. Due to the high rate of background events triggered by a pure electron tagger trigger, in addition to the presence of the tagged electron a trigger from the

central detector components is required in order to ensure the presence of activity in the central region of the detector.

In the subsequent analysis two trigger conditions were considered. Firstly, in order to obtain an unbiased event selection for the analysis of the inclusive charged particle cross section, a sample of events triggered by a coincidence between a tagged electron and a ray from the central and forward multiwire proportional chambers was selected (Sample I). Due to the high rate, this trigger (referred to as Etag*t0) was downscaled during the 1993 run period. The sample of events selected by this trigger is referred to as the ‘minimum bias’ tagged event sample. Secondly, in order to study jet production, and the energy flow and charged particle multiplicity in hard photoproduction, a sample of events triggered by a coincidence between a tagged electron and a track from the central jet chamber trigger was selected (Sample II).

In addition to the above trigger requirements, the L4 selection algorithm rejected events that were positively identified as beam-gas background, beam-wall background, cosmics or trigger noise. In particular, beam gas events were rejected using their characteristic energy flow by rejecting events with

$$R_{beamgas} = (y_{JB})^2 + ((1 - \sum p_z / \sum p) / 0.3)^2 < 1$$

Here $y_{JB} = \sum(E - p_z) / (2E_e)$ is measured after a partial event reconstruction, where $\sum(E - p_z)$ is determined by summing $E \cdot (1 - \cos\theta)$ over all tracks and isolated calorimeter cells and p_z denotes the longitudinal momentum component. This closely follows the event selection described in [26] and [73]. In addition, events with no activity in either the central or forward trackers after a partial track reconstruction were also rejected.

The initial event samples consisted of 132311(325533) events from a total integrated luminosity of 117.0 (312) nb⁻¹ respectively. All events were selected from runs in which the essential components of the detector, such as the LAr calorimeter and the central tracking detectors, were stable. The resulting sample was determined [58] to have a background contamination of $0.49 \pm 0.06\%$ ($0.86 \pm 0.07\%$) due to electron induced background and $5.8 \pm 1.0\%$ ($9.5 \pm 1.5\%$) due to proton induced background

for sample I(II) respectively. For the analysis of the charged particle production in the forward region the forward tracker was also required to be operational.

The dominant remaining background consists of interactions between the proton beam and the residual gas in the fiducial central region appearing in random coincidence with a signal in the electron tagger. The background contamination was further reduced by applying a cut on the fractional energy of the photon, y , which in the case of electron tagged events is well approximated by $y_{TAG} \simeq 1 - (E_{e'}/E_e)$. Here E_e and $E_{e'}$ are the energy of the incoming and scattered electron respectively. In order to ensure a reliable reconstruction of the tagged electron a fiducial cut of $|x_{TAG}| < 6.5$ cm was applied, where x_{TAG} is the reconstructed x coordinate of the tagged electron. The measured distributions of the fractional energy of the photon, determined from the reconstructed tagged electron, for sample I and a background event sample selected by a pure electron tagger monitor trigger are shown in figures 4.1a and 4.1b respectively. To estimate the background contamination in the final data sample, the monitor trigger distribution was normalised to the data using that part of the spectrum below $y_{TAG} < 0.2$. Figure 4.1c shows the measured distribution for sample I compared with the renormalised background distribution. A cut of $0.3 < y_{TAG} < 0.7$ was applied to the data sample giving an estimated upper limit to the background contamination of $(3.0 \pm 0.5)\%$ and $(2.8 \pm 0.5)\%$ for samples I and II respectively.

Finally, for the remaining events, a cut was performed on the z coordinate of the reconstructed vertex, $ZVTX$. To restrict the analysis to a region of homogeneous track acceptance a cut of $-25 < ZVTX < +25$ cm was applied. This also reduces the remaining background contamination, as illustrated in figure 4.2 in which the $ZVTX$ distribution for a sample of 897 proton pilot bunch events is shown. Events in which a vertex has not been reconstructed have been excluded from the distribution, accounting for 2% of the pilot bunch sample. The $ZVTX$ cut rejects 40% of the proton pilot bunch events, whilst only rejecting approximately 3% of the data sample. After such a cut, the remaining background contamination has been estimated at less than 2% for both samples and is ignored in the subsequent analysis.

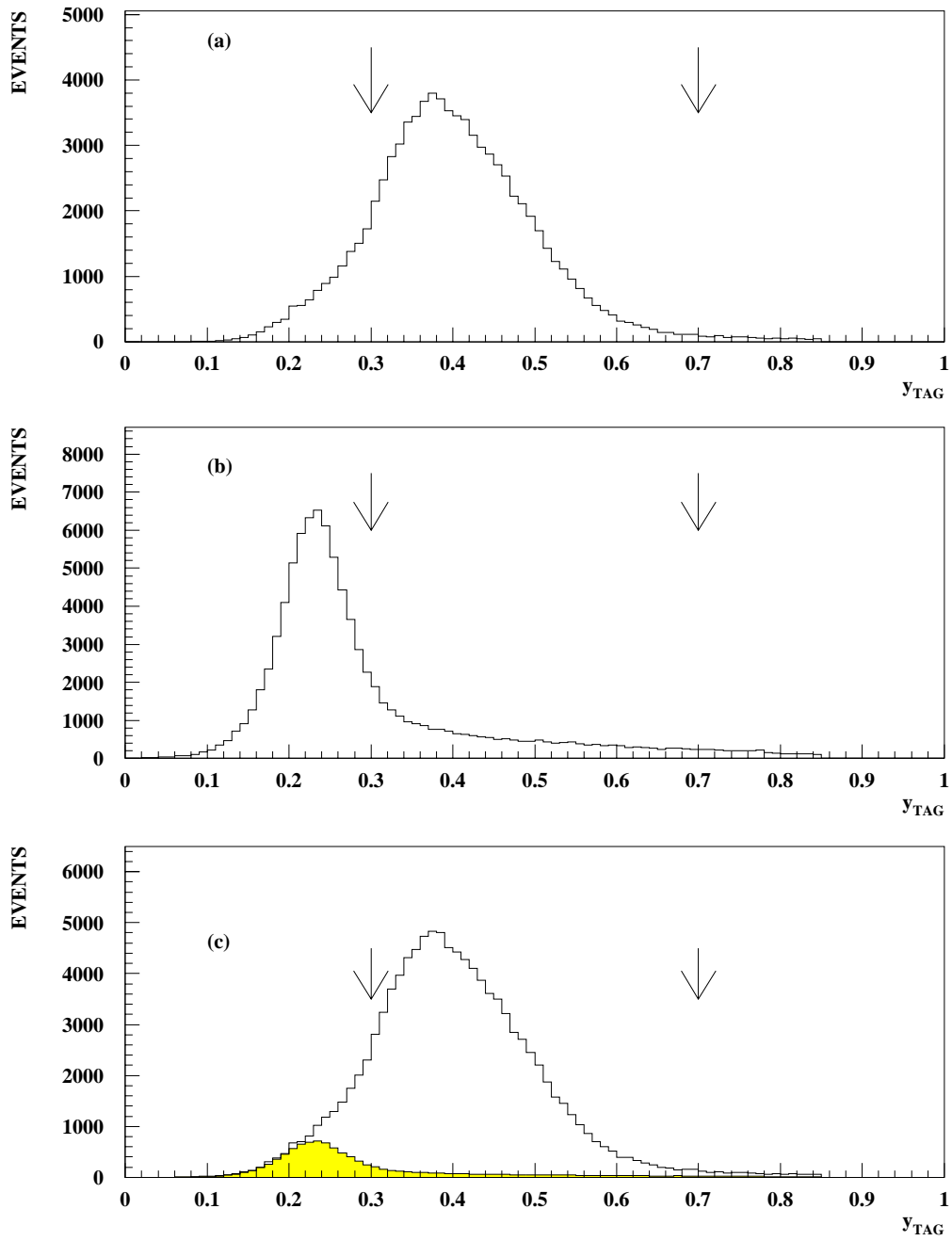


Figure 4.1: The y_{TAG} distribution for (a) sample I, (b) the background sample and (c) sample I compared with the background sample normalised to the number of events with $y_{TAG} < 0.2$. The arrows indicate the cut applied in the final data sample

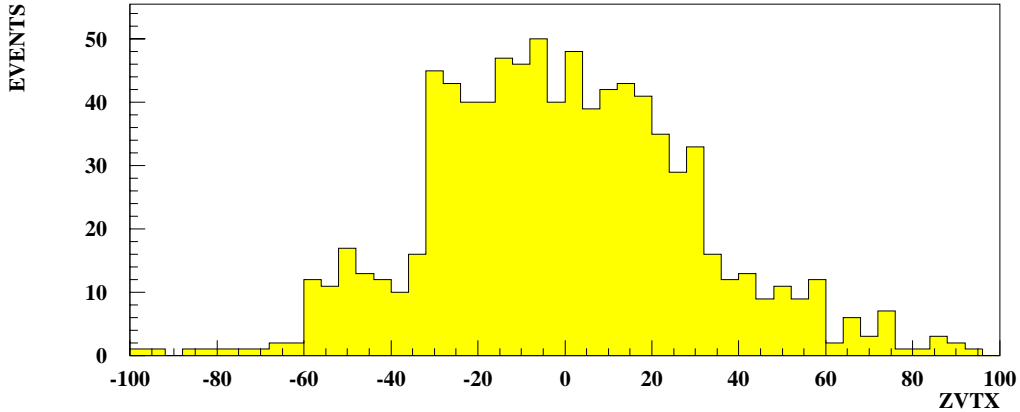


Figure 4.2: The measured ZVTX distribution for a sample of 897 proton pilot bunch events.

The ZVTX distribution is compared between data and Monte Carlo in figure 4.3. The results of a gaussian fit to the data is illustrated by the dashed line. The distributions for data and Monte Carlo agree very well in the central region. However the data shows broader tails to the distribution due to the presence of beam induced backgrounds (see above). Furthermore a small second peak can be seen in the data at $z \approx 60\text{cm}$ due to satellite bunches.

The measured distribution of the fractional energy of the quasi-real photon, y_{TAG} , as determined from the reconstructed scattered electron is shown in figure 4.4 compared with the expected distribution from a Monte Carlo simulation. The background contribution (see above) has been statistically subtracted from the data. The distributions are similar in shape, however the Monte Carlo shows a small shift compared with the data. This is due to uncertainties in the calculation of the photon flux in the Monte Carlo generator.

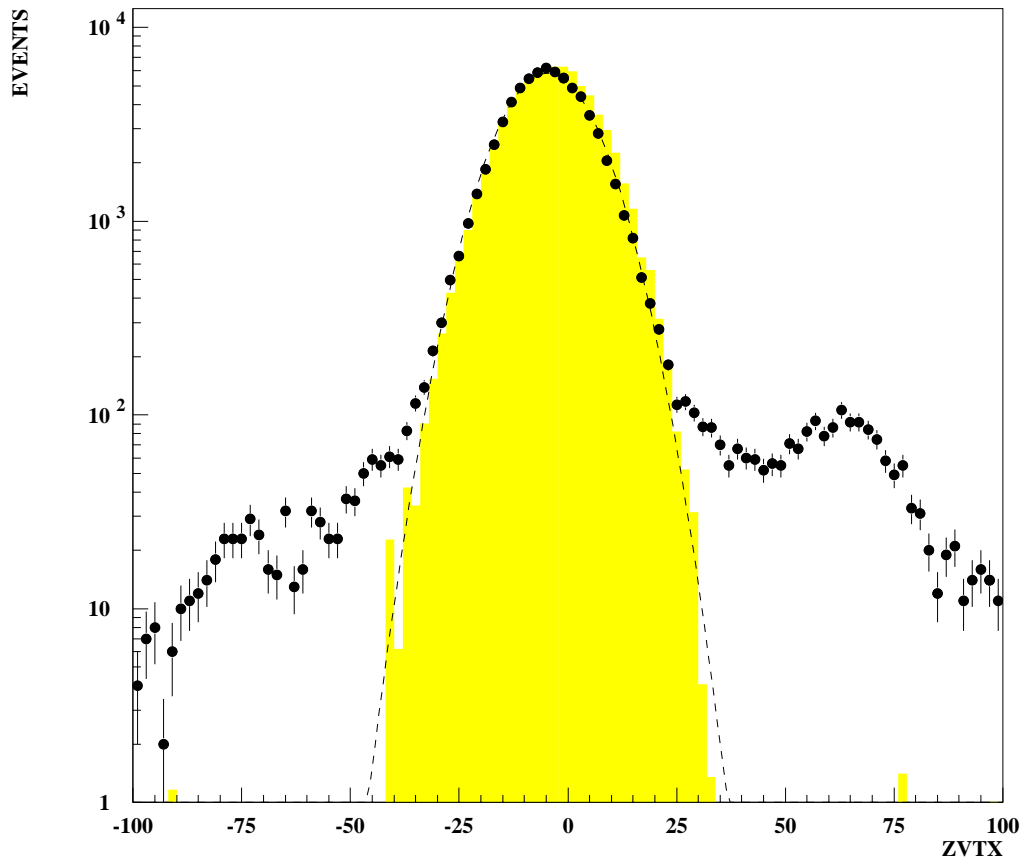


Figure 4.3: The measured ZVTX distribution for data (points) and Monte Carlo (histogram) respectively. The dashed curve illustrates the result of a gaussian fit to the data.

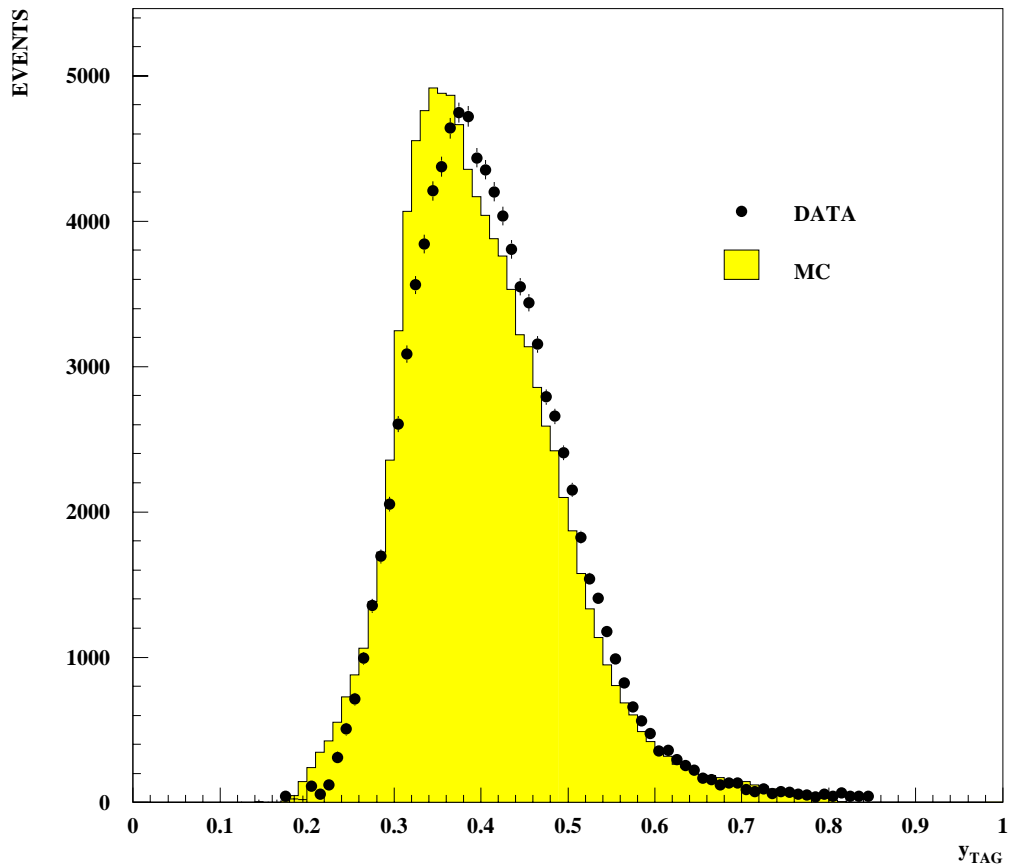


Figure 4.4: The measured y_{TAG} spectrum for data (points) and Monte Carlo (histogram) respectively.

4.3 Good Track Selection

In the remainder of this thesis, ‘good’ tracks are defined as vertex constrained tracks measured in either the central or forward tracking detectors which for tracks reconstructed in the central tracker have

- $15^\circ < \theta < 155^\circ$;
- at least 10 hits in the central jet chamber;
- a radius at the start of the track < 30 cm;
- $|DCA| < 2.0$ cm, where DCA is the distance of closest approach between the extrapolated track and the primary vertex;
- $|Z_0| < 50$ cm, where Z_0 is the z-value of the track at the point of closest approach;
- $p_T > 0.3$ GeV;
- $\Delta p/p < 0.3$;

and for tracks reconstructed in the forward tracker have

- at least 2 planar segments;
- $5^\circ < \theta < 30^\circ$;
- $|DCA| < 2.0$ cm;
- $|Z_0 - Z_{vtx}| < 10$ cm;
- $p_T > 0.3$ GeV;
- $\Delta p/p < 1.0$;

The determination of the track selection criteria for tracks measured in the forward tracker is discussed in section 5.

4.4 MC Samples

In the following analysis, comparisons have been made with three different event generators. A detailed detector simulation has then been performed and the resulting event samples passed through the same analysis chain as the data. The event generators considered are described below. In all cases the GRV-LO leading order parton density parameterisations for the proton and photon were used.

4.4.1 PYTHIA

The PYTHIA event generator [59] is based on leading order QCD matrix element calculations, including parton shower models for the initial and final state parton radiation. The PYTHIA event generator has been used to generate photon-proton interactions, the electron vertex being treated by a generator for quasi-real photons.

The strong coupling constant α_s was calculated in first order QCD using $\Lambda_{QCD}=200$ MeV with 4 flavours. The renormalisation and factorisation scales were both set to the transverse momentum, p_T , of the outgoing partons from the hard scattering. To avoid the divergence in the matrix element, a lower cut-off has been applied to the transverse momenta of the partons emerging from the hard interaction of $p_T \geq 2.0$ GeV.

Separate event samples corresponding to resolved, direct(light quarks) and direct(heavy quarks) processes have been produced. Optionally, PYTHIA allows for additional interactions between partons from the proton remnant and partons from the photon remnant within the ‘multiple interaction model’. The same parameters as used in previous studies of multiple interactions in $p\bar{p}$ collisions have been used [60, 61, 62]. Multiple interactions are treated within the framework of LO QCD with a lower cut-off for the transverse momentum of the partons emerging from the multiple interaction process of $p_T \geq 1.2$ GeV. The hadronisation process has been treated using the Lund fragmentation scheme as implemented in JETSET[63]

4.4.2 HERWIG

The HERWIG event generator [64] is also based on LO QCD calculations. It includes a parton shower model which allows for interference effects between initial and final state showers (colour coherence) [65]. As above the renormalisation and factorisation scales were both set to the the transverse momentum, p_T , of the outgoing partons from the hard scattering. The strong coupling constant α_s was calculated in first order QCD using $\Lambda_{QCD}=180$ MeV with 5 flavours.

HERWIG also, optionally, allows for additional interactions of the beam remnants in terms of a ‘soft underlying event’, modelled as soft hadron-hadron collisions. A cluster model is used to treat the hadronisation process.

4.4.3 PHOJET

The PHOJET generator[66] attempts to describe both soft and hard photoproduction in a consistent approach. The generator is based on the two-component Dual Parton Model (DPM) [67]. The realisation of the generator is similar to the Monte Carlo event generator DTUJET [68] simulating multiparticle production in hadron collisions up to high energies.

Hard processes are calculated in LO pQCD with a lower transverse momentum cutoff of $p_T \geq 3\text{GeV}$. Soft interactions are represented mainly by strings stretched between valence quark and di-quark and between quark and diquark of the colliding proton and resolved hadronic state of the photon.

Multiple interactions are a characteristic feature of the PHOJET generator. The multiplicities of soft and hard interactions are calculated within a unitarization scheme [69], with an average multiplicity in the energy range of HERA of approximately 1.7 interactions per event. The details of the calculation of the cross sections for different configurations of the final state are given in [70]. The Lund string model as implemented in JETSET is used for the description of the fragmentation process.

Chapter 5

The Performance of the H1 Forward Tracker

5.1 Introduction

An important consideration in the study of high E_T photoproduction and the determination of the presence of multiple interactions at HERA energies is the analysis of the production of charged particles using the H1 tracking detectors. The presence of multiple interactions manifests itself in the form of additional event energy, typically in the region of $\eta^*=0$, where η^* is the pseudo-rapidity in the γp rest frame. Typically, the γp rest frame is boosted by approximately two units of rapidity in the forward direction. Consequently in order to test any model including multiple interactions, it is necessary to use the H1 forward tracker. In this chapter an analysis into the performance of the H1 forward tracker is presented.

5.2 Track Reconstruction in the Forward Tracker

As described in chapter 3 the forward tracking detector (FTD) consists of three identical sub-units, known as supermodules. Each supermodule consists of a planar

drift chamber module, a MWPC module for triggering, a layer of transition radiator material, and finally a radial drift chamber module. A planar drift chamber module consists of twelve planes of wires perpendicular to the z axis. The first four planes have wires which are aligned vertically, the next four at $+60^\circ$, and the final four at -60° to the vertical. The three sets of planes are referred to as ‘orientations’. The radial chambers consist of 12 radial planes of wires with each plane divided into 48 wedges.

The pattern recognition for the FTD is described in detail in [50]. Initially line segments are independently reconstructed in the planar and radial chambers. These are then combined to form a track. The procedure adopted when reconstructing line segments in the planar and radial chambers differs due their respective geometries.

5.2.1 Planar Segment Pattern Recognition

A charged track passing through a planar chamber module will deposit charge which will be measured as hits on the wires. The wires are only read out at one end and so there is no knowledge of the position of a hit along the direction of the wire. To a good approximation the path of a track through a chamber is straight and hence the information from the drift distances to the sense wires can be expressed as a plane. Within the tolerance of the detector, the three planes from each orientation intersect to form the track.

There are two stages to the planar pattern recognition. Firstly, digitisations within an orientation are combined into a ‘cluster’. Due to the drift sign ambiguity, ionisation left by a particle gives two possible hit positions and so both have to be treated as a real hit. Each hit on the first wire plane in z is paired with every hit on the last wire plane. Clusters are only formed when at least one hit is found in the two intermediate wire planes within four standard deviations of a straight line extrapolation between the first and last hit.

Hits can contribute to more than one cluster and therefore the set of clusters obtained must then be reduced until a subset of clusters is found that do not share digitisations. The two hits due to the drift sign ambiguity are considered as one digi-

tisation for the rejection procedure. The method used in this reduction is described in detail in [50].

In the second stage of the planar pattern recognition, a cluster from each of the orientations are combined to form planar segments. The intersections between all possible pairs of cluster planes are calculated. For a true planar segment, the three resulting intersections will agree within the tolerance of the detector. Consequently any three intersections which lie within a given distance of each other at the front and rear face of the chamber, currently 7 mm, are candidates for a line segment. However, many of the resulting line segments will share clusters and therefore the initial set of segments must be reduced to form a disconnected subset. The procedure used at this stage is more elegant than the method used in the above cluster reduction. This is possible since the smaller number of segments enables the algorithm used to be more computationally intensive.

5.2.2 Radial Segment Pattern Recognition

There are two stages to the radial pattern recognition, which is performed individually for each wedge. The first stage is to reconstruct triplets of adjacent points within a wedge. A triplet is defined as three adjacent hits satisfying the following criterion

$$\left| \frac{1}{2}(d_1 + d_3) - d_2 \right| < P_1 \quad (5.1)$$

where d_1, d_2, d_3 are signed distances to the wire plane and P_1 is a parameter, currently 1 mm.

In the next stage of the pattern recognition, line segments are produced by joining triplets which have shared hits with the same drift sign and for which the resulting group of hits lies, within the tolerance of the chamber, on a straight line extrapolation between the first and last digitisation. Triplets separated by one missing hit may also be combined if they satisfy the straight line constraint. A straight line fit to the combined triplets is used to extrapolate along the wedge and pick up isolated digitisations. Only the line segment with the largest number of hits is then retained and the remaining segments rejected. If more than one track

satisfies this criterion, the segment with the best χ^2 fit to a straight line is retained. This is repeated until insufficient digitisations remain and at which point the next wedge is considered.

The above procedure finds hits belonging to a track segment provided that the track segment lies entirely within one radial wedge. In general this may not be true, however line segments can be extrapolated in ϕ into nearby wedges to pick up associated digitisations.

5.2.3 Line Segment Linking and Track Fitting

The final stage in the reconstruction of tracks in the forward tracker is to link individual line segments to form tracks and to determine the track parameters.

The line segments forming a track lie on a helix. However, due to limitations in computing time, it is not possible to use a helix fit to link segments. Instead, an approximate track model is used to link segments and check whether the resulting track is consistent with a helix. The details of the approximate track model are described in [50].

There are four stages to the segment linking. Firstly, planar line segments are linked to form candidate tracks. The resulting two and three-module tracks are extrapolated in order to attempt to link radial segments. Secondly, and independently, radial line segments are combined to form candidate tracks which are then extrapolated to attempt to link any planar segments. However, due to chamber inefficiencies and the two track resolution, neither procedure can be used to select all possible tracks. Consequently, in the third step, the two sets of tracks are compared and a unique set of two and three-module tracks is selected. The selection procedure depends on the efficiency of the hardware. At present, planar based tracks are favoured over radial based tracks, and a radial based track is only retained if it is verified by at least one planar segment.

After this procedure, there remains unassociated single planar and radial segments. The remaining planar segments are fitted to straight lines in $\phi - z$ and $R - z$ and these lines are extrapolated into the radial chambers in order to try and

associate them with remaining radial segments. In this final step somewhat larger tolerances are applied.

Finally following the linking of individual line segments to form a track a Kalman filtering technique is used to determine the optimum track parameters.

5.3 Determination of the Track Reconstruction Efficiency

The efficiency of the forward tracker has been determined using the results of a detailed Monte Carlo simulation. This has been achieved by relating simulated and reconstructed tracks using the ratios R1 and R2 given by

$$R1 = \frac{N_C}{N_R} \quad \text{and} \quad R2 = \frac{N_C}{N_S} \quad (5.2)$$

where N_S, N_R are the number of simulated and reconstructed hits of the tracks under consideration and N_C is the number of hits shared by both the simulated and reconstructed track. Only hits in the planar chambers of the forward tracker were considered.

The ratios R1 and R2 are calculated for every possible pair of a simulated and a reconstructed track. The track pair with the highest values of R1 and R2 are matched and are no longer considered. This is repeated in an attempt to match further reconstructed and simulated tracks. In this way a unique correspondence between reconstructed and simulated tracks is produced.

In order to determine the efficiency, stable charged particles from the primary event vertex were considered. The reconstruction efficiency was defined as the ratio of the number of such particles that had a matched reconstructed track to the total number of such particles. It is also possible to determine the efficiency to reconstruct a planar segment within a supermodule by repeating the matching procedure restricting consideration to hits within that supermodule. This also enables the linking efficiency between planar segments to be determined.

The track reconstruction efficiency as a function of the pseudo-rapidity, η , of the

generated particle is shown in figure 5.1a. Only particles with a $p_T > 0.3 \text{ GeV}/c$ were considered in order to reduce the effects of multiple scattering in the material between the tracking detectors. The efficiency is shown both for the minimum requirement that a reconstructed track must consist of at least one planar segment and for the requirement that a track must consist of at least two planar segments. In order to restrict the analysis to a region of high acceptance for the remainder of this analysis, consideration was restricted to the region $2.0 < \eta < 2.5$. The average efficiency in the above η range is approximately 85% and 40% if at least one or two planar segments are required respectively. The track reconstruction efficiency as a function of the transverse momentum, p_T , of the generated particle in the above η range is shown in figure 5.1b. The efficiency is approximately independent of p_T in the region $p_T > 1.0 \text{ GeV}/c$. Below $1.0 \text{ GeV}/c$ the efficiency falls approaching $0.3 \text{ GeV}/c$, varying by approximately 5% over this range.

The forward region is a particularly hostile environment for track reconstruction. In particular, a large number of secondary tracks are produced from interactions with the material in the end wall of the CTD and around the beam pipe, as well as secondary interactions with a collimator situated in the beam pipe at $z=204 \text{ cm}$ which further increases the track multiplicity at the rear of the tracker. Consequently, a large percentage of the tracks which enter the forward tracker are products from secondary interactions, and the total multiplicity in the forward region is typically high.

The high multiplicity in the forward tracker has a strong effect on the efficiency of track reconstruction. This is illustrated in figure 5.2 in which the track reconstruction efficiency is shown as a function of the total number of tracks in the forward tracker. For the minimum requirement that a reconstructed track consists of at least one reconstructed planar segment, the track reconstruction efficiency is not strongly dependent on the total track multiplicity. However, if at least two reconstructed planar segments per track are required, then a strong dependence on the total track multiplicity is introduced.

The dependence of the measured efficiency on the total track multiplicity can

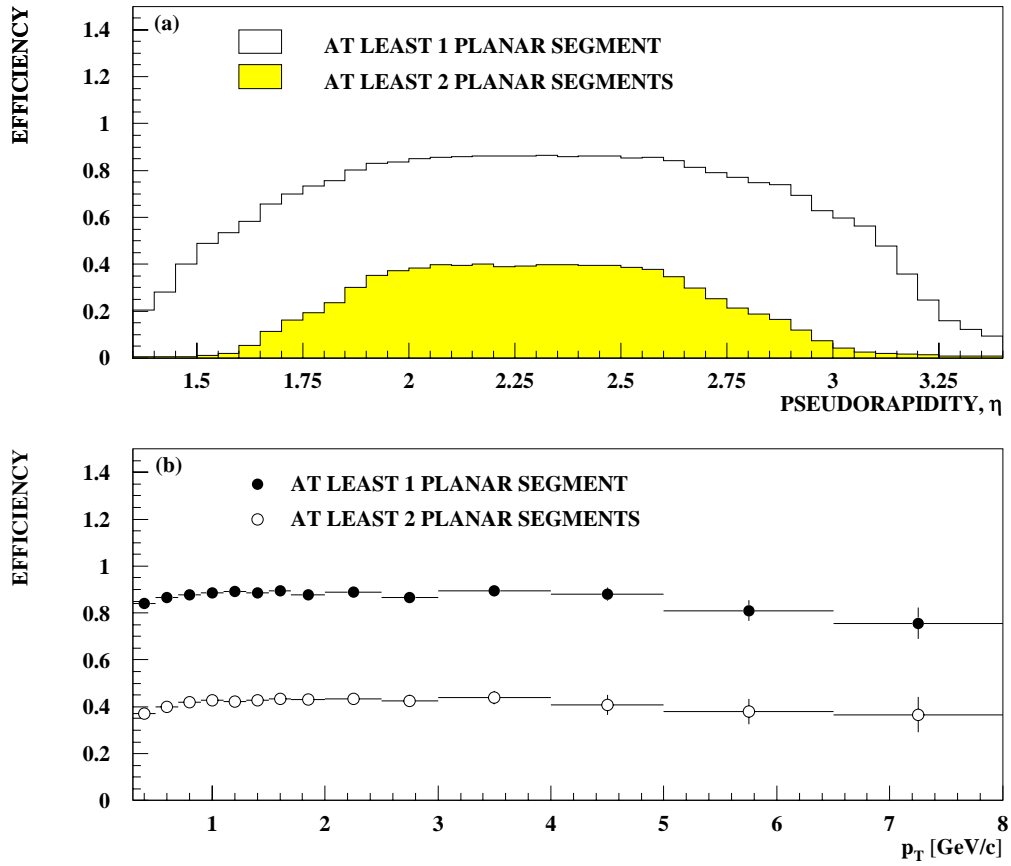


Figure 5.1: The average track reconstruction efficiency as a function of (a) pseudo-rapidity, η , and (b) transverse momentum, p_T .

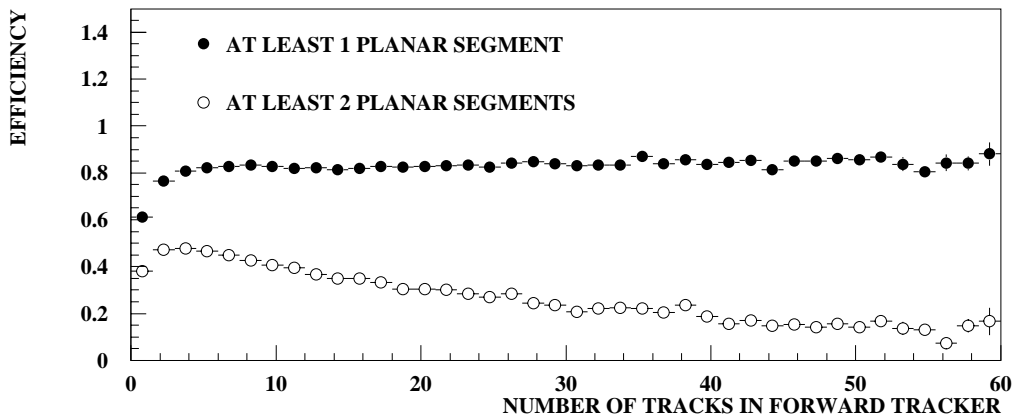


Figure 5.2: The average track reconstruction efficiency as a function of the total number of reconstructed tracks in the forward tracker.

be understood in terms of the planar segment efficiency and the linking efficiency between the individual chambers. From figure 5.3, it can be seen that the planar segment efficiency in each supermodule is relatively independent of the total track multiplicity. This implies that the strong dependence of the efficiency on the total track multiplicity when at least two planar segments per track are required is a result of the deterioration of the linking efficiency between planar segments at high multiplicities. This can be seen in figure 5.4 in which the linking efficiency between the respective supermodules is shown as a function of the total track multiplicity in the forward region.

The deterioration in the linking efficiency as a function of the total track multiplicity is due to the poor reconstruction of planar line segments at high multiplicities. This can be seen by considering simulated particles from the event vertex for which a matched planar segment has been reconstructed in each supermodule. Particles with a matched reconstructed track consisting of a planar segment in the second and third supermodule were then selected. Figure 5.5a shows the ratio R1 of the planar segment in the first supermodule for the case where the planar segment has been successfully linked to the remainder of the track. Also in figure 5.5b the distance,

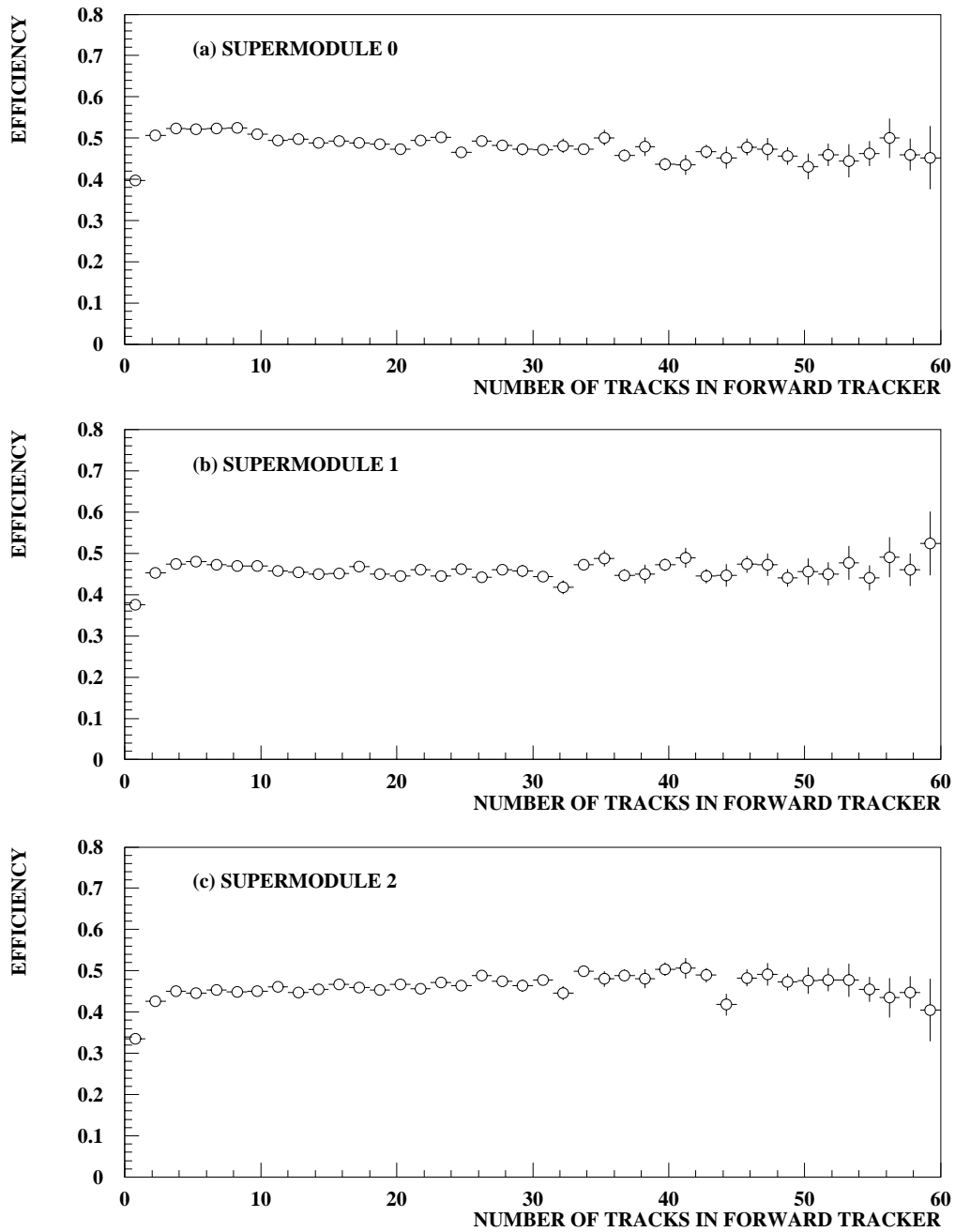


Figure 5.3: The average planar segment reconstruction efficiency as a function of the total number of reconstructed tracks in the forward tracker for each respective supermodule.

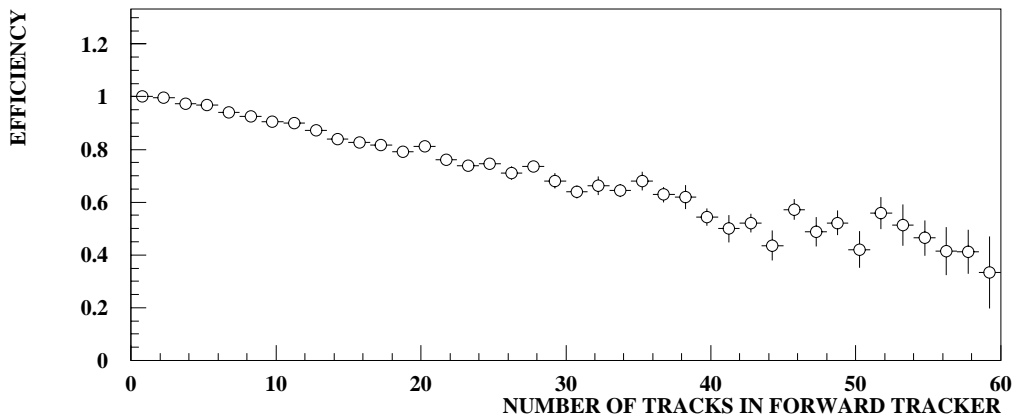


Figure 5.4: The planar segment linking efficiency as a function of the total number of reconstructed tracks in the forward tracker.

ΔR , in the $x - y$ plane between the extrapolated generated track and the reconstructed planar segment at the face of the first supermodule. The distributions $R1$ and ΔR are also shown in figure 5.5c and figure 5.5d for the case where the planar segment in the first supermodule has failed to be linked to the remainder of the track.

For the majority of cases where the planar segment in the first supermodule has been successfully linked to the remainder of the track, the ratio $R1$ is unity and hence the planar segment is pure and has been well reconstructed. Also in this case the distance ΔR is typically less than 5 mm. However for the case that the planar segment has failed the linking procedure the distribution of $R1$ shows a significant peak at approximately $R1=0.3$. Also the distribution of the distance ΔR shows a long tail up to $\Delta R=60$ cm. This indicates that for the majority of these cases the planar segment has not been properly reconstructed in the first supermodule. In fact for the majority of these cases three unconnected clusters have been falsely combined together giving a peak in the distribution of the ratio $R1$ at $R1=0.3$. Clearly, though the above matching procedure has associated the resulting planar segment with one particle from the event vertex, which particle the segment is

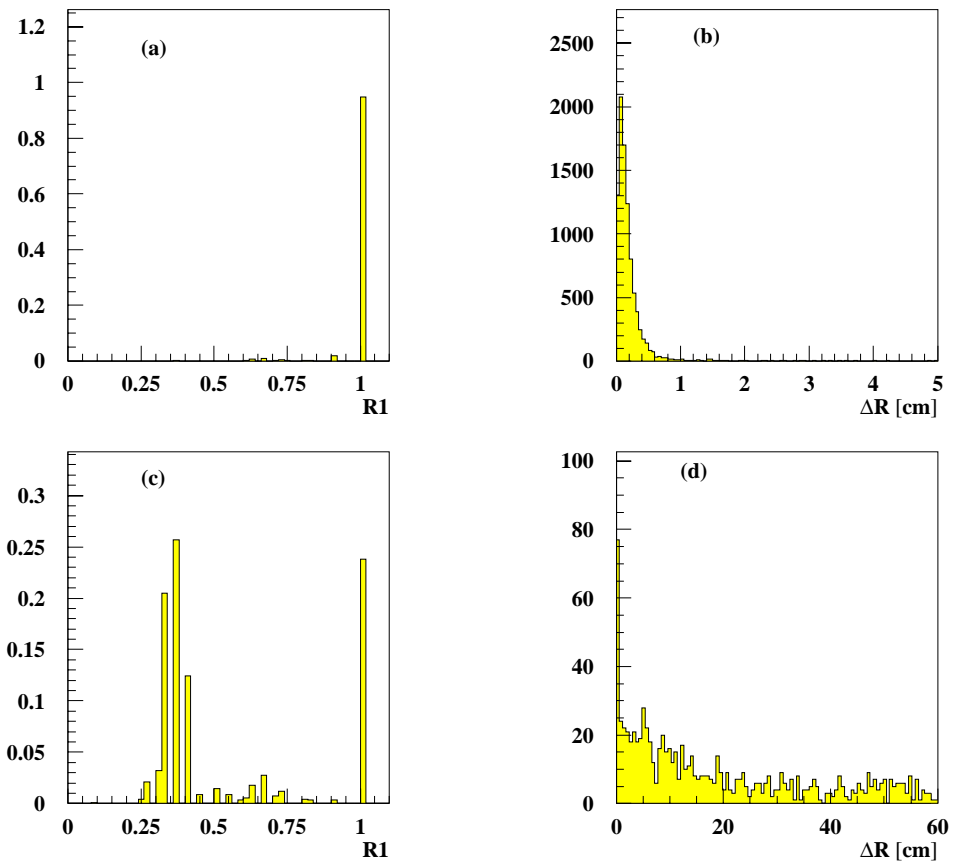


Figure 5.5: The distributions of the ratio $R1$ and the distance ΔR for (a),(b) particles matched to three successfully linked planar segments, and (c),(d) particles in which the matched planar segment in the first supermodule has failed to be linked to the remainder of the track in the second and third supermodules.

matched to is somewhat arbitrary. A peak in the distribution of $R1$ at unity is however still seen for the case where the planar segment in the first supermodule has failed the linking procedure. This is a result of the inherent linking inefficiency between good reconstructed planar segments. A corresponding peak is also seen in the distribution of ΔR . This corresponds to approximately 25% of these cases, and is due to a linking inefficiency between true planar segments of approximately 2%.

The above suggests that it would be desirable to select two planar segment tracks in order to exclude poorly reconstructed single planar segment tracks from the subsequent analysis. The requirement that at least two planar segment tracks have been successfully linked together will increase the hit purity of the resulting track sample. It should be noted that the rejection of single planar segment tracks with low values of the ratio $R1$ cannot be achieved at the reconstruction level by applying a cut to the χ^2 of the track parameterisation, as this quantity has already been used in the combination of clusters in the track reconstruction. The observation of poor quality tracks is a consequence of the inadequacy of such an approach for events with high track multiplicities. The track selection will be discussed in detail in section 5.5.

Attempts have been made to parameterise the efficiency in terms of a localised track density. However it is clear from figure 5.5 that the efficiency cannot be parameterised as a function of a simple track density within a certain distance ΔR in the $x - y$ plane of the track under consideration. This is a consequence of the geometry of the planar chambers and the fact that a cluster within an orientation only determines a plane. Clearly a false intersection of three unconnected planes can be formed at large values of ΔR . Nevertheless attempts were made to describe the efficiency in terms of a track density within an area defined using the geometry of the planar orientations. However, this was found to be problematic due to the effect of the limited resolution of tracks reconstructed in only one planar segment and due to the loss of clusters within the reconstruction procedure. Instead, the efficiency has been parameterised as a function of the total number of tracks in the forward tracker. The application of the efficiency in correcting the measured track

multiplicity will be discussed in chapter 7.

5.4 Comparison of the Track Reconstruction Efficiency between Data and MC

The track reconstruction efficiency has been compared between data and MC using the inherent redundancy in the forward tracker. This has been achieved by searching for missing track segments in each respective supermodule using tracks measured both before and after the supermodule under consideration. How this is achieved differs slightly for each planar module. For the first supermodule in order to achieve a reliable determination of the planar segment efficiency a sample of tracks reconstructed in both the central tracker, and in either the second or third planar chambers was used to determine the planar segment efficiency. The measured efficiency is then the ratio of the number of such tracks that have a planar segment in the first supermodule to the total number of selected tracks. This can be repeated for the second supermodule using tracks with a planar segment in the first and third supermodules, and for the third supermodule with tracks with a planar segment in either the first or second supermodule and a radial segment in the third supermodule. The angular range that can be tested varies for each respective supermodule, and a full coverage of the forward tracker cannot be achieved.

A comparison of the measured efficiency for data and Monte Carlo as a function of the total track multiplicity in the forward tracker is shown in figure 5.6. The measured efficiency is slightly higher in data than in Monte Carlo particularly for supermodule 0. The efficiency that is determined using this approach is a combination of the actual planar segment efficiency and the linking efficiency between supermodules. However the form of the dependence of the measured efficiency on the total track multiplicity is well modelled by the Monte Carlo. This strongly suggests that the linking efficiency between individual supermodules is well modelled by the Monte Carlo simulation, and that the difference in the efficiency determined in this way is a result of a constant absolute difference in the planar segment efficiency

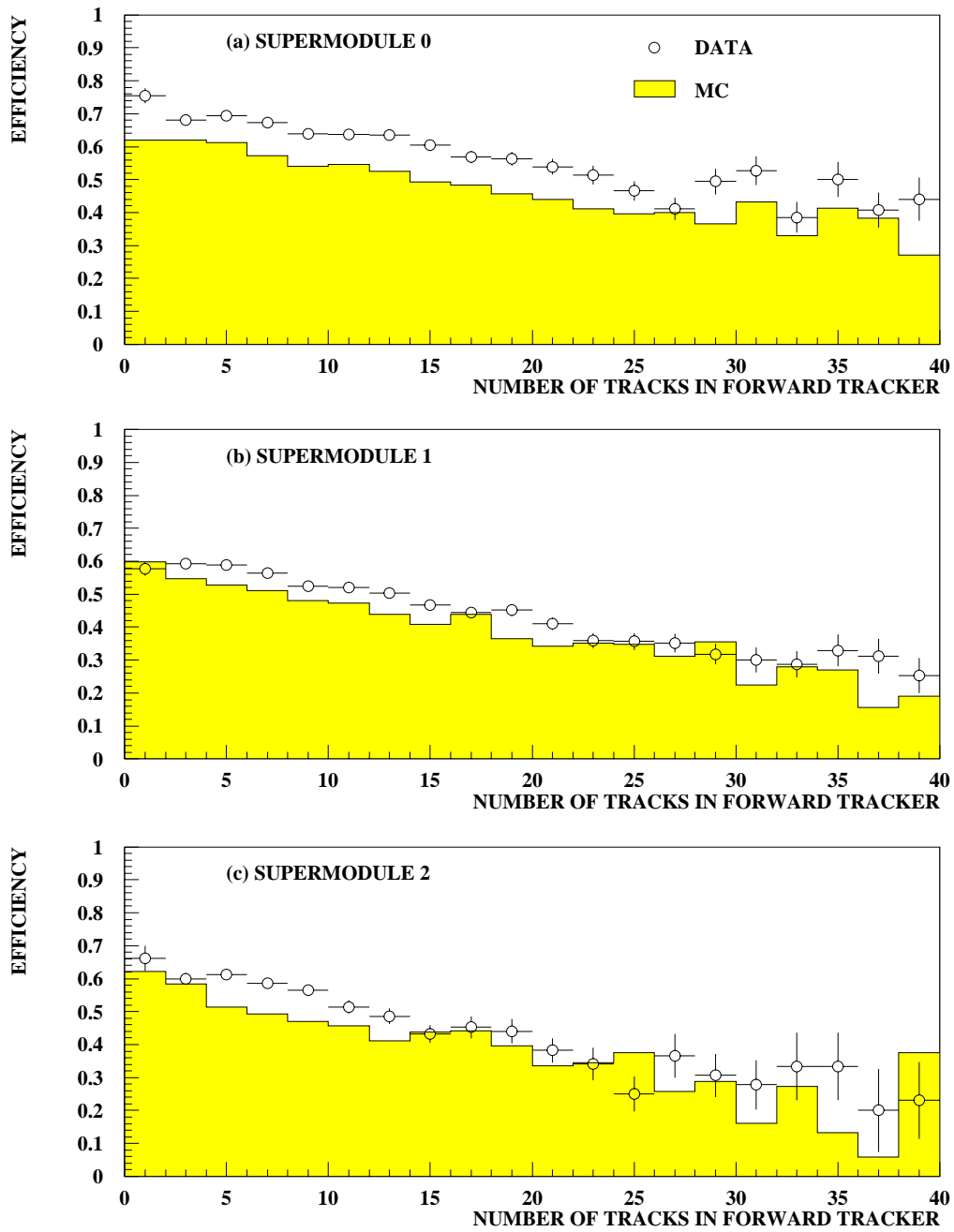


Figure 5.6: A comparison of the ‘missing segment efficiency’ between data (points) and MC (filled histogram) for each supermodule.

between data and Monte Carlo.

The planar segment efficiency is modelled by the Monte Carlo simulation by applying the following losses to a perfect detector description :

- Firstly the single wire hit efficiency is modelled by the MC simulation.
- A dead wire map determined from the data is applied to allow for dead cells and wires.
- Finally a global factor is applied to account for the apparent correlated loss of clusters within an orientations

The final factor in the Monte Carlo simulation was at the time of this report not well understood, and is the subject of study by the forward tracker detector group. Consequently a rather ad hoc method has been applied in the Monte Carlo simulation with a global factor per supermodule to account for this correlated loss. The disagreement in efficiency between data and Monte Carlo can be attributed to the mis-tuning of these parameters.

Due to the observed difference in efficiency between data and Monte Carlo it is necessary to correct for the discrepancy in applying the track reconstruction efficiency as determined from the Monte Carlo simulation. This will be discussed in more detail in chapter 7

5.5 Track Selection

A large percentage of tracks that are reconstructed in the forward tracker will in fact come from secondary interactions either due to interactions with the material between the end wall of the CTD and the forward tracker or alternatively due to secondary interactions with the beam pipe and collimator C3.

In determining the optimum track selection criteria, consideration must be given to the effect on the track reconstruction efficiency. The selection is a trade-off between the reduction in efficiency and the increased purity of the sample of tracks. The track selection criteria have been optimised using the track matching procedure

in the MC simulation. It is then possible to determine whether a track is a primary track from the event vertex or the result of a secondary interaction with material in the detector. Tracks due to particle decays are also considered as secondary tracks in this discussion. In the following, reconstructed tracks matched to primary particles from the event vertex are referred to as ‘primary reconstructed tracks’. Similarly tracks matched to products from secondary interactions are referred to as ‘secondary reconstructed tracks’.

A physical track in the reconstruction must consist of at least one planar segment. Tracks with only one planar segment are however largely unconstrained in momentum. Furthermore, as shown in section 5.3, a significant percentage of these tracks will be very poor quality at the hit level. Consequently, only tracks with at least two planar segments were considered for the subsequent analysis.

After a track has been reconstructed in the forward tracker, a fit to the interaction vertex is applied. For tracks reconstructed in the forward tracker, this is achieved by adding the reconstructed vertex position as an extra coordinate to the track. Tracks are not therefore required to pass exactly through the vertex. The cuts applied in the vertex constraint in the reconstruction are rather loose. This can be improved by applying a cut to the χ^2 of the vertex fit. The effect of such a cut is illustrated in figure 5.7 which shows the percentage of primary reconstructed tracks accepted as a function of the cut applied to the χ^2 of the vertex fit. Figure 5.7 also shows the percentage of secondary reconstructed tracks rejected by the vertex constraint. The vertex fit applied in the reconstruction is equivalent to a χ^2 cut of $\chi^2=50$. This accepts approximately 80% of primary reconstructed tracks, whilst rejecting approximately 45% of secondary reconstructed tracks. Tightening the cut applied to χ^2 of the vertex fit improves the rejection of secondary tracks at the expense of a slightly reduced efficiency. However, due to uncertainties in the determination of the χ^2 of the vertex fit, no additional cut was applied and all tracks constrained to the interaction vertex in the reconstruction were considered in the subsequent analysis.

For tracks constrained to the interaction vertex, the track parameters are recal-

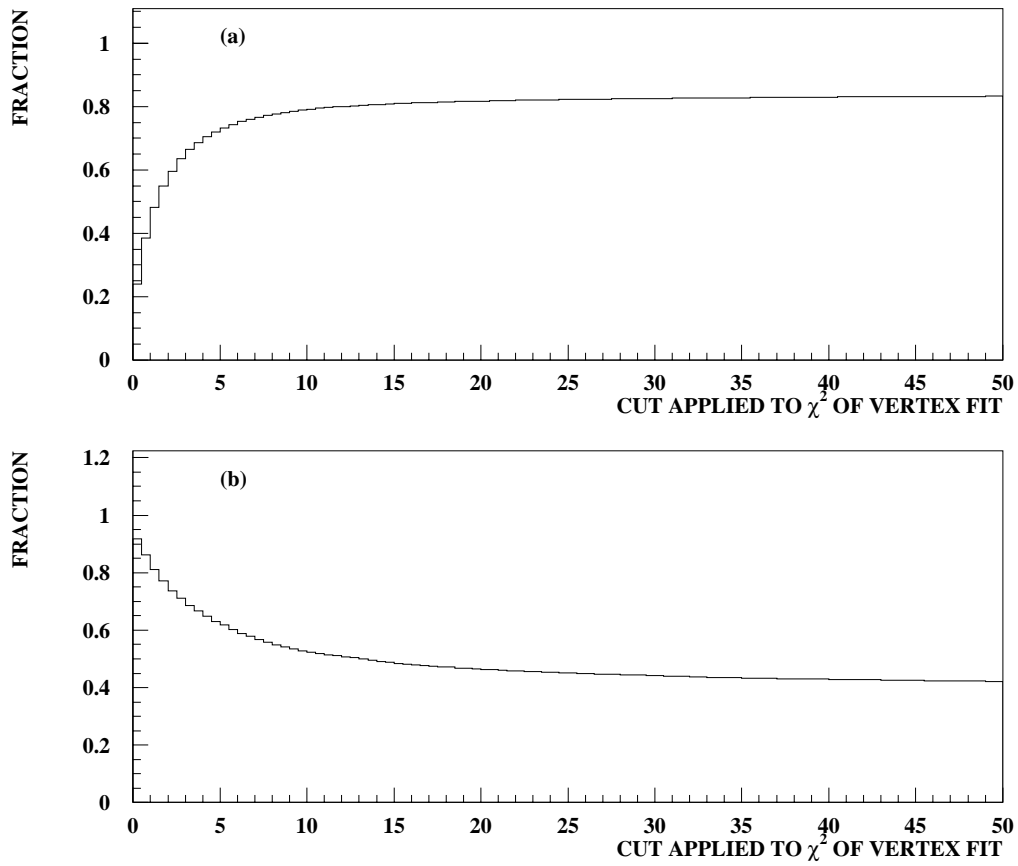


Figure 5.7: The percentage of (a) primary reconstructed tracks accepted and (b) secondary reconstructed tracks rejected as a function of the cut applied to the χ^2 of the vertex fit.

culated using the interaction vertex as an additional point on the track. This can lead to an improved determination of the momentum for tracks correctly assigned to the interaction vertex. This is shown in figure 5.8 in which the resolution in $1/p$ is shown for tracks with $p_T > 0.3 \text{ GeV}/c$ both with and without a vertex constraint. The resolution is well described by an analytical fit to a generalised Breit-Wigner¹. The resolution in $1/p$ is improved significantly by considering only vertex constrained tracks.

In addition to the application of a vertex constraint, the likelihood that a track was produced in the primary interaction can be improved by considering the results of an extrapolation of the track to the vertex. The extrapolation can be parameterised in terms of the distance of closest approach, DCA, of the extrapolated track from the event vertex and the quantity, $|Z_0 - Z_{\text{VTX}}|$, where Z_0 is the z -coordinate of the track at the distance of closest approach. The effect of the vertex constraint on the distribution of these two variables is shown in figure 5.9. The application of a vertex fit restricts the above distributions to the region $|Z_0 - Z_{\text{VTX}}| < 40 \text{ cm}$ and $|DCA| < 4 \text{ cm}$.

The distribution of the above track variables is shown for primary and secondary reconstructed tracks respectively in figure 5.10. The effect of applying a cut to the above track parameters is illustrated in figure 5.11 in which the percentage of primary reconstructed tracks accepted and secondary tracks rejected is shown as a function of the cut applied to each track variable respectively. Applying a cut to either of these variables reduces the contamination due to secondary reconstructed tracks at the expense of a reduced track reconstruction efficiency. Clearly, neither variable enables a perfect discrimination between primary and reconstructed tracks. Finally, the observed distributions of the variables DCA and $Z_0 - Z_{\text{VTX}}$ are compared between data and Monte Carlo in figure 5.12. The distributions of the above track

¹A generalised Breit-Wigner distribution is defined as :

$$G(x) = \alpha(1 + [2^{\frac{1}{\beta}} - 1](\frac{x - \bar{x}}{\gamma})^2)^{-\beta}.$$

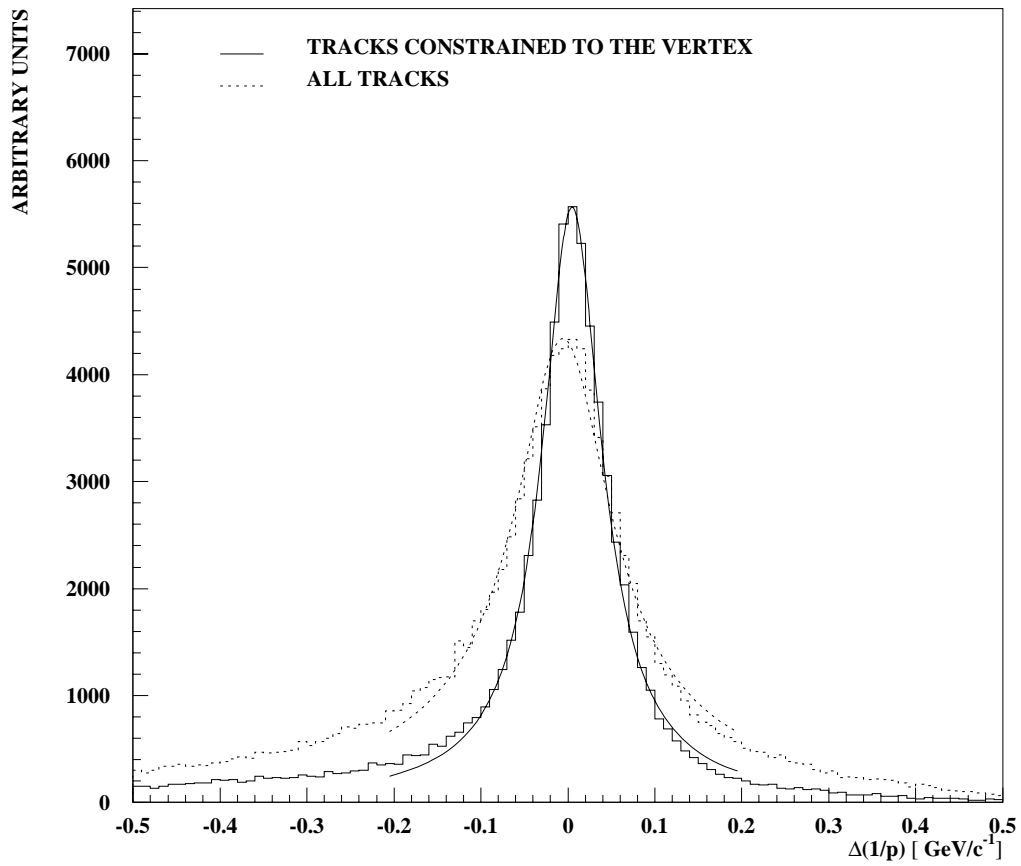


Figure 5.8: The reconstructed track resolution in $1/p$ before (dashed histogram) and after (solid histogram) the vertex constraint.

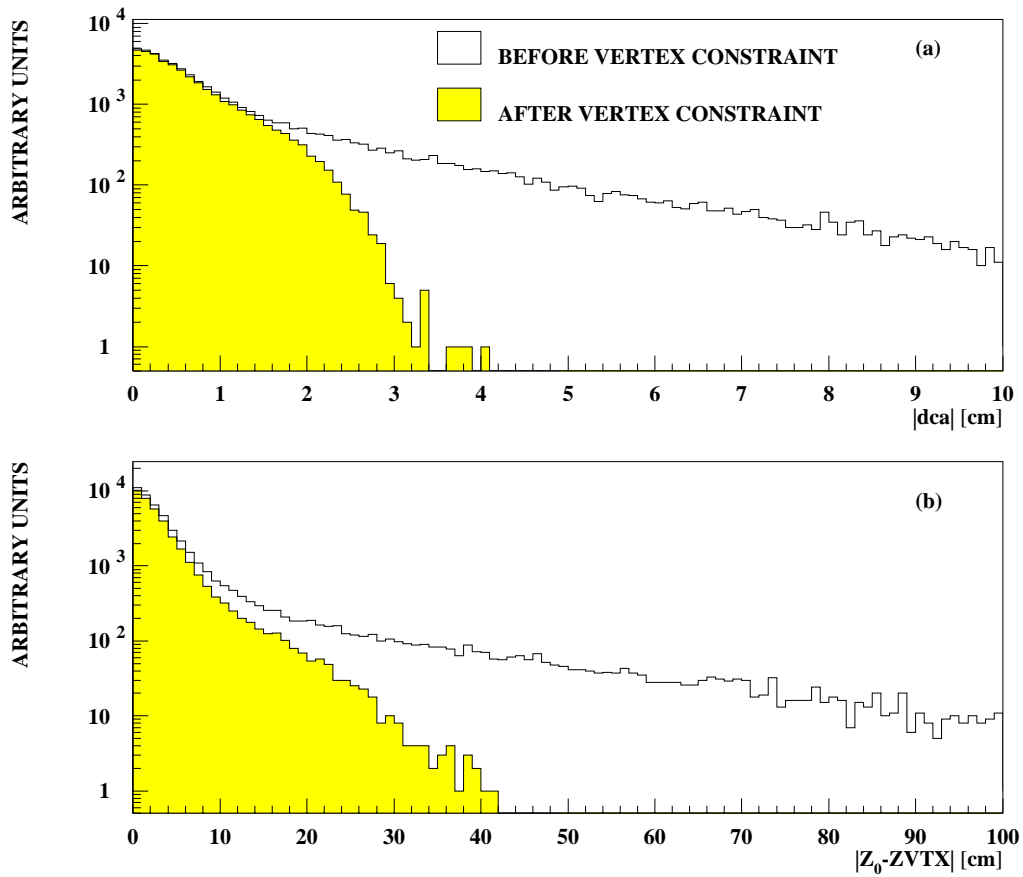


Figure 5.9: The distributions of (a) $|DCA|$ and (b) $|Z_0 - Z_{vtx}|$ before and after the vertex constraint.

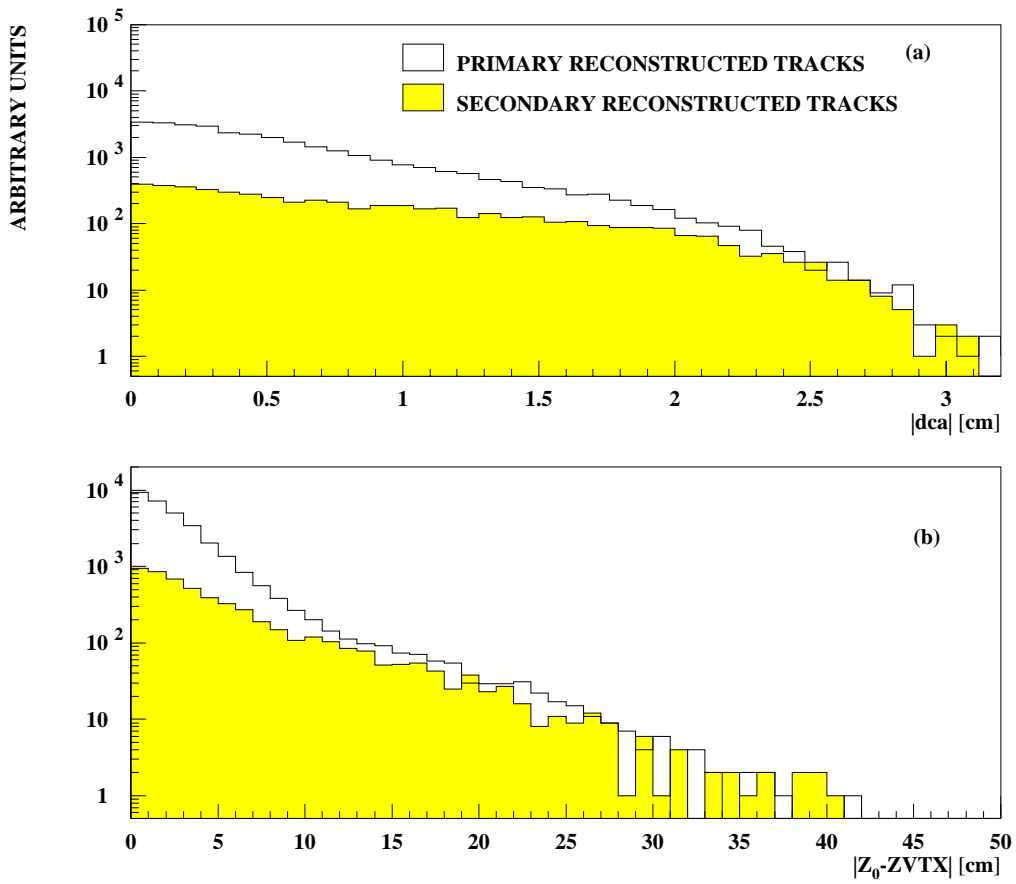


Figure 5.10: The distributions of the track parameters a) $|DCA|$, b) $|Z_0-ZVTX|$ for primary reconstructed tracks (empty histogram) and secondary reconstructed tracks (filled histogram).

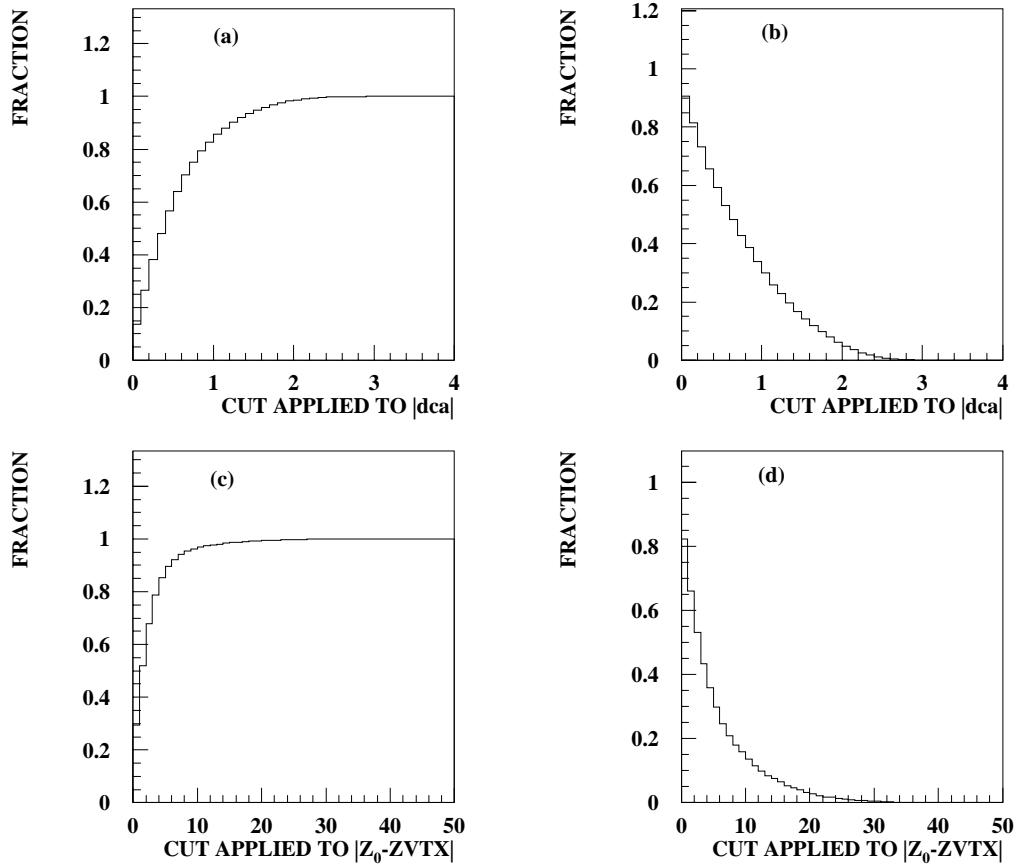


Figure 5.11: The percentage of primary tracks accepted, (a),(c), and the percentage of secondary tracks rejected, (b),(d), as a function of the track parameters $|DCA|$, $|Z_0-Z_{vtx}|$.

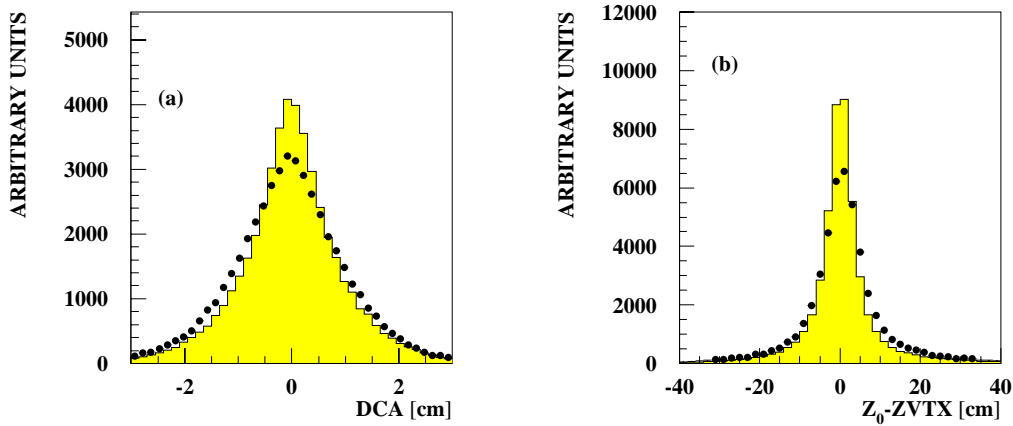


Figure 5.12: A comparison of the of the track parameters (a) DCA, and (b) Z_0-Z_{VTX} between data (points) and Monte Carlo (histogram).

variables for the selected data sample show a broader distribution than expected from the MC simulation. This can be interpreted in two ways, either a) the effect of a reduced resolution for the data compared with the MC or b) the effect of an increased contamination due to secondary tracks.

In view of the above discrepancy between the observed distributions between data and MC, conservative cuts were applied to these variables, and consideration was restricted to tracks with $|DCA| < 2\text{cm}$ and $|Z_0-Z_{vtx}| < 10\text{cm}$. In addition to the above criteria, loose cuts were applied to the error in the reconstructed momentum of the track ($\Delta p/p$) and the $\chi^2/\text{per degree of freedom}$ of the track parameterisation. In total, in the following analysis tracks reconstructed using the forward tracker were considered if

- the track has been successfully constrained to the primary vertex;
- the track consists of at least two planar segments;
- $2.0 < \eta < 2.5$;
- $p_T > 0.3 \text{ GeV}/c$;

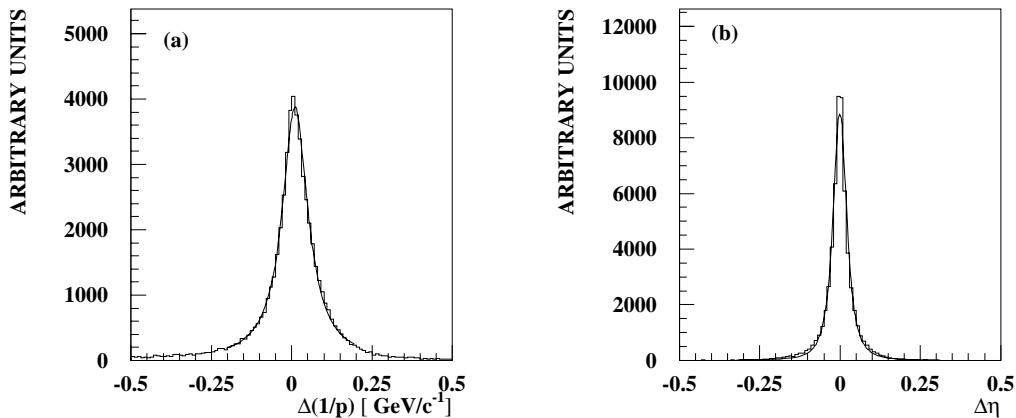


Figure 5.13: The reconstructed track resolution in (a) $1/p$ and (b) pseudorapidity, η , after the full track selection.

- $|DCA| < 2 \text{ cm};$
- $|Z_0 - Z_{vtx}| < 10 \text{ cm};$
- $|\Delta p/p| < 1.0;$
- $|\chi^2/NDF| < 30.$

Following the above track selection the resolution of the selected tracks in $1/p$ and η is shown in figure 5.13.

Any track selection cannot reject all secondary tracks and hence the results of the MC simulation must be used in correcting the measured track multiplicity in the photoproduction data. The track selection efficiency and the contamination due to secondary reconstructed tracks has again been studied using the track matching procedure in the MC simulation.

The track selection efficiency is defined as the ratio of the number of primary reconstructed tracks passing the above track selection to the total number of primary reconstructed tracks. The efficiency is shown in figure 5.14 as a function of the total number of tracks observed in the forward tracker and the transverse momentum of the track respectively. The track selection efficiency deteriorates significantly for

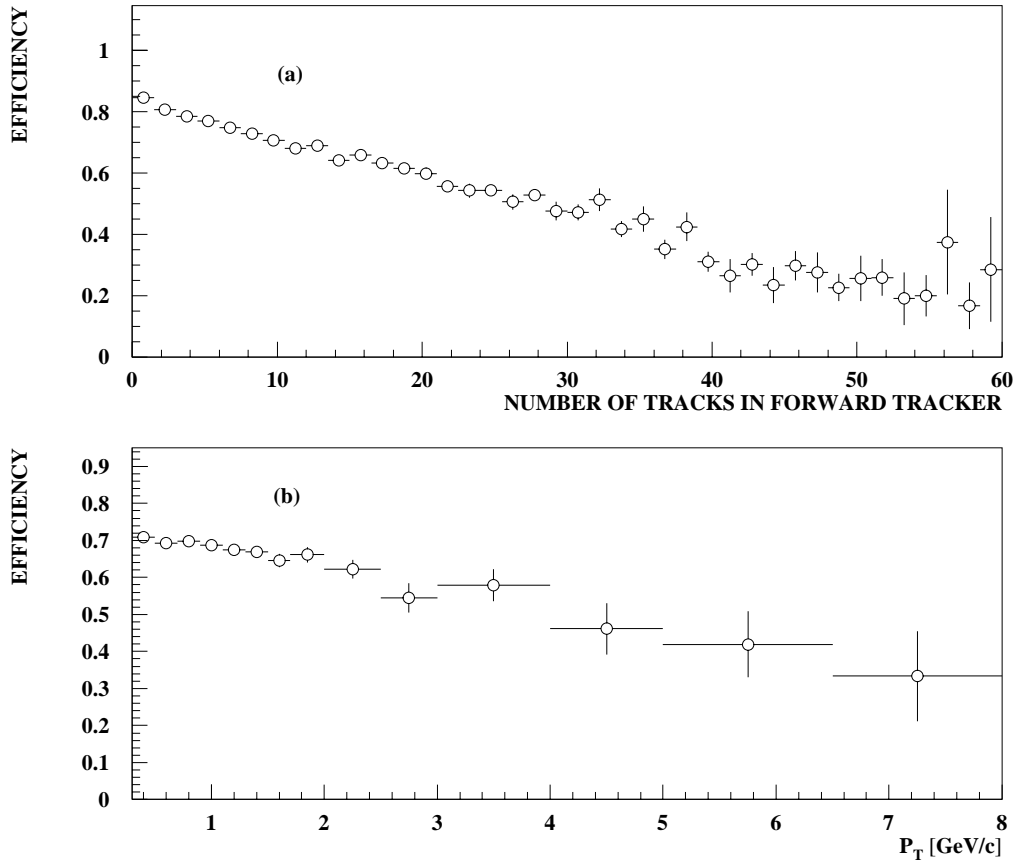


Figure 5.14: The average track selection efficiency as a function of (a) the number of reconstructed tracks in the forward tracker and (b) the transverse momentum of the track.

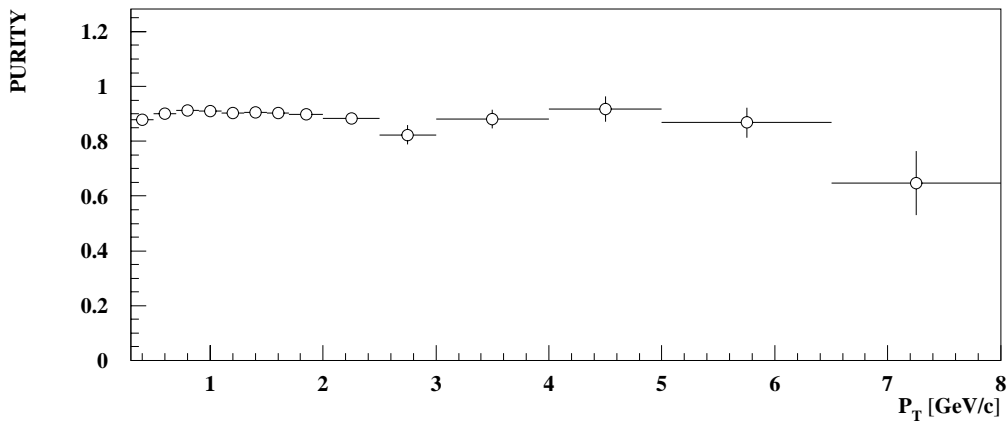


Figure 5.15: The track purity as a function of the transverse momentum of the track.

events with a high track multiplicity. This is a consequence of the deterioration in the planar segment reconstruction at high multiplicities. The track selection efficiency also deteriorates significantly with increasing transverse momentum.

Finally the track purity is shown as a function of the transverse momentum of the track in figure 5.15. The track purity is defined as the fraction of the total number of tracks selected that are due to primary reconstructed tracks. The track purity is approximately independent of the transverse momentum of the track with an average value of approximately 90%.

5.6 Summary

The efficiency of track reconstruction in the forward tracker has been studied in the forward region and is found to be strongly dependent on the multiplicity in the forward region. The reason for this strong dependence has been studied and is related to the poor reconstruction of planar segments for events with high multiplicities. The average track reconstruction efficiency has been determined by a Monte Carlo simulation to be approximately 85% for tracks with at least one planar segment

and approximately 40% for the additional requirement that a track consists of at least two planar segments. The efficiency has been compared between data and MC using the inherent redundancy in the forward tracker. It has been found that the planar segment efficiency is between 5 and 10% higher in data than in Monte Carlo, depending on the supermodule under consideration. This is due to the apparent correlated loss of clusters of hits within the data, which is not well modelled by the Monte Carlo simulation.

A set of criteria has been discussed in order to select tracks from the primary event vertex. The effect of the track selection on the efficiency of the reconstruction has been determined using a MC simulation. The track selection efficiency has been found to be dependent both on the transverse momentum of the track and the track multiplicity in the forward tracker. The purity of the track sample after the full track selection has been determined and is found to be approximately 90%. The resolution in the track parameters η and p_T has been shown for the selected tracks.

Chapter 6

The Photoproduction of Jets at HERA

6.1 Introduction

Photoproduction is dominated by low p_T , soft interactions in which the final state kinematics can essentially be described by longitudinal phase space. However, at HERA energies, hard scattering processes, characterised by high transverse momenta in the hadronic final state and the production of jets, have clearly been observed [39, 43]. Such events can reveal the underlying dynamics of the constituents of the photon, and are of considerable theoretical interest.

However studies of jet production at HERA have shown that the measured energy flow away from the jet axis is not well described by QCD calculations, even with the inclusion of QCD radiation and hadronisation models [41, 42]. This was found to be particularly noticeable in the forward region. Before studying the charged particle multiplicity in the forward region using the H1 Forward Tracker, an analysis into the energy flow in events with at least one reconstructed jet is presented and the observed discrepancy between data and LO QCD generators is illustrated. The possibility that the discrepancy in the energy flow is due to the presence of multiple interactions is discussed.

6.2 Jet Reconstruction

In leading order (LO) QCD calculations, hard photoproduction events are typified by the production of two high p_T outgoing partons from the hard scattering process. The outgoing partons cannot, however, be observed experimentally due to the confinement mechanism of QCD. Instead the resulting hadrons from the fragmentation procedure are observed in the detector, typically in the form of two well collimated jets of hadrons. The kinematics of the hard scattering can however be reconstructed from the resulting jets, enabling experimental results to be compared with theoretical predictions from perturbative QCD (pQCD).

The experimental definition of a jet is not well defined, and several techniques are available to reconstruct jets. In this analysis a cone algorithm, such as first used by the UA1 collaboration, has been considered. This algorithm assumes that jets have a fixed radial size in the η/ϕ plane, where η is the pseudo-rapidity of a particle and is given by

$$\eta = \frac{1}{2} \ln \frac{(P + P_z)}{(P - P_z)} = -\ln\left(\tan \frac{\theta}{2}\right) \quad (6.1)$$

Essentially, the UA1 type algorithm determines jets by looking for large depositions of transverse energy within cones given by a certain fixed radius in the η/ϕ plane. Such algorithms are ideally suited to photoproduction and consequently the majority of theoretical calculations are performed using such a jet definition. For the remainder of this analysis, a UA1 type jet reconstruction routine, QJCALO [71], will be considered.

6.2.1 The QJCALO algorithm

The QJCALO jet algorithm is a cone algorithm, initially developed to reconstruct jets using calorimeter cells. The first stage in reconstructing the jets in an event is to map the energy observed in the detector onto a two dimensional η/ϕ grid. Jets are then reconstructed by considering grid elements with an E_T above a given threshold ($E_{T,thr}^{ini}$) as jet initiators. All grid elements within a distance Δr in the η/ϕ plane,

given by

$$\Delta r = \sqrt{(\eta_{bin} - \eta_{ini})^2 + (\phi_{bin} - \phi_{ini})^2}, \quad (6.2)$$

less than a given radius (R_{limit}) are vectorally added to the jet initiator to reconstruct a jet candidate. Those candidates which pass a final E_T cut ($E_{T,thr}^{jet}$) are selected as jets.

In the QJCALO algorithm the grid element with the highest E_T above the initiator threshold is used to reconstruct the first jet candidate. An iterative approach is then considered, in which a new cone is drawn around the initial jet axis. The jet axis is then recalculated using the new cone definition. This is repeated until the jet axis remains unchanged.

If the resulting jet candidate is above the final E_T threshold the grid elements belonging to the jet are locked from further consideration. However, if the jet candidate fails the final E_T cut then the jet is immediately rejected and the grid elements used are released for consideration in further jet candidates. The next highest E_T grid element is then considered.

The parameters used in the above jet algorithm are :

- $E_{T,thr}^{ini}$, the threshold for a grid element to be considered as a jet initiator,
- R_{limit} , the cone size in the η/ϕ plane,
- and $E_{T,thr}^{jet}$, the minimum E_T for a jet to be accepted.

For this analysis an η/ϕ grid with 25 elements in η in the range $-2.0 < \eta < 3.0$ and 25 elements in ϕ was used. Calorimeter cells reconstructed in the LAr and BEMC calorimeters were used. A cone size, R_{limit} , of 1.0 was used for this analysis with a final E_T threshold of $E_{T,thr}^{jet} = 7.0$ GeV. The initiator threshold was set as $E_{T,thr}^{ini} = 0.2$ GeV.

The performance of the jet reconstruction has been studied by relating the reconstructed jets to the leading order outgoing partons from the hard subprocess using the distance between the reconstructed jet axis and the nearest outgoing parton in the η/ϕ plane. The distance Δr in the η/ϕ plane between the reconstructed jet axis

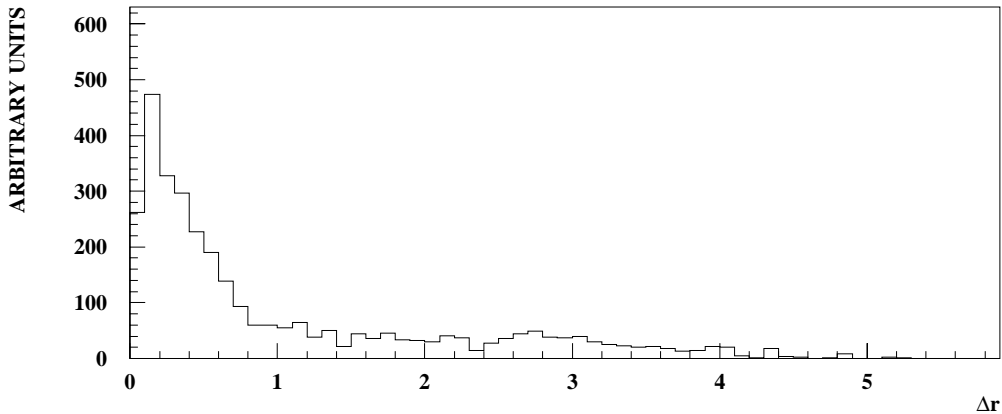


Figure 6.1: The distance Δr in the η/ϕ plane between the reconstructed jet axis and the nearest outgoing parton for jets with $E_T > 7\text{GeV}$ in the angular range $-1.0 < \eta < 2.0$, determined using the PYTHIA Monte Carlo including multiple interactions.

and the nearest outgoing parton is shown in figure 6.1, determined by the PYTHIA Monte Carlo with the inclusion of the multiple interaction model implemented within the PYTHIA generator. A significant peak is seen in the region $\Delta r < 0.7$, indicating a strong correlation between the reconstructed jets and the outgoing partons from the leading order subprocess.

The correlation between the reconstructed jet quantities η and ϕ and the corresponding quantities of the nearest leading order outgoing parton in the η/ϕ plane is shown in figure 6.2. This further illustrates the strong angular correlation between the reconstructed jet axis and the nearest parton from the hard subprocess. However in both figure 6.1 and figure 6.2 there is a noticeable background of reconstructed jets which are not well related to the outgoing partons of the hard sub-process. In order to study the transverse energy resolution of the jet reconstruction these jets were excluded by only considering jets with $\Delta r < 0.7$. The correlation between the transverse energy of the reconstructed jet, E_T^{jet} , and the transverse momentum of the nearest outgoing parton is shown in figure 6.3. From this it can be seen that the

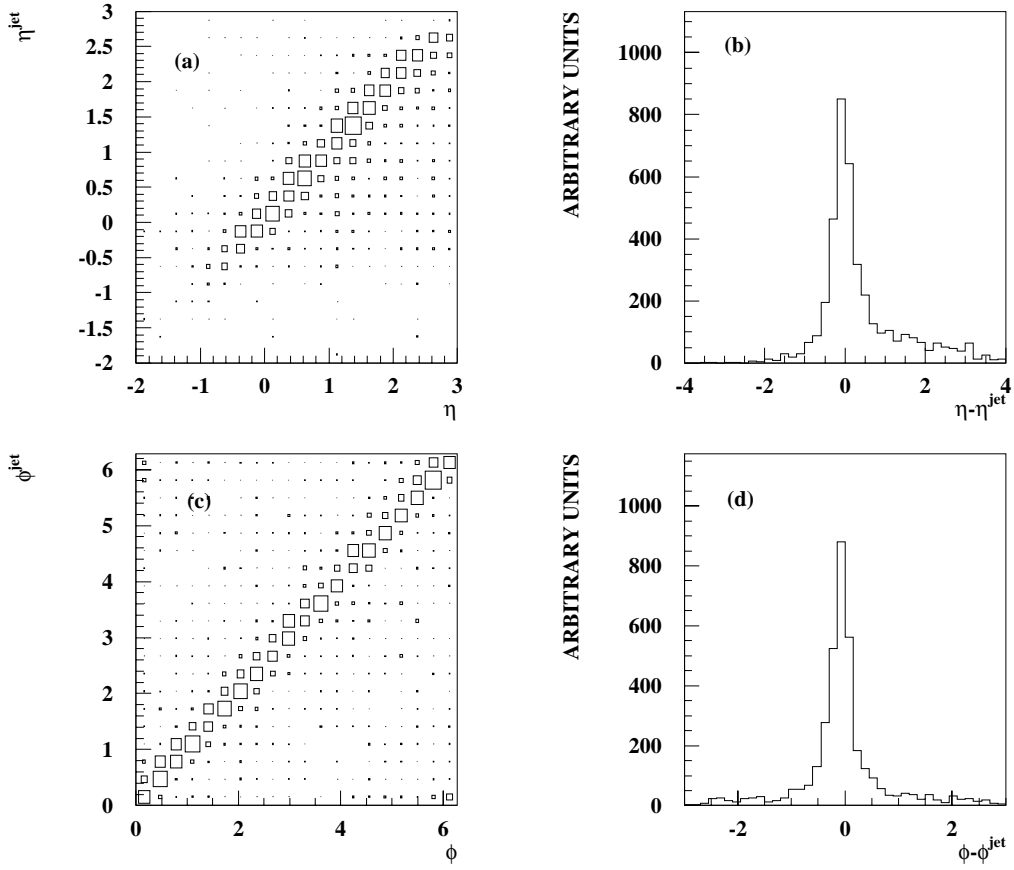


Figure 6.2: The correlation between the pseudorapidity, η , ((a),(b)) and azimuthal angle, ϕ , ((c),(d)) between the reconstructed jet axis and the nearest outgoing parton from the hard scattering, as determined by the PYTHIA Monte Carlo with the inclusion of multiple interactions.

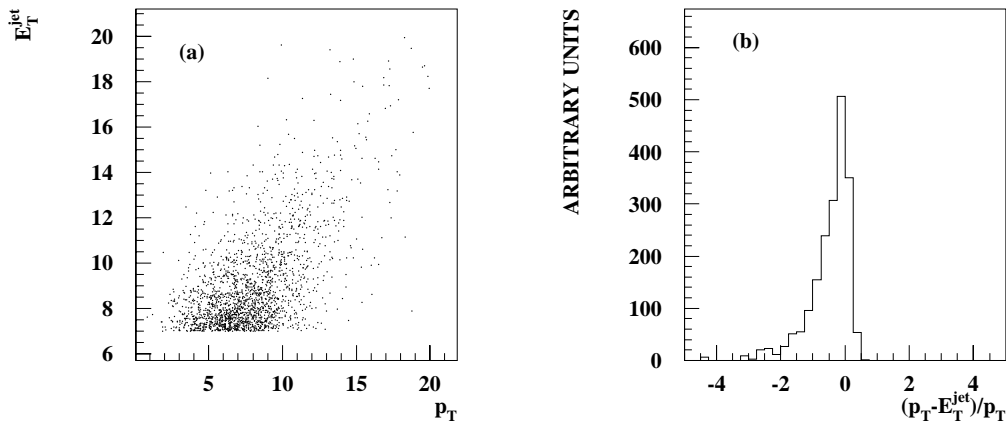


Figure 6.3: The correlation between the transverse energy, E_T^{jet} , of the reconstructed jet axis and the transverse momentum, p_T , of the nearest outgoing parton from the hard subprocess, as determined by the PYTHIA Monte Carlo with multiple interactions. Only jets within a distance $\Delta r < 0.7$ of the nearest outgoing parton are included.

correlation between the transverse energy of the reconstructed jet and the nearest outgoing parton is rather poor, compared with the angular correlation.

6.3 Jet Pedestals

In the previous section the correlation between the reconstructed jets and the outgoing partons from the hard sub-process was shown. In order to reconstruct the kinematics of the hard scattering it is necessary to unfold the reconstructed jet parameters to the partonic level. This requires a detailed understanding of the energy flow in such events. However the energy flow in hard photoproduction is complicated by the effect of higher order corrections and the fragmentation mechanism. Monte Carlo generators used at H1 are based on exact leading order matrix element calculations. The effect of initial and final state radiation and higher order corrections is taken into account using parton shower models. The fragmentation of the

outgoing partons is then taken into account using phenomenological models such as the Lund String Model (see section 4.4). However as discussed in section 2.4 there is also the possibility in resolved photoproduction for multiple interactions to occur. The presence of multiple interactions should be noticeable in the description of the observed jet pedestals, the energy flow outside of the jet cone.

In order to study the description of the energy flow in hard photoproduction events with a reconstructed jet, the QJCALO jet algorithm has been applied to the selected tagged data sample, triggered by a coincidence between a tagged electron and a track from the central jet chamber trigger. The distribution of the energy flow around the jet axis has then been compared between data and several Monte Carlo generators. Consideration was restricted to reconstructed jets with $E_T > 7\text{GeV}$ in the angular range $-1.0 < \eta < 2.0$. The observed jet profiles as a function of the difference $\Delta\eta$ and $\Delta\phi$ between the reconstructed jet axis and the calorimeter cell are shown in figure 6.4 in slices of $\Delta\phi < 1.0$ and $\Delta\eta < 1.0$ respectively. The observed jet profiles are compared with predictions from the PYTHIA Monte Carlo generator both with and without the inclusion of the multiple interaction model implemented within the PYTHIA generator. The jet profiles are shown for jets reconstructed in the angular range $-1.0 < \eta^{jet} < 0.5$ and $0.5 < \eta^{jet} < 2.0$ respectively.

It can be seen that the observed jet profiles are reasonably well described by the PYTHIA Monte Carlo both with and without the inclusion of multiple interactions for jets in the region $-1.0 < \eta^{jet} < 0.5$. However, for jets reconstructed in the forward region $0.5 < \eta^{jet} < 2.0$ the data shows a significantly increased jet pedestal compared with the results of the PYTHIA generator without the inclusion of multiple interactions. This is noticeable both in the distribution of the energy flow as a function of $\Delta\phi$ in which the data shows a less jet-like structure, and also in the distribution of the energy flow as a function of $\Delta\eta$ in which an excess of energy is seen in the data in the forward region $\Delta\eta > 0$. The inclusion of the possibility of multiple interactions improves the agreement between the data and the PYTHIA Monte Carlo (particularly the description of the η profiles). However it is clear that this still does not give a perfect description of the observed jet profiles, and does

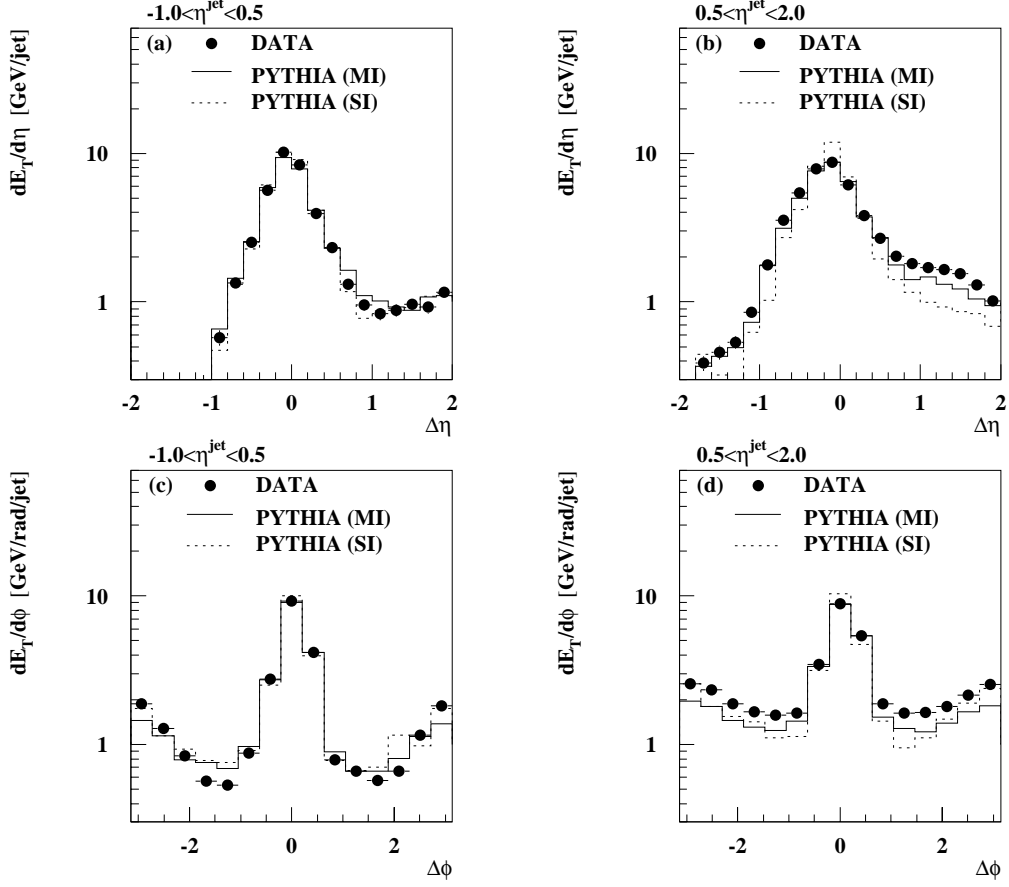


Figure 6.4: The observed transverse energy flow about the jet axis versus the pseudorapidity distance from the jet direction (integrated over $|\phi^{cell} - \phi^{jet}| \leq 1$) and the azimuthal angle with respect to the jet direction (integrated over $|\eta^{cell} - \eta^{jet}| \leq 1$). The jet profiles are shown for for two pseudorapidity bins: $-1.0 < \eta^{jet} < 0.5$ ((a),(c)) and $0.5 < \eta^{jet} < 2.0$ ((b),(d)). Full circles are H1 data. The curves refer to the predictions from the PYTHIA event generator with (full) and without (dashed) the inclusion of multiple interactions.

not fully account for the increased energy flow outside of the jet cone in the forward region.

The observed jet profiles have also been compared with the HERWIG generator. The HERWIG generator also includes an option to allow for multiple interactions by the inclusion of a ‘soft underlying event’. In this option a second typically soft interaction is superimposed on the initial hard interaction. However when this option is included a soft underlying event is included for every generated event, whilst it is expected that the number of interactions in the data will vary from event to event. The observed energy flow in the data can be modelled by mixing events generated with and without the inclusion of the soft underlying event option in a given ratio which then can be varied to improve the description of the data. Studies within the photoproduction working group at H1 have found that the best description of the data can be obtained by including the option of a soft underlying event for approximately 35% of events. The observed jet profiles are compared with the HERWIG generator, including a soft underlying event for 35% of events, in figure 6.5.

Also in figure 6.5, the observed jet profiles have been compared with expectations from the PHOJET generator. The PHOJET generator attempts to describe both soft and hard photoproduction within a consistent framework, and explicitly includes the possibility of multiple interactions. It is clear from figure 6.5 that the PHOJET generator overestimates the energy flow outside of the jet cone. This is particularly noticeable in the description of the jet profiles as a function of $\Delta\eta$ for jets reconstructed in the forward region.

An important consideration in the description of the observed energy flow in the data is the fluctuations in the jet pedestal. If the increased jet pedestal observed in the data is indeed due to the presence of multiple interactions then the number of interactions per event would be expected to vary on an event by event basis. Consequently, any model including multiple interactions must not only describe the average jet pedestal but also the fluctuations in the jet pedestal on an event by event basis.

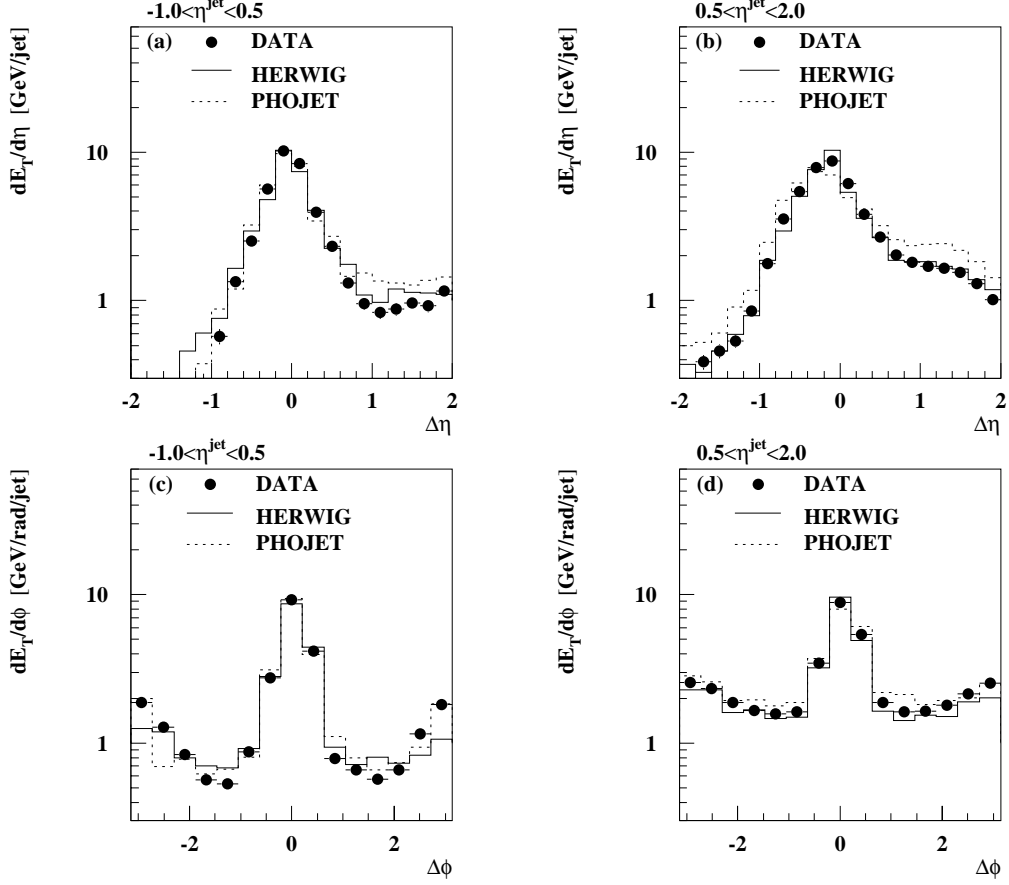


Figure 6.5: The observed transverse energy flow about the jet axis versus the pseudorapidity distance from the jet direction (integrated over $|\phi^{cell} - \phi^{jet}| \leq 1$) and the azimuthal angle with respect to the jet direction (integrated over $|\eta^{cell} - \eta^{jet}| \leq 1$). The jet profiles are shown for for two pseudorapidity bins: $-1.0 < \eta^{jet} < 0.5$ ((a),(c)) and $0.5 < \eta^{jet} < 2.0$ ((b),(d)). Full circles are H1 data. The curves refer to the predictions from the HERWIG event generator including the soft underlying event option for 35% of events (full) and the PHOJET generator (dashed) respectively.

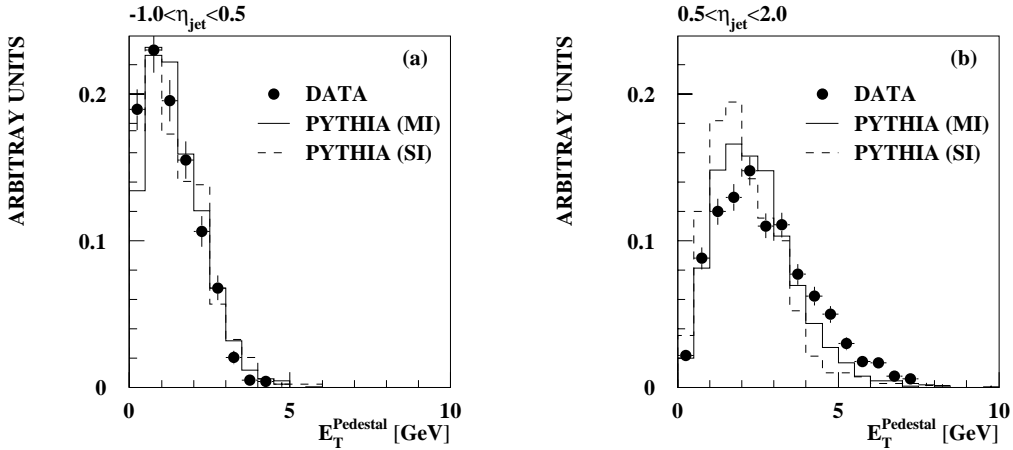


Figure 6.6: The distribution of the transverse energy measured outside the jets in the slice $|\eta^{cell} - \eta^{jet}| \leq 1.0$, $E_T^{Pedestal}$, normalised to the area of the jet cone for a) $-1.0 < \eta^{jet} < 0.5$ and b) $0.5 < \eta^{jet} < 2.0$. Full circles are H1 data. The curves refer to the predictions from the PYTHIA event generator with (full) and without (dashed) the inclusion of multiple interactions.

In order to study the fluctuations in the jet pedestal the distribution of the total transverse energy outside of the jet cone, within the region $|\eta^{jet} - \eta^{cell}| < 1.0$ is shown in figure 6.6. Regions in the η/ϕ plane affected by additional jets are excluded from the calculation. The total transverse energy has then been normalised to the area of the jet cone. Again the distributions are shown for two bins in pseudorapidity: $-1.0 < \eta^{jet} < 0.5$ and $0.5 < \eta^{jet} < 2.0$. The observed distributions are compared with predictions from the PYTHIA event generator both with and without the inclusion of the multiple interaction model implemented within the PYTHIA generator. This further illustrates the poor description of the jet pedestal effect provided by the standard PYTHIA event generator for jets reconstructed in the forward region. Again, an improved description of the jet pedestal distribution is provided by the inclusion of the multiple interaction model, however the PYTHIA Monte Carlo with the inclusion of multiple interaction model clearly underestimates the energy flow outside the jet cone.

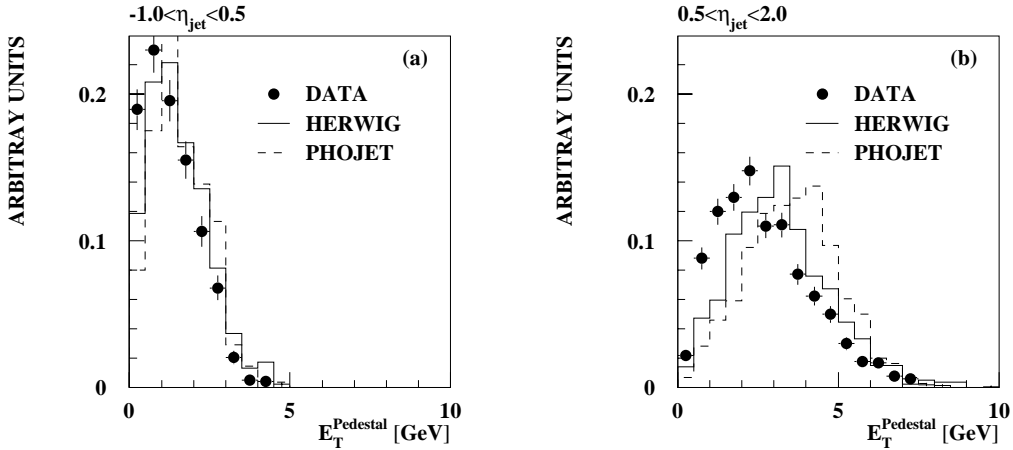


Figure 6.7: The distribution of the transverse energy measured outside the jets in the slice $|\eta^{cell} - \eta^{jet}| \leq 1.0$, $E_T^{Pedestal}$, normalised to the area of the jet cone for a) $-1.0 < \eta^{jet} < 0.5$ and b) $0.5 < \eta^{jet} < 2.0$. Full circles are H1 data. The curves refer to the predictions from the HERWIG event generator with the soft underlying event option for 35% of events (full) and the PHOJET generator (dashed) respectively.

The distribution of the total transverse energy of the jet pedestal is compared with the HERWIG and PHOJET generators in figure 6.7. Again for the HERWIG generator, the soft underlying event option is included for 35% of events. Clearly neither the HERWIG or PHOJET generators give a satisfactory description of the data for jets reconstructed in the forward region. However, all the models including multiple interactions give the expected increase in the jet pedestal in the forward region, as seen in the data.

6.4 Summary and Conclusions

The energy flow in photoproduction events with at least one jet with $E_T > 7$ GeV has been studied. The increased jet pedestal observed in the data compared with the predictions of leading order Monte Carlo generators for jets reconstructed in the forward region has been illustrated. Several Monte Carlo models including

the possibility of multiple interaction have been compared with the measured jet profiles. The inclusion of multiple interactions has been found to lead to an increased jet pedestal for jets reconstructed in the forward region, as observed in the data. This is in agreement with observations at $p\bar{p}$ [60, 61, 62] scattering in which Monte Carlo generators which include multiple interactions have been found to describe the data significantly better than generators including QCD radiation effects and hadronisation alone. A perfect description of the energy flow has not yet been achieved, and the presence of multiple interactions can not be inferred from the description of the jet pedestals alone.

A more detailed study of the energy flow in hard photoproduction has recently been presented by the H1 collaboration [42]. A description of the energy flow is imperative in order to enable reconstructed jet quantities to be unfolded to the partonic level, enabling the determination of the parton distribution within the photon. However, the study of multiple interactions is also of interest in its own right as very little is known theoretically about the features of multiple interactions. This is illustrated by the variation in predictions from different Monte Carlo models for this effect. Photoproduction offers a unique opportunity to study the effect of multiple interactions, as it is possible to compare the energy flow observed in resolved photoproduction, in which multiple interactions would be expected to contribute, with the energy flow in direct photoproduction, in which multiple interactions can not contribute. This has been the basis for recent studies by the photoproduction working group at H1, and with increased statistics in subsequent data taking periods will enable a more detailed understanding of the energy flow in photoproduction to be achieved.

Chapter 7

The Track Multiplicity in the Forward Region

7.1 Introduction

As shown in the previous chapter, studies of the energy flow measured in the LAr calorimeter for photoproduction events with at least one reconstructed jet, have shown a marked discrepancy between data and predictions from leading order Monte Carlo generators, such as the PYTHIA generator. This is most noticeable in the description of the energy flow for events with a reconstructed jet in the forward region, $\eta_{jet} > 0.5$, for which the data shows an increased jet pedestal effect compared with the predictions of leading order QCD calculations including QCD radiation effects and hadronisation alone. The increased energy flow is expected from generators which include the possibility of multiple interaction. However the present understanding of the multiple interaction mechanism is limited and present models have failed to give a complete description of the energy flow in such events.

In this chapter, an independent analysis is presented in which the charged particle multiplicity in the forward region for hard photoproduction events has been studied using the H1 forward tracking detector. The charged particle multiplicity in the region $2.0 < \eta < 2.5$ has been used to study the description of the data provided by standard leading order Monte Carlo generators and to test the need for the inclusion

of multiple interaction models.

7.2 Event Sample

In order to study the charged particle multiplicity in the forward region in hard photoproduction, the tagged event sample triggered by a coincidence between an electron in the small angle electron tagger and a track from the central jet chamber trigger has been used. Processes involving a hard scattering are characterised by a high value of p_T^{max} , defined by the particle with the highest p_T in the event. On the other hand, soft processes are not expected to have a high value of p_T^{max} , since here the particle p_T essentially comes from hadronisation. For events with $p_T^{max} \geq 1.5$ GeV/c, soft photoproduction can be neglected. In order to select events in which a hard scattering has occurred, a track based selection has then been performed. For this analysis, events have been selected using the variable $p_T^{max'}$, defined by the highest p_T good reconstructed track in the restricted η range $\eta < 0.5$. The event selection has been restricted in this way to avoid any bias introduced by the presence of multiple interactions. The corrected track multiplicity may then be directly compared with predictions from leading order Monte Carlo generators. Furthermore, the selected sample is independent of the measured energy flow in the LAr calorimeter. This is an important consideration as this avoids any bias introduced by a poor description of the LAr calorimeter, should this be the reason for the observed discrepancy in the energy flow in photoproduction.

7.3 Determination of the Corrected Track Multiplicity

In order to obtain a corrected track multiplicity in the region $2.0 < \eta < 2.5$, the data have firstly been corrected for the difference in the track reconstruction efficiency between data and Monte Carlo, as illustrated in section 5.4. The difference in the planar segment efficiency in each supermodule has been determined using the

Supermodule	Absolute difference in efficiency (%)
SM 0	9.1 ± 0.5
SM 1	4.9 ± 0.4
SM 2	6.5 ± 0.8

Table 7.1: The difference in the planar segment efficiency, determined from the weighted mean of the difference in the missing segment efficiency, between data and MC for each supermodule respectively

weighted mean of the difference in the missing segment efficiency between data and Monte Carlo as a function of the total number of tracks in the forward tracker, and is shown in table 7.1 for each supermodule respectively. In this approach it has been assumed that the difference in the missing segment efficiency, determined using the inherent redundancy in the forward tracker, is due to an absolute difference in the planar segment efficiency, and that the linking efficiency between individual planar segments is well described by the Monte Carlo simulation. This is justified by the description of the dependence of the missing segment efficiency provided by the Monte Carlo simulation.

The difference in the planar segment efficiency between data and Monte Carlo has been allowed for by weighting each track reconstructed in the data by a factor W^k which is calculated separately for each possible configuration of at least two planar segments. The index k refers to the configuration being considered and has values in the range $k = 1 \rightarrow 4$ corresponding to tracks with a planar segment in the first and second supermodule, the first and third supermodule, the second and third supermodule, and all three supermodules respectively. The factor W^k is given by

$$W^k = \frac{\epsilon_{MC}^k}{\epsilon_{data}^k} \quad (7.1)$$

where ϵ_{MC} and ϵ_{data} are the probability to reconstruct a track with the particular planar segment configuration under consideration for Monte Carlo and data respectively.

The factor ϵ_{MC}^k is obtained by summing up the contributions to the total probability for the k^{th} configuration of planar segments per track due to all possible configurations of individual planar segments before the segment linking procedure. Each contribution is calculated using the measured planar segment and linking efficiencies determined by the Monte Carlo simulation. The factor ϵ_{data}^k is calculated in a similar way allowing for the difference in the planar segment efficiency between data and MC.

Having reweighted the data, the overall track efficiency as determined from the Monte Carlo simulation is then applied. The efficiency contains two multiplicative components: (i) the efficiency to reconstruct a track with at least two planar segments and (ii) the efficiency of the track selection for primary reconstructed tracks. As shown in section 5.3 the track reconstruction and selection efficiency is strongly dependent on the track multiplicity in the forward tracker.

The data have been corrected for the track reconstruction and selection efficiency as a function of the transverse momentum of the track and the total track multiplicity. This has been achieved by applying an empirical polynomial fit to the measured efficiency as a function of the total track multiplicity in the forward tracker for the p_T range $0.3 < p_T < 0.5$ GeV/c. The difference in the efficiency as a function of p_T has then been accounted for by applying a constrained fit to the track reconstruction and selection efficiency as a function of the total track multiplicity in each bin considered.

The total track multiplicity referred to in the above is the total number of tracks reconstructed in the forward tracker before any track selection and over the full acceptance of the forward tracker, including reconstructed tracks with only one planar segment. The track reconstruction efficiency before any track selection for tracks with at least one planar segment is approximately 85%. The track reconstruction efficiency is ultimately dependent on the hit multiplicity in the forward tracker, however it has not been possible to correct the data as a function of the hit multiplicity directly and instead the reconstructed track multiplicity has been considered. The systematic error in the measured efficiency has then been determined by considering

the variation in the observed number of tracks given the average track reconstruction efficiency.

As described in section 5.5 the track selection cannot achieve a perfect separation of primary and secondary tracks. To allow for the contamination due to secondary tracks the data have been corrected using the results of a detailed Monte Carlo simulation. The correction has been applied by weighting each track by a factor given by the purity of the sample after the full track selection as a function of the transverse momentum of the track. The determination of the contamination due to secondary tracks is sensitive to the description in the detector simulation program of the material between the central and forward tracking detectors and surrounding the beam pipe. A conservative systematic error of 20% has been assigned to the contamination of the selected track sample due to secondary reconstructed tracks giving an average systematic error due to the uncertainty in the Monte Carlo simulation of approximately 2%.

Due to the discrepancy between the observed distributions of the extrapolated track variables DCA and $Z_0 - ZVTX$, conservative track selection criteria have been applied. The systematic error on the track selection efficiency has been determined by considering the variation in the track selection efficiency obtained by restricting the track selection criteria applied. Due to the conservative nature of the track selection criteria applied, restricting the track selection criteria applied by 10% results in a reduction of the track selection efficiency by approximately 3%. This has been assigned as the systematic error on the track selection efficiency.

7.4 Results

The corrected transverse momentum spectrum, $1/N_{evt} dN_{trk}/dp_T$, in the region $2.0 < \eta < 2.5$ is shown in figure 7.1 for the selected data sample of events with $p_T^{max'} > 1.5$ GeV/c. The distribution has been corrected for bin migrations using a correction factor, given by the ratio of the number of generated primary tracks to the number of reconstructed tracks in each bin, restricting consideration to tracks which have

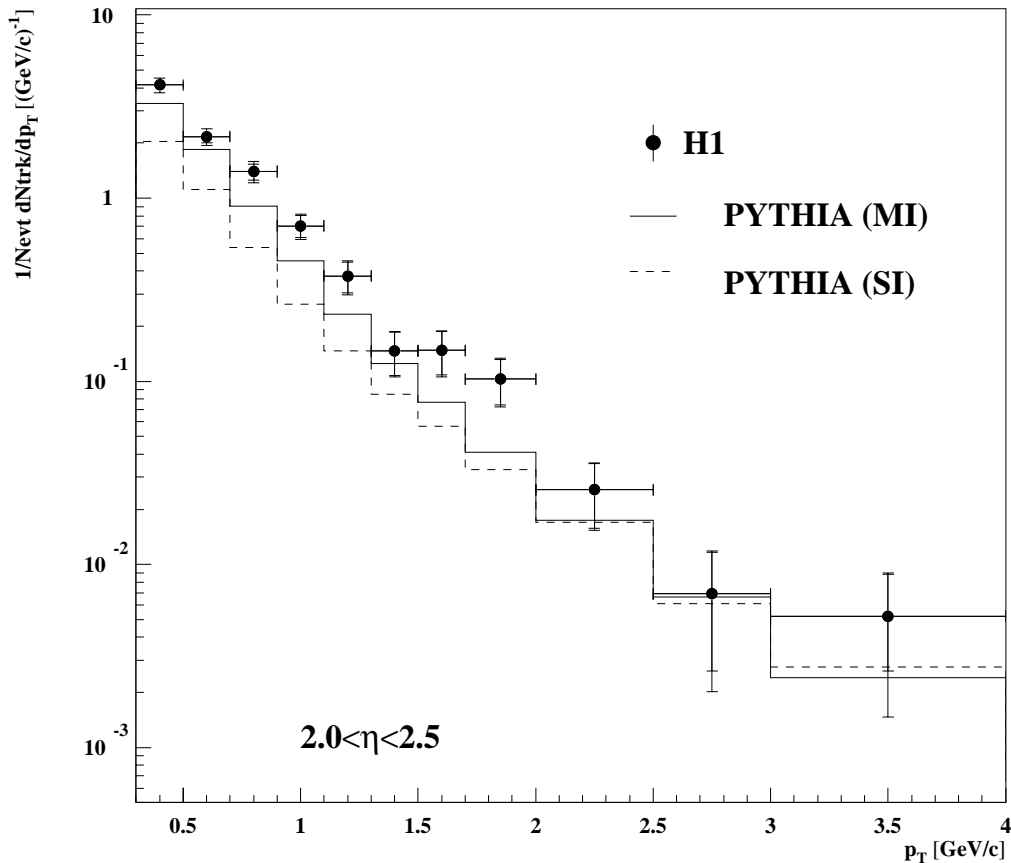


Figure 7.1: The corrected distribution $1/N \, dN_{trk}/dp_T$ for events with $p_T^{max'} > 1.5$ GeV compared with predictions from the PYTHIA generator both with (solid histogram) and without (dashed histogram) the inclusion of multiple interactions.

been matched to primary generated particles from the event vertex.

The corrected distribution is compared with predictions from the PYTHIA Monte Carlo both with and without the inclusion of multiple interactions. The data shows a significant excess of low p_T tracks compared with predictions from the PYTHIA Monte Carlo without the inclusion of multiple interactions. The inclusion of multiple interactions leads to an increased track multiplicity in the low p_T region, agreeing qualitatively with the data.

In figure 7.2, the observed transverse momentum distribution has also been compared with the PHOJET and HERWIG generators. As in the previous chapter, soft underlying event option for the HERWIG generator has been included for 35% of the

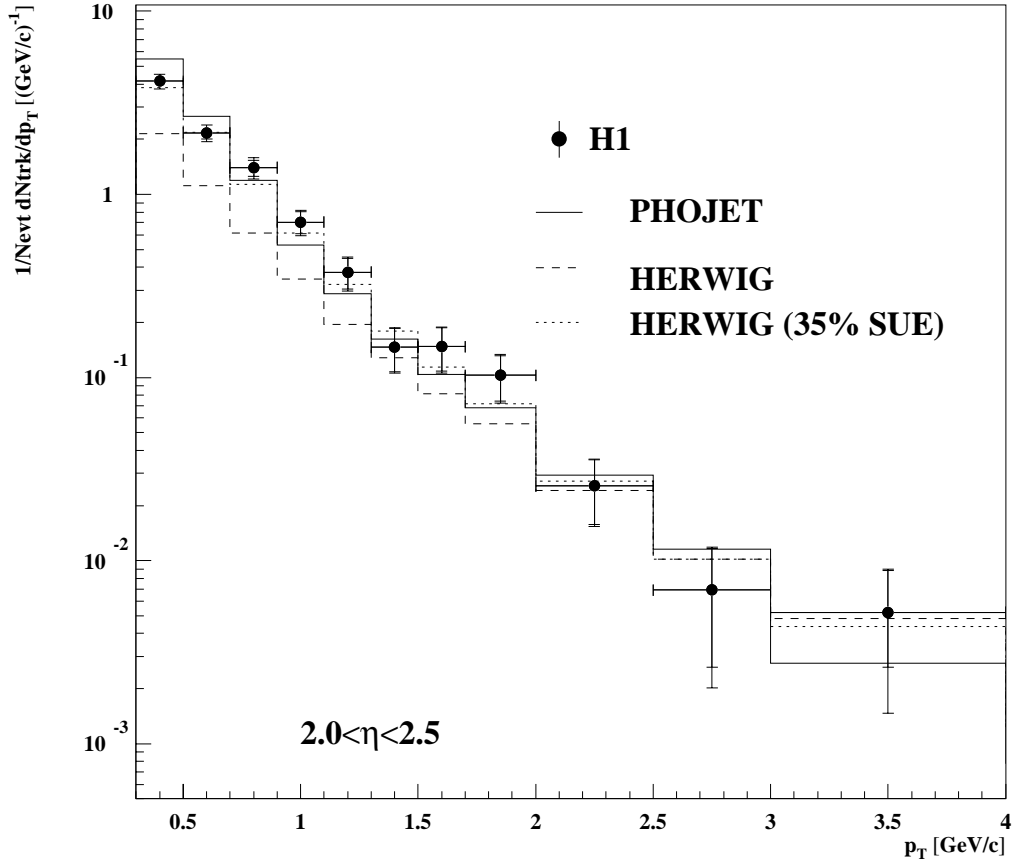


Figure 7.2: The corrected distribution $1/N \, dN_{trk}/dp_T$ for events with $p_T^{max'} > 1.5$ GeV compared with predictions from the PHOJET generator (solid histogram) and the HERWIG generator (dashed - without soft underlying event / dash dotted - 35% events including soft underlying event).

events. It can be seen that both the HERWIG and PHOJET Monte Carlos give an improved description of the transverse momentum spectrum, however it is not possible with the limited statistics and the systematic uncertainties in the corrections to determine more quantitative conclusions.

7.5 Summary and Conclusions

The corrected transverse momentum spectrum in the forward region for events with $p_T^{max'} > 1.5 \text{ GeV}/c$ has been studied and has provided an independent cross check of the discrepancy in the energy flow observed in the LAr calorimeter. Leading order QCD calculations fail to describe the multiplicity in this region, however the inclusion of multiple interaction models within several Monte Carlo generators give a qualitative description of the increased energy flow. This confirms the observed discrepancy observed in the energy flow as measured in the LAr calorimeter for hard photoproduction. In order to determine the presence of multiple interactions, further more detailed studies are required.

Chapter 8

The Inclusive Charged Particle Cross-section

8.1 Introduction

In this chapter the cross-sections $d^2\sigma/dp_T^2 d\eta$ and $d\sigma/d\eta$ for the inclusive production of charged particles in photoproduction are presented. The cross-sections are presented for the kinematical region $2.0 < \eta < 2.5$, $0.3 < y < 0.7$, $Q^2 < 10^{-2} \text{ GeV}^2$ and $p_T > 1.5 \text{ GeV}/c$. The measured cross sections are compared with previous results from $p\bar{p}$ interactions at $\sqrt{s} = 200 \text{ GeV}$ measured by the UA1 collaboration [72] and previous measurements by the H1 collaboration in the rapidity range $|\eta| < 1.5$. Leading order QCD predictions determined by the PYTHIA event generator both with and without the inclusion of multiple interactions are also compared with the measured cross sections.

8.2 Cross Section Determination and Results

The invariant cross section for single particle production is given by

$$\frac{d^2\sigma}{dp_T^2 d\eta_0} = \int \frac{d^3\sigma}{dp_T^2 d\eta_0 d\phi} d\phi = \pi E \frac{d^3\sigma}{dp^3} \quad (8.1)$$

assuming azimuthal symmetry of the cross section and thus allowing the integration over ϕ . Here $\eta_0 = -0.5 \ln((E - p_z)/(E + p_z))$ denotes the rapidity, which for $p \gg m$ can be approximated by the pseudorapidity $\eta = -\ln(\tan(\theta/2))$, with p and m being the particle momentum and mass respectively.

The inclusive charged particle cross section is calculated from the corrected number of tracks produced, $N_{produced}$, in each bin of p_T and η and is given by :

$$\frac{d^2\sigma}{dp_T^2 d\eta} = \frac{N_{produced}(p_T, \eta)}{L 2p_T \Delta p_T \Delta \eta} \quad (8.2)$$

where L denotes the integrated luminosity, and $\Delta p_T^2 = 2p_T \Delta p_T$ and $\Delta \eta$ are the bin widths.

In order to determine the inclusive charged particle cross-section, the minimum-bias tagged event sample has been used. The correction procedure outlined in the previous chapter has been used to determine the number of tracks produced in each bin. In addition the event selection and trigger efficiency has been corrected for on an event by event basis. The geometrical acceptance of the electron tagger has been corrected as a function of y , the fractional photon energy. The average acceptance in the range $0.3 < y < 0.7$ considered in this analysis is 54%. The tagger efficiency within this range is 100%. The ray trigger efficiency has been determined by a detailed Monte Carlo simulation tuned to the data. The trigger efficiency has been parameterised as a function of p_T^{max} , defined by the highest p_T good reconstructed track in the event. The trigger efficiency is 98% for events with $p_T^{max} > 1.5 \text{ GeV}/c$.

Two components in the event selection efficiency have to be considered. Firstly the restriction of the primary vertex to $-25 < ZVTX < 25 \text{ cm}$ has been taken into account by a constant $91 \pm 2\%$ efficiency factor, determined from the data. Secondly the topological event selection has been parameterised as a function of p_T^{max} . As reported in [73], for events with $p_T^{max} > 1.5 \text{ GeV}/c$ the effects of soft photo-production can be neglected and the event selection efficiency has been determined by the PYTHIA event generator with the inclusion of multiple interactions. Consideration will only be given here to the inclusive charged particle cross section for $p_T > 1.5 \text{ GeV}/c$. The efficiency for events with $p_T^{max} > 1.5 \text{ GeV}/c$ is 98%. For $p_T > 1.5 \text{ GeV}/c$ the average event selection efficiency is found to be $89 \pm 2 \pm 2\%$.

p_T [GeV/c]	$\frac{d^2\sigma^{ep}}{dp_T^2 d\eta} [\frac{nb}{(GeV/c)^2}]$	$\sigma_{stat} [\frac{nb}{(GeV/c)^2}]$	$\sigma_{syst} [\frac{nb}{(GeV/c)^2}]$
1.5-1.7	32.1	3.6	3.0
1.7-2.0	24.3	2.9	2.6
2.0-2.5	5.0	0.8	0.6
2.5-3.0	1.4	0.4	0.2
3.0-4.0	0.90	0.23	0.15
4.0-5.0	0.199	0.074	0.051
5.0-6.5	0.078	0.036	0.031
6.5-8.0	0.0177	0.0093	0.0135

Table 8.1: The measured differential cross section $\frac{d^2\sigma^{ep}}{dp_T^2 d\eta}$ for the production of charged particles in the η range 2.0 to 2.5.

The measured differential cross sections in the region $2.0 < \eta < 2.5$ are shown in figure 8.1. The inner error bars denote the statistical error and the outer error bars indicate the quadratically combined systematic and statistical errors. An overall systematic error of 5% from the determination of the luminosity is not included. The measured cross-sections are listed in table 8.2. The inclusive charged particle cross-section for $p\bar{p}$ interactions determined by the UA1 collaboration are also shown in figure 8.1. The $p\bar{p}$ cross-sections correspond to $\sqrt{s} = 200$ GeV in the rapidity interval $|\eta| < 2.0$. The UA1 data points are normalised to the H1 point at $p_T = 1.5$ GeV/c. The scale factor of order 4000 can be understood in terms of the photon flux factor, the (ρ, ω, ϕ) -meson coupling constants within the VDM model (of order 200), a factor π (see equation 8.1), a factor 1.5 (3 instead of 2 quarks in mesons versus baryons) and a factor 0.5 (UA1 measurements are for single charges only). The γp CMS system for the H1 data is typically boosted by two units of rapidity in the forward direction with $\sqrt{s} \approx 200$ GeV. The spread in this shift due to the photon energy range is less than 0.3 units in pseudorapidity. The H1 data overlaps with the rapidity interval measured by the UA1 collaboration in the proton hemisphere.

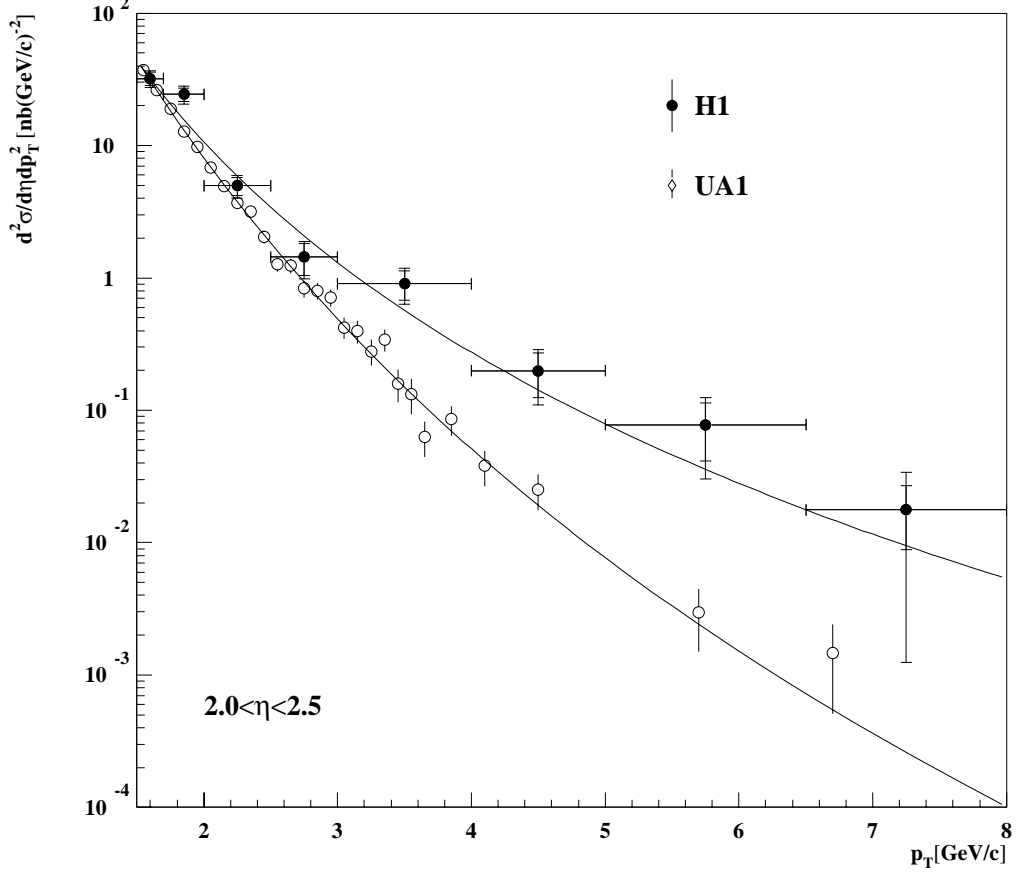


Figure 8.1: The measured inclusive charged particle cross-section $\frac{d^2\sigma^{ep}}{dp_T^2 d\eta}$ in photo-production (full circles) in the kinematical region $2.0 < \eta < 2.5$, $Q^2 < 10^{-2}\text{GeV}^2$ and $0.3 < y < 0.7$ at an average $E_{CMS}(\gamma p) \approx 200 \text{ GeV}$. The error bars indicate the quadratic sum of statistical and systematic errors. An overall uncertainty of 5 % from the luminosity measurement is not included. The cross sections measured by the UA1 collaboration for $p\bar{p}$ interactions for $\sqrt{s} = 200 \text{ GeV}$ and $|\eta| < 2$ are also shown, normalised to the H1 data at $p_T = 1.5\text{GeV}/c$. The curves show the result of a QCD inspired power law fit to the data.

Experiment	η range	$(p_T)_0[GeV/c]$	n
H1 1992	-1.5 - 1.5	0.63 ± 0.20	7.1 ± 2.0
H1 1993	2.0 - 2.5	0.44 ± 0.13	6.2 ± 0.6
UA1	-2.5 - 2.5	1.8 ± 0.1	12.14 ± 0.39

Table 8.2: The results of a QCD inspired power law fit to the inclusive charged particle spectra measured by H1 and UA1 respectively in the region $p_T > 1.5$ GeV/c.

A QCD inspired power law fit [74] to the data given by:

$$E \frac{d^3\sigma}{dp^3} = A \left(1 + \frac{p_T}{(p_T)_0}\right)^{-n} \quad (8.3)$$

has been applied to both the UA1 and H1 measurements. The measured cross-sections are well described by equation 8.3. The results of the fit are summarised in table 8.2. Also shown is the result of a fit to the previously published result using data collected by H1 in 1992 for the kinematic region $|\eta| < 1.5$. The curves in figure 8.1 indicate the results of the above power law fit. From the results of the fit it can be clearly seen that the γp data show a significantly more pronounced tail at large transverse momenta. This agrees qualitatively with results obtained by the WA69 collaboration [75] at $\sqrt{s}=18$ GeV. The WA69 collaboration determined the inclusive charged particle cross section with real photon and hadron ($=60\%\pi+40\%K$) beams within the same experimental setup, observing a more pronounced tail in the distribution at large transverse momenta for the former case.

In figure 8.2 the cross sections are compared with the previously measured cross section for photoproduction interactions in the rapidity range $|\eta| < 1.5$, determined using data collected in 1992 by the H1 collaboration. It can be seen that the measured cross sections in the forward region, are compatible within the errors with the previous H1 measurement, though the cross sections favour a slightly harder spectrum than previously observed.

The more pronounced tail in the observed p_T spectra compared with $p\bar{p}$ scattering illustrates the differences between the two interactions at high p_T . This is

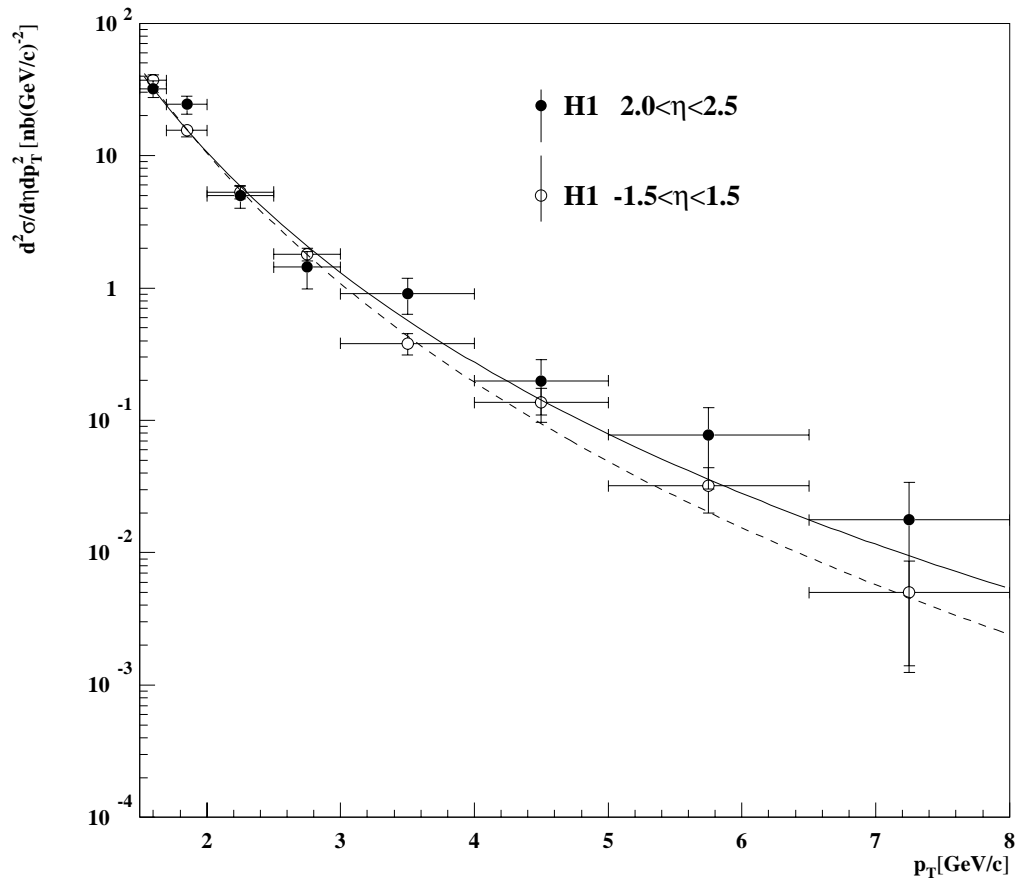


Figure 8.2: The measured inclusive charged particle cross-section as depicted in figure 8.3 (full circles) compared with the previously measured cross section for the rapidity range $|\eta| < 1.5$ (open circles).

in contrast to the similarity observed in the low p_T region previously observed and as expected from the VDM model. There are several possible reasons for this disagreement. Firstly the measurements cover differing ranges of rapidity. The results presented correspond to a pseudorapidity in the CMS system of $0 < \eta^* < 0.5$.

Secondly, within the framework of the VDM model, γp collisions can be approximated as an interaction of a vector mesons with a proton. The p_T spectrum for Vp collisions may be harder than $p\bar{p}$ interactions at similar energies, since the parton momenta of quarks in mesons are on average larger than in baryons. Finally, photo-production interactions also receive a contribution from the anomalous component of the resolved photon, and the direct photon, both of which contribute at high p_T .

The measured cross sections are compared with a leading order QCD prediction, determined by the PYTHIA event generator, in figure 8.3. The full line represents the full calculation including all processes. Also shown is the contribution of the resolved processes only (dashed line). The GRV-LO parton distribution functions have been used for the proton and photon. The leading order QCD prediction does not describe the observed slope of the p_T spectrum. It can also be seen that the direct contribution only contributes a small fraction of the cross section, and is not able to describe the difference in the cross section between the data and the resolved component of the cross section. The predictions are however dependent on the parton distribution functions used to describe both the photon and proton. In particular, the gluon distribution function in the photon is not well constrained, though recent measurements by the H1 collaboration favour the GRV parameterisation, in which the gluon distribution is essentially generated radiatively, compared with more extreme predictions such as the LACI and LACIII parton distribution functions. However with the large statistical and systematic errors in the present measurement, it is not possible to draw further quantitative conclusions concerning parton distribution functions.

The inclusive charged particle cross-section $d\sigma/d\eta$ for particles with $p_T > 1.5$ GeV/c and $2.0 < \eta < 2.5$ is shown in figure 8.4 compared with the previously published cross sections measured using H1 data taken during 1992 in the range

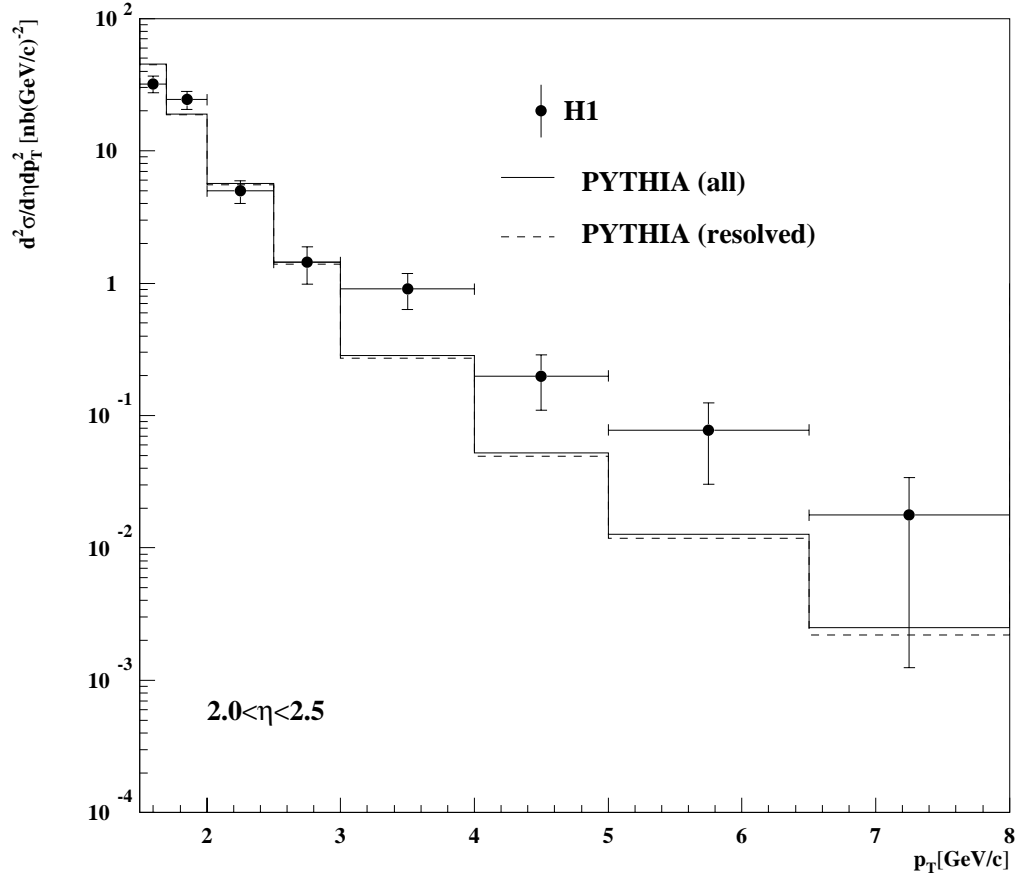


Figure 8.3: The measured inclusive charged particle cross-section $\frac{d^2\sigma^{ep}}{dp_T^2 d\eta}$ in photo-production (full circles) compared with the predictions from a LO QCD calculation using the PYTHIA generator. The dashed line represents the contribution of the resolved component only and the solid line represents the sum of the resolved and direct contributions.

$|\eta| < 1.5$. Also shown are the predictions of a LO calculation using the PYTHIA generator with the inclusion of multiple interactions. The contributions to the cross section of the resolved and direct components is illustrated. The measured cross sections are compatible within the statistical and systematic errors with the predictions of the PYTHIA generator. The effect of the inclusion of multiple interactions is illustrated in figure 8.5 in which the measured cross sections are compared with predictions of the PYTHIA Monte Carlo with and without the inclusion of multiple interactions. In both cases the direct component is included. The inclusion of multiple interactions gives an increased cross section in the forward region, giving an improved description of the measured cross section in this region. The HERWIG and PHOJET generators give similar results to the PYTHIA Monte Carlo shown above.

8.3 Summary

A first measurement of the inclusive charged particle cross sections $d^2\sigma/dp_T^2 d\eta$ and $d\sigma/d\eta$ for the kinematical region $2.0 < \eta < 2.5$, $0.3 < y < 0.7$ and $Q^2 < 10^{-2} GeV^2$ and $p_T > 1.5 GeV/c$ has been presented. The results have been compared with previous measurements by the UA1 collaboration for $p\bar{p}$ interactions at a centre of mass energy ranging of $\sqrt{s} = 200 GeV$ for the pseudorapidity range $|\eta| < 2.0$. At H1 the γp centre of mass is on average shifted by two units of rapidity in the forward direction, and the measured cross sections overlap with the UA1 measurement in the proton hemisphere. The observed p_T spectra has been found to be well described by a QCD inspired power law fit and is significantly harder than the measured spectra for $p\bar{p}$ interactions at the same centre of mass energy. The measured cross sections have also been compared with LO Monte Carlo predictions using the GRV parameterisations for the photon and proton structure functions. The data has been found to favour a harder spectrum than predicted by the leading order calculation.

The overall cross section $d\sigma/d\eta$ for particles with $p_T > 1.5 GeV/c$ has also been

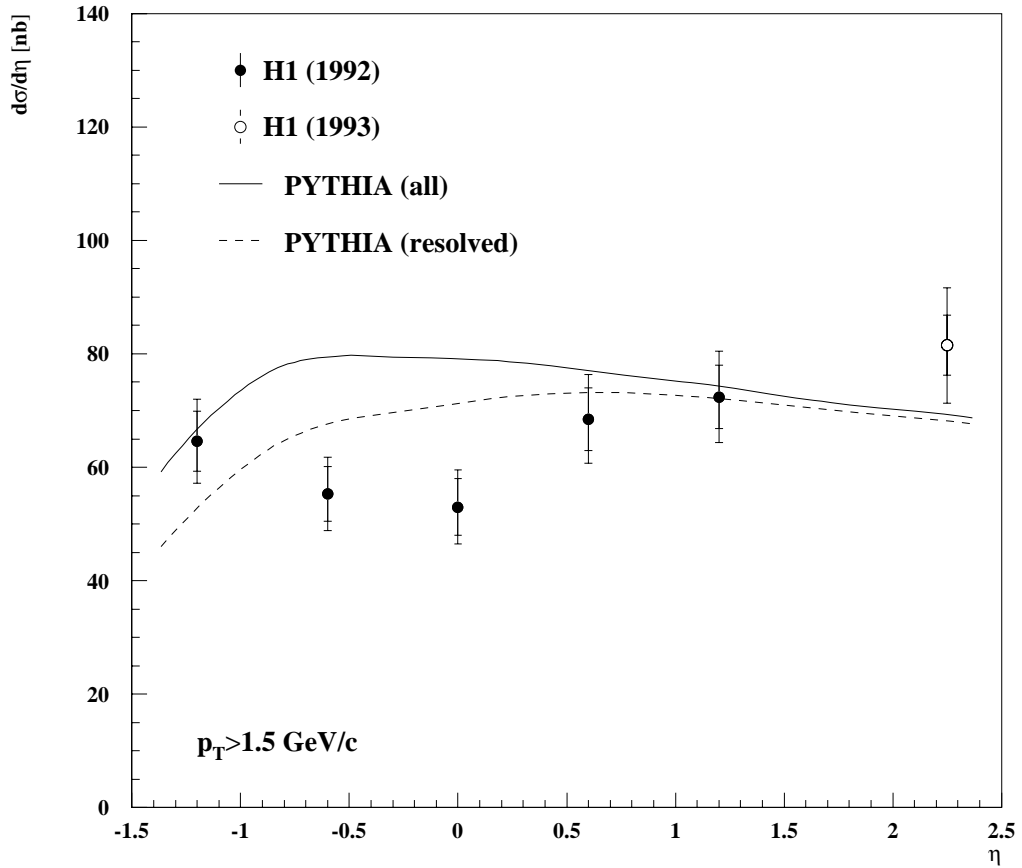


Figure 8.4: The measured inclusive charged particle cross-section $d\sigma/d\eta$ in photo-production in the kinematical region $p_T > 1.5$ GeV/c and $2.0 < \eta < 2.5$ (open circles) compared with the previously measured cross-sections in the η region $|\eta| < 1.5$ and predictions from a LO QCD calculation using the PYTHIA generator. The dashed line represents the contribution of the resolved component only and the solid line represents the sum of the resolved and direct contributions.

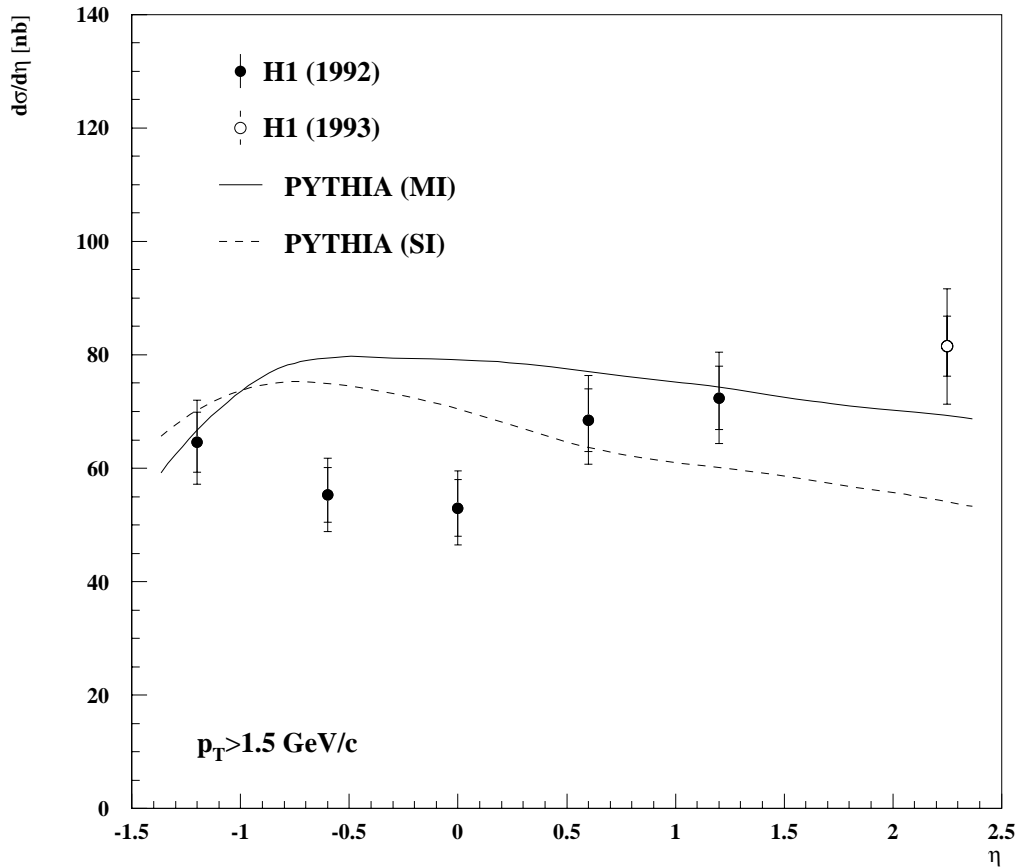


Figure 8.5: The measured inclusive charged particle cross-section $d\sigma/d\eta$ in photo-production in the kinematical region $p_T > 1.5$ GeV/c and $2.0 < \eta < 2.5$ (open circles) compared with predictions from a LO QCD calculation using the PYTHIA generator both with (full) and without (dashed) the inclusion of multiple interactions.

measured in this region and has been found to be

$$d\sigma/d\eta = 73.2 \pm 4.8(stat) \pm 7.8(sys) nb$$

This is compatible with the results of a leading order Monte Carlo prediction provided multiple interaction models are included.

Chapter 9

Summary

In this thesis, an analysis of hard photoproduction at HERA has been presented. The poor description of the energy flow in the forward region provided by LO QCD calculations including QCD radiation and hadronisation effects has been illustrated. This is particularly noticeable in the description of the jet profiles and jet pedestal distribution for jets reconstructed in the forward region. The possibility that the increased energy flow in the forward region is due to the presence of multiple scattering has been examined. The description of the data has been improved by including multiple interaction models within the framework of several Monte Carlo generators. This agrees with observations in $p\bar{p}$ scattering, in which an improved description has been observed with the inclusion of multiple interactions.

To further test the presence of multiple interactions and to provide an independent cross check, the track multiplicity in the forward region has been studied. In order to facilitate this, a detailed study of the performance of the H1 Forward Tracker has been presented. The corrected track multiplicity has then been measured for hard photoproduction events selected by a track based selection. The results have been compared with predictions of several different event generators, and have further illustrated the improved description of the data provided by the inclusion of multiple interaction models.

Finally, the inclusive charged particle cross section in photoproduction has been presented for the kinematical range $2.0 < \eta < 2.5$, $0.3 < y < 0.7$, $Q^2 < 10^{-2} \text{ GeV}^2$

and $p_T > 1.5 \text{ GeV}/c$. A QCD inspired power law fit to the transverse momentum distribution has been applied and the results compared with previously measured cross sections both in photoproduction and $p\bar{p}$ scattering. The transverse momentum distribution has been found to be noticeable harder than in $p\bar{p}$ scattering at equivalent centre of mass energies. The measured cross sections have also been compared with the predictions of a leading order QCD event generator, with the data favouring a harder spectrum than predicted.

The overall cross section $d\sigma/d\eta$ for particles with $p_T > 1.5 \text{ GeV}/c$ has also been measured in this region and has been found to be

$$d\sigma/d\eta = 73.2 \pm 4.8(stat) \pm 7.8(sys) \text{ nb}$$

This is compatible with the results of a leading order Monte Carlo prediction provided multiple interaction models are included.

Bibliography

- [1] F.Abe et al., Phys.Rev.Lett. **74** (1995) 2626.
- [2] S.Abachi et al., Phys.Rev.Lett. **74** (1995) 2632.
- [3] R.Hofstadter, Rev. Mod. Phys. **28** (1956) 214.
- [4] Joel Feltesse, *Low x Physics, Deep Inelastic Scattering and Structure Functions*,
Review Paper presented at XXVII International Conference on High Energy
Physics: Session Pl-4, Glasgow,UK,20-27 July 1994
- [5] F.Halzen and A.Martin, *Quarks and Leptons: An Introductory Course in Mod-
ern Particle Physics*, John Wiley & Sons Inc. (1984).
- [6] J.D.Bjorken, Phys. Rev. **163** (1967) 1767.
- [7] M.Breidenbach et al., Phys. Rev. Lett. **23** (1969) 935.
- [8] G.Altaralli,G.Parisi, Nucl. Phys. **126** (1977) 298.
- [9] C.F.Weizacker, Z. Phys. **88** (1934) 612;
E.J.Williams, Phys. Rev. **45** (1934) 729.
- [10] A.I.Lebedev, Proceeding of the HERA Workshop (1992) Vol 1,613.
- [11] J.R.Smith, H1 note H1-12/92-259 (1992)
- [12] I.Abt, J.R.Smith, H1 note H1-10/92-249 (1992)
- [13] J.J.Sakurai, Ann. Phys. **11** (1960) 1;
M.Gell-Mann and F.Zachariasen, Phys. Rev. **124** (1961) 953.

- [14] G.Wolf and P.Soding, in ‘Electromagnetic Interactions of Hadrons’;
Vol.2,p.1; Eds. Donnachie and Shaw, 1978.
- [15] M.Greco, Nucl. Phys. **63B** (1973) 398.
- [16] Ch.Berger and W.Wagner, Phys.Rep. **146** (1987) 1;
H.Kolanoski and P.Zerwas, ‘Two-Photon Physics’ in ‘High Energy Electron-
Positron Physics’, eds. A.Ali and P.Soding, World Scientific 1988.
- [17] G.A.Schuler and T.Sjostrand, Nucl. Phys. **B407** (1993) 539.
- [18] M.Drees and R.Godbole, **MADPH-95-898** (1995)
- [19] H.Abramowicz et al., Int. J. Mod. Phys. **A8**, (1993) 1005.
- [20] E.Witten, Nucl. Phys. **B120** (1977) 189;
R.J.deWitt et al., Phys. Rev. **D19** (1979) 2046.
- [21] For a recent review of data on the production of hadronic final states in
(real or virtual) two-photon collisions see : D.Morgan, M.R.Pennington and
M.R.Whalley, J. Phys. **G20** (1994) A1.
- [22] OPAL collab., R.Akers et al., Z.Phys. **C61** (1994) 199.
- [23] TOPAZ collab., K.Muramatsu et al., Phys. Lett. **B332** (1994) 477.
- [24] H.Abramowicz, K.Charchula and A.Levy, Phys. Lett. **B269** (1991) 458.
- [25] M.Gluck, E.Reya and A.Vogt, Z.Phys. **53C** (1992) 127.
- [26] H1 Collab., T.Ahmed et al., Phys. Lett. **B299** (1993) 374.
- [27] ZEUS Collab., M.Derrick et al., Phys. Lett, **B293** (1992) 465.
- [28] H1 Collab., S.Aid et al., DESY-95-162 to be published in Zeitschrift f. Physik.
- [29] T.Regge, Nuov. Cim. **14** (1959) 951, Nuov. Cim. **18** (1960) 947;
G.Chew, S.Frautschi, S.Mandelstam, Phys. Rev **126** (1962) 1202.

- [30] A.Donnachie and P.V.Landshoff, CERN-TH.6488/92(1992).
- [31] A.Levy, J. Phys. **G19** (1993) 1489.
- [32] J.K.Storow, J. Phys. **G19** (1993) 1641.
- [33] S.Lomatch, F.I. Olness and J.C.Collins, Nucl. Phys. **B317** (1989) 617.
- [34] M.Froissart, Phys. Rev. **123** (1961) 1053.
- [35] TOPAZ collab., H. Hayashii et al., Phys. Lett. **B314** (1993) 149;
AMY collab., B.J. Kim et al., Phys. Lett. **B325** (1994) 248.
- [36] AMY collab., R.Tanaka et al., Phys. Lett. **B277** (1992) 215;
ALEPH collab., D.Buskulic et al., Phys. Lett. **B313** (1993) 509;
DELPHI collab., P.Abreu et al., CERN report PPE-94-04.
- [37] J.R.Forshaw and J.K.Storow, Phys. Lett. **B321** (1994) 151.
- [38] M.Drees, Talk presented at the meeting on *Two-Photon Physics at LEP and HERA*, Lund, Sweden, May 1994 (see preprint MAD/PH/841).
- [39] H1 collab., T.Ahmed et al., Phys. Lett. **B297** (1992) 205.
- [40] H1 collab., T.Ahmed et al., Phys. Lett. **B314** (1993) 436.
- [41] H1 collab., T.Ahmed et al., Nucl. Phys. **B445** (1995) 195.
- [42] H1 collab., A. Buniation, Talk given at the International workshop PHOTON-95, Sheffield, UK, 8-13 April 1995.
- [43] ZEUS collab., M.Derrick et al., Phys. Lett. **B297** (1992) 404.
- [44] ZEUS collab., M.Derrick et al., Phys. Lett. **B322** (1994) 287.
- [45] ZEUS collab., M.Derrick et al., Phys. Lett. **B342** (1995) 417.
- [46] ZEUS collab., M.Derrick et al., Phys. Lett. **B348** (1995) 665.

- [47] H1 collab., I.Abt et al., ‘The H1 detector at HERA’, DESY 93-103 (1993), to be submitted to Nucl. Instr. and Meth.
- [48] J.Burger et al., Nucl Instr. and Meth. **A279** (1989) 217.
- [49] K.Muller et al., Nucl Instr. and Meth. **A312** (1992) 457.
- [50] S.Burke et al., RAL-95-037/DESY-95-132, March 1995.
- [51] B. Andrieu et al., Nucl. Instr. and Meth. **A336** (1993) 460.
- [52] B. Andrieu et al., Nucl. Instr. and Meth. **A350** (1994) 57.
- [53] B. Andrieu et al., Nucl. Instr. and Meth. **A336** (1993) 499.
- [54] G.Bernardi et al.,H1 collab., H1REC manual, internal H1 report.
- [55] M.Erdmann et al., H1 collab., H1PHAN manual, internal H1 report.
- [56] S.Egli et al.,H1 collab., H1SIM manual, internal H1 report.
- [57] H1 collab., I.Abt et al., Phys. Lett. **B328** (1994) 176.
- [58] S.Levonian, internal H1 communication.
- [59] T.Sjostrand, **CERN-TH-6488** (1992), Comp. Phys. Commun. **82** (1994) 74.
- [60] UA2 Collaboration, J.Alitti et al., Phys. Lett. **B268** (1991) 145.
- [61] AFS Collaboration, T.Akesson et al., Z. Phys. **C34** (1987) 163.
- [62] CDF Collaboration, L.J.Keeble et al., **FERMILAB-CONF-92-161-E (1992)**.
- [63] T.Sjostrand and M.Bengtson, Comp. Phys. Commun. **43** (1987) 367.
- [64] V.Blobel, **DESY 84-118**, and ‘Proceedings of the 1984 CERN School of Computing, Aiguablava (Spain), CERN 1985.

- [65] G.Marchesini and B.R.Webber, Nucl. Phys. **B310** (1988) 461;
G.Marchesini and B.R.Webber, Nucl. Phys. **B238** (1984) 1.
- [66] R.Engel, ‘Proceedings of the XXIXth Rencontre de Moriond (1994)’, p.321;
- [67] A.Capella et al., Phys. Rep. **236** (1994) 227.
- [68] P.Aurenche et al., Phys. Rev. **D45** (1992) 92;
F.W. Bopp et al., Comp. Phys. Commun. **83** (1994) 107.
- [69] A. Capella et al., Phys. Rev. Lett. **58** (1987) 2015.
- [70] R. Engel, Z. Phys. **C66** (1995) 203.
- [71] M.Devel, internal H1 report H1-SW-029;
M.Erdmann et al., H1 collab., H1PHAN manual, internal H1 report.
- [72] UA1 collab., C.Albajar et al., Nucl. Phys. **B335** (1990) 261.
- [73] H1 collab., I.Abt et al., Phys. Lett. **B328** (1994) 176.
- [74] R.Hagedorn, Riv. Nuovo Cim. **6** (1983) 1.
- [75] OMEGA Photon collab., R.J.Apsimon et al., Z. Phys. **C43** (1989) 63.